

# Novel Finger-like Soft Pneumatic Actuators for Affective Movement

by

Mohammadreza Memarian

A thesis  
presented to the University of Waterloo  
in fulfillment of the  
thesis requirement for the degree of  
Master of Applied Science  
in  
Electrical & Computer Engineering

Waterloo, Ontario, Canada, 2015

© Mohammadreza Memarian 2015

I hereby declare that I am the sole author of this thesis. This is a true copy of the thesis, including any required final revisions, as accepted by my examiners.

I understand that my thesis may be made electronically available to the public.

## Abstract

The ability to communicate emotion through movement is an important element to enable engaging social human-robot interaction. It has been shown that humans are capable of conveying emotion through hand and arm movements alone. Thus, simple robotics structures might be capable of emotion conveyance. In this thesis, the design and implementation of a finger-like robotic structure capable of performing movements that convey emotion is investigated. First, the requirements for such a mechanism are derived directly from human affective movement dynamics, coupled with application-specific constraints. Comparative analysis is performed on various actuation options based on these requirements. Studies suggest that fast dynamic motion is required for the conveyance of many emotions. Therefore, the analysis focused on determining actuation options that can produce controllable finger-like motion with fast dynamics. A class of pneumatic actuators called soft pneumatic artificial muscles (SPAMs) were determined to fit the requirements for finger-like affective motion better than the other available actuator options.

SPAMs are a type of pneumatic actuator that provides customizable motion trajectories in three dimensional space without the need for rigid links or a transmission mechanism. The motion of these actuators can be designed to be similar to the motion of the human finger. Their motion also achieves high velocities and accelerations. In addition, SPAMs provide high power to weight ratios and are compliant, making them suitable for interaction with human users.

In this thesis, a novel design for producing SPAMs, named wrapped SPAMs (WSPAMs) is introduced. Unlike previous SPAM designs, the production process of WSPAM is highly repeatable, while the motion trajectory can be easily tailored at the design stage. A model is presented for predicting the steady state angular displacement of the WSPAM actuator based on its geometrical parameters and the elasticity of the materials used in its production. The model is validated by experimental analysis. Two sets of experiments are designed and presented. The first set enables the estimation of the model parameters. In the second set of experiments, the estimated parameters are used to model WSPAMs through the possible range of design parameters. Six WSPAMs with design parameters within the physical limitations are constructed. Comparison of their performance against the modeled results is presented, and shows that the model is capable of estimating the performance of WSPAM within the physical limitations of its design.

Finally, a pneumatic circuit and a closed-loop controller for the finger-like movement of these soft pneumatic actuators is developed. An innovative approach, which uses a gyroscopic sensor, is used to add feedback on the position of these actuators and make

closed-loop control possible. Additionally, a simple and low-cost solution is designed to significantly improve the noisy behavior of the existing pneumatic driving mechanisms. The proposed controller design is validated on physical SPAM prototypes. Experimental results demonstrate the performance of the pneumatic and control system for the actuator, and its ability to track human movement trajectories with affective content.

## **Acknowledgements**

I would like to thank my supervisors, Professor Dana Kulić and Professor Rob Gorbet, for the patient guidance, encouragement and advice they provided throughout my time as their student. I have been extremely lucky to have supervisors who cared so much about my work, and who responded to my questions and queries so promptly. I would like to also thank Ali Samadani and Matt Borland for their help on various chapters of this work.

Lastly, I would like to thank the Robotics and Biology Laboratory from Technische Universität Berlin for providing us with their novel PneuFlex pneumatic actuators.

## **Dedication**

This is dedicated to my family and the love of my life.

# Table of Contents

List of Tables	ix
List of Figures	x
<b>1 Introduction</b>	<b>1</b>
<b>2 IFLS Design Requirements</b>	<b>5</b>
2.1 Analysis of Human Hand Affective Motion Trajectories . . . . .	5
2.2 Design Requirements . . . . .	13
2.2.1 Application-Specific Requirements (Interactive Architecture) . . . . .	14
2.2.2 Human Interaction Requirements . . . . .	14
2.2.3 Dynamic Requirements . . . . .	15
2.3 Summary of Design Requirements . . . . .	19
<b>3 Mechanical System Design</b>	<b>21</b>
3.1 Conventional Mechanical Designs . . . . .	21
3.1.1 Actuators . . . . .	23
3.1.2 Transmission . . . . .	33
3.2 Soft Pneumatic Artificial Muscles . . . . .	35
3.2.1 Background . . . . .	35
3.2.2 SPAM Requirement Analysis . . . . .	37
3.3 Mechanical System Design Summary . . . . .	47

<b>4</b>	<b>SPAM Control</b>	<b>49</b>
4.1	Proposed Approach . . . . .	50
4.1.1	PneuFlex Actuator design modification . . . . .	50
4.1.2	Electromechanical Driving Mechanism . . . . .	51
4.1.3	Controller . . . . .	56
4.2	Experiments . . . . .	57
4.2.1	Reference Signal . . . . .	57
4.2.2	Control System Requirements . . . . .	58
4.2.3	Controller Results . . . . .	58
<b>5</b>	<b>WSPAM</b>	<b>69</b>
5.1	WSPAM Production Process . . . . .	70
5.2	Steady state modelling . . . . .	76
5.3	Modelling the Effective Young's Modulus . . . . .	81
5.4	Experimental Validation . . . . .	86
<b>6</b>	<b>Conclusions</b>	<b>92</b>
	<b>Bibliography</b>	<b>101</b>

# List of Tables

2.1	Maximum and minimum end effector angular velocity in $rad/s$ for joy, anger, and sadness . . . . .	18
2.2	Maximum and minimum end effector angular acceleration in $rad/s^2$ for joy, anger, and sadness . . . . .	18
2.3	Required and desired velocity and acceleration of the flexion and extension motion of the IFLS . . . . .	19
2.4	Summary of Design Requirements . . . . .	20
3.1	End effector orientation, velocity, and acceleration of PneuFlex SPAM design	47
3.2	Comparison of the three most suitable actuation options against the requirements for the IFLS mechanism . . . . .	48
4.1	Measured end effector orientation, velocity, and acceleration error, for joy, anger, and sadness trajectories . . . . .	62
4.2	Maximum and minimum end effector orientation, velocity, and acceleration, for joy, anger, and sadness trajectories . . . . .	67

# List of Figures

1.1	Hylozoic Soil installation; the tentacle mechanism is marked by the red oval. This picture is used with permission from PBAI . . . . .	2
2.1	Frames of the animation of the human hand performing affective motion . . . . .	6
2.2	Kinematic structure of the hand recorded by the data glove showing the orientation and the location of the joints . . . . .	7
2.3	The local joint angle and the global end effector orientation of the five fingers during the trajectory for anger . . . . .	10
2.4	The local joint angle and the global end effector orientation of the five fingers during the trajectory for joy . . . . .	11
2.5	The local joint angle and the global end effector orientation of the five fingers during the trajectory for sadness . . . . .	12
2.6	End effector angular velocity of each finger for joy, anger, and sadness . . . . .	16
2.7	End effector angular acceleration of each finger for joy, anger, and sadness . . . . .	17
3.1	Sample robotic manipulator design for the IFLS . . . . .	22
3.2	Illustration of the three main pneumatic actuators in robotics . . . . .	28
3.3	PAM dynamic response test apparatus. PAM pressurized to 450kPa shown on left and atmospheric pressure PAM shown on right. . . . .	30
3.4	End effector orientation of PAM-actuated 1 DOF apparatus . . . . .	31
3.5	End effector angular velocity of PAM-actuated 1 DOF apparatus . . . . .	32
3.6	End effector angular acceleration of PAM-actuated 1 DOF apparatus . . . . .	32
3.7	Various transmission mechanisms . . . . .	34

3.8	Examples of current SPAM designs . . . . .	35
3.9	Pneumatic open-loop circuit . . . . .	38
3.10	Absolute end effector orientation of the PneuFlex measured on still images	39
3.11	Frequency content of the velocity of SPAM's full flexion and extension step response . . . . .	41
3.12	SPAM's full flexion and extension tip orientation response . . . . .	46
4.1	Components of the modified SPAM-based on the PneuFlex actuator . . . . .	51
4.2	The motion frames of the custom built SPAM with curved motion trajectory	51
4.3	The pneumatic circuit for the control of the SPAM actuator . . . . .	54
4.4	Pneumatic low pass filter . . . . .	54
4.5	Electrical circuit analogy of the pneumatic circuit with low pass filter and voltage divider . . . . .	56
4.6	Pressure-orientation closed-loop controller system for SPAM actuators . . .	57
4.7	Reference and experimental end effector orientation for the joy motion and orientation tracking error . . . . .	60
4.8	Reference and experimental end effector orientation for the anger motion and orientation tracking error . . . . .	61
4.9	Reference and experimental end effector orientation for the sadness motion and orientation tracking error . . . . .	62
4.10	Reference and experimental end effector angular velocity for the joy motion and angular velocity tracking error . . . . .	64
4.11	Reference and experimental end effector angular velocity for the anger motion and angular velocity tracking error . . . . .	65
4.12	Reference and experimental end effector angular velocity for the sadness motion and angular velocity tracking error . . . . .	66
4.13	Reference vs experimental motion response of the sections that include maximum and minimum velocities and accelerations . . . . .	68
5.1	Cuboid WSPAM in the unpressurised and pressurized state. The silicone gap (white) and mesh cover (grey) pair block is shown on the left . . . . .	70

5.2	LEGO-built outer mold with plexiglass covers . . . . .	71
5.3	Picture of the alignment procedure and apparatus . . . . .	72
5.4	Pictures of the silicone molding procedure . . . . .	73
5.5	Pictures of laser-cutting the mesh and aligning the silicone core . . . . .	74
5.6	Sample laser cut pattern for WSPAM. The red line indicates the lines the laser cutter needs to cut. . . . .	75
5.7	Pictures of the procedure for precisely wrapping the mesh around the core . . . . .	76
5.8	Parameters of the gap and cover block from top view. $W$ is the thickness of the silicone wall, $L$ is the width of the WSPAM with a square cross section. . . . .	77
5.9	The physical parameters of the gap and cover block . . . . .	78
5.10	The left-hand drawing shows a side view of one cover-gap pair block when pressurized and the right-hand drawing shows the equivalent spring model. Bending of the block was not depicted for illustration purposes . . . . .	82
5.11	Cover section saturation model for the spring constant and the illustration of the silicone behaviour when pressurized . . . . .	85
5.12	Gradient $H_c$ (on the left) and $H_g$ (on the right) WSPAMs at rest and pressurized . . . . .	86
5.13	Simulation and experimental data for $K_g$ in terms of rest heights $H_g$ . . . . .	87
5.14	Simulation and experimental data for $K_c$ in terms of rest heights $H_c$ . . . . .	88
5.15	Pressurized WSPAMs at 3 different $r$ and 2 different $H_b$ values. Note that WSPAMs with lower $r$ have higher $H_g$ and achieve greater angular displacement but at the cost of a distended, “bloated” appearance. . . . .	89
5.16	Simulated and experimental block angular displacement $\theta_{tip}$ with respect to block height $H_b$ and block ratio $r$ in 2D . . . . .	90

# Chapter 1

## Introduction

Research in psychology, animation and human-robot interaction suggests that humans are capable of perceiving and conveying emotion through movement [1, 2]. In robotics, sociable humanoid robots have been studied extensively in the past couple of decades [3, 4, 5, 6]. However, works such as the Kismet robot from MIT [4] mainly focus on facial expressions, and emotional conveyance through the motion of other parts of the body is not considered. Several works (e.g., [7, 8, 9]) investigate the ability of hand and arm movement to convey affect by analysing real actor performances or the re-creation of their motion through computer animation. User perceptual studies [9] indicate that humans are able to accurately perceive the intended emotion from an animation of the real hand or other hand-like structure that performs the same motion. Despite these promising results and the increasing interest in affective motion in human-robot interaction [1], little research has been done on the display of affective movements on robotic hand-like structures. In this work, affective movement or affective motion refer to movement that has the purpose of conveying a particular emotion.

One such hand-like structure is the tentacle mechanism used in the interactive architecture project called *Hylozoic Soil* [10]. Figure 1.1 shows a Hylozoic Soil installation with the tentacle mechanism indicated in red. Each tentacle is able to curl upward in a motion which resembles that of a finger, acting as a potential affective display mechanism. However, one issue with the current system is that the tentacles are driven by shape memory alloys (SMAs), which are inherently slow and therefore are not capable of achieving the high velocities and accelerations which are necessary for emotion conveyance [7, 8, 11, 12].



**Figure 1.1:** Hylozoic Soil installation; the tentacle mechanism is marked by the red oval. This picture is used with permission from PBAI [13].

This limitation of the tentacle system was the motivation for this thesis and led to the design of a simple robotic finger-like mechanism that is capable of performing affective motions in large interactive architecture installations. In this thesis, this mechanism is referred to as the interactive finger-like structure (IFLS).

The design and implementation of the IFLS was initiated by analyzing the motion trajectories to be performed by the IFLS. Samadani *et al.* [9] investigate the conveyance of emotion through human hand movement. Three emotions are considered in their work: joy, anger, and sadness. For each of these emotions, an actor is asked to repeat a single motion—closing and opening a fist—while imbuing the movement with the desired emotion. The human hand motion data is recorded using data gloves and is replayed on a computer-animated structure of the human hand. User perceptual studies indicate that humans are able to accurately perceive the intended emotion from an animation of the hand structure. The human hand data gathered in [9] is used to create the reference trajectories for and determine dynamic performance requirements the IFLS.

The nature of the interactive architecture installation, which often has short installation periods and requires hundreds of actuators, imposes a set of design constraints on the IFLS. Human observers will be interacting with the mechanism both visually and physically, so the mechanism should be safe for physical interaction and possibly encourage it. The IFLS and its motion should not include artifacts that interfere with emotion conveyance. The affective motion trajectories should be followed with minimal error and achieving peak velocity and acceleration in all directions. In this thesis, the IFLS requirements are specified and analyzed.

Surveys of various hand-like and finger-like mechanisms [14, 15, 16, 17] suggest that

common robotic hands are designed mainly for grasping applications in research and industry or for prosthetics. For these robotic hands, the motion trajectory of the fingers or their poses during the motion is not of primary concern. They mostly perform slow motion trajectories for better control over the force and impact of the hand on the object that will be grasped. The slow movement of these robotic hand makes them unsuitable for affective motion applications because high velocities and accelerations are achieved by the fingers during the motion of high-intensity emotions [18, 12, 11, 8, 7]. There are fast robotic hand designs that are capable of performing the affective motion trajectories. However, these robotic hand designs are too expensive and complex for the application considered in this thesis. Cost, complexity, and robustness are critical, since each installation may contain hundreds of these actuators. Thus, a custom design was investigated for the IFLS.

In order to determine the most suitable mechanical design for the IFLS, conventional mechanical designs for robotic hands or fingers are analyzed. These conventional designs consist of a rigid skeleton that give the mechanism its finger-like shape and pose. The skeleton can be actuated using various rotary or linear actuators. The energy of the actuators is transferred to the skeleton using a transmission mechanism, which has several options for its design. The main actuation options for conventional robotic hand designs are analyzed with respect to the IFLS requirements: DC motors, pneumatic artificial muscles (PAMs), hydraulic actuators, and SMAs. Also, the various transmission mechanisms are analyzed in order to determine a suitable transmission mechanism design.

In addition to conventional designs for robotic hands, a recent pneumatic solution called soft pneumatic artificial muscle (SPAM) is also analyzed for the design of the IFLS. Unlike the conventional designs, SPAM is an actuator design with a motion trajectory that resembles that of the human finger. This means that a SPAM-based IFLS would not require a rigid skeleton, nor a transmission mechanism. The SPAM actuator is analyzed with respect to the defined requirements for the IFLS. The result of the analysis shows that SPAMs are a more suitable option for the design of the IFLS in comparison to the conventional robotic finger designs.

Because SPAMs are recent, their fabrication and control is still a relatively new field. This encouraged us to design and implement novel control mechanisms and production methods for these actuators. The first contribution of this thesis is the high-speed dynamic control of SPAM actuators which, as the related work in chapter 4 will discuss, has not been previously achieved. The feedback controller uses innovative pneumatic designs to reduce the noise level of PWM controllers previously used for conventional pneumatic actuators such as PAMs. Feedback on tip orientation is measured using a gyroscopic sensor at the tip of the SPAM. A customized cascade pressure and position controller is implemented to obtain closed-loop trajectory-following on the SPAM. Trajectory-following was achieved

with low tracking error and minimal motion artifacts such as visible vibration.

The second contribution of the thesis is a novel production method that allows easily customizable and robust designs for SPAMs. As will be discussed in depth in chapter 5, current SPAM production methods each have shortcomings that make their consistent and repeatable production difficult, resulting in fragile SPAMs, or SPAMs with undesirable appearance and motion. The novel production method for SPAMs in this work, called the wrapped SPAMs (WSPAMs), rectifies all of these issues with innovative production methods. Additionally, it significantly simplifies the customization of the motion trajectory of these actuators.

The third contribution of this thesis is modeling the steady-state orientation of pressurized WSPAMs. This model will simplify the design of the WSPAMs as the geometrical parameters of the design can be determined based on the desired steady-state orientation. In order to confirm the theoretical model, first the parameters of the model are estimated using experimental analysis on special WSPAMs specifically designed for parameter estimation. The estimated parameters are then used to perform steady-state tip orientation estimation for 6 different WSPAM designs and verify the performance of the model. The model is capable of estimating the steady-state orientation of the WSPAM and thus can be used for the design of these actuators. A provisional patent has been filed for the WSPAM production, modelling, and control method.

The rest of the thesis is organized as follows: in chapter 2, the affective motion trajectories of human hand data are analyzed in order to extract the dynamic requirements of the IFLS. In addition, the application-based requirements on the design of the IFLS are outlined. In chapter 3, a review of existing actuator solutions is provided and the various conventional robotic hand and finger designs are analyzed with respect to the IFLS requirements. SPAM-based designs are also reviewed and a SPAM-based solution for the IFLS is analyzed and its performance compared to that of the conventional robotic designs. In chapter 4, the controller solution for the SPAM actuator is discussed. First, the related work on pneumatic controllers is presented. Second, an innovative solution that enables the application of pneumatic controller designs to SPAMs is introduced. Third, experimental results confirming the performance of the controller are discussed. In chapter 5, existing approaches for SPAM production are first reviewed. Then, the production method for the novel SPAM design, the WSPAM, is introduced. Next, the steady-state model for the WSPAMs is presented. Lastly, chapter 6 concludes the thesis and discusses directions for future work.

# Chapter 2

## IFLS Design Requirements

There are a number of electromechanical solutions that can be developed into the IFLS that are capable of performing affective motion. In order to narrow down the number of possible solutions and to eventually choose one that is capable of performing affective motion in the context of interactive architecture, a set of design requirements are formulated in this chapter. In order to establish these requirements, affective motion trajectories generated by a human demonstrator are analysed and their kinematic and dynamic characteristics are determined. These characteristics are translated to design requirements that must be met by the motion of the IFLS. Also, the sculpture is a component of an interactive architecture installation. This application introduces an additional set of requirements on the design of the IFLS.

In this chapter, first, the motions to be reproduced by IFLS are analysed and the characteristics of the motion are extracted in order to elaborate the design requirements. Second, the design requirements are categorized and summarized.

### 2.1 Analysis of Human Hand Affective Motion Trajectories

The affective hand motion trajectories investigated in [9] are the basis for the motion trajectories that must be performed by the IFLS. Samadani *et al.* [9] investigate the perception, conveyed through hand movements, of three emotions: joy, anger, and sadness. The motions are performed by a human actor wearing a data glove (ShapeHand from Measurand). The recorded data is used to create an animated model of the movements

which are displayed to human observers using computer animations. Observers are asked to rate the affective content of these animations. The work concludes that the investigated hand motion trajectories successfully convey the intended emotion, and that participants can reliably detect the intended emotion from the animation. Figure 2.1 shows frames of the hand animation of the recorded affective motion. In the collected dataset for the affective hand motions, the hand mainly performs opening and closing of the fist. During these motion trajectories, the motion of the fingers are very similar and there is little movement out of the sagittal plane of each finger (i.e., finger spreading). This is an important characteristic that simplifies the requirements on the motion of the dynamic sculpture. It means that simpler mechanisms with fewer degrees of freedom than the human finger can be capable of performing these motions. In this chapter, analysis is conducted on the motion of the human hand during affective trajectories, in order to determine the kinematic complexity of the IFLS necessary for performing the demonstrated affective motions.

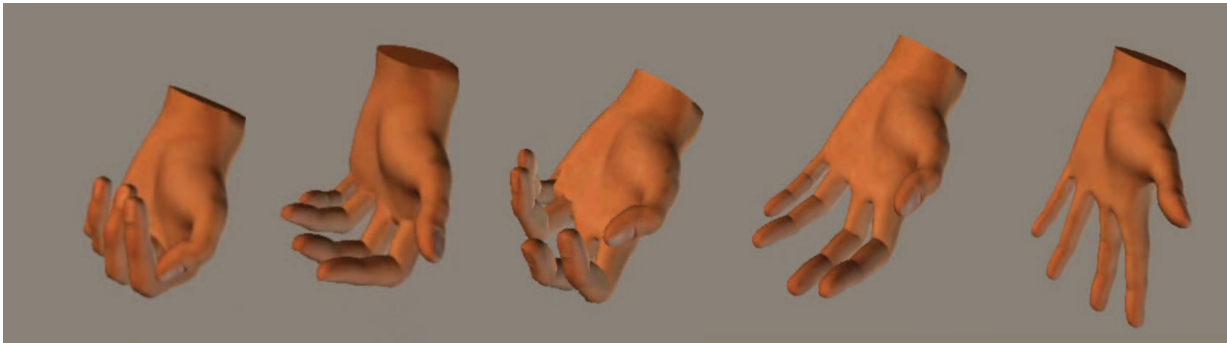


**Figure 2.1:** Frames of the animation of the human hand performing affective motion [9]

The data glove measures the movement of 3 joints in each finger including the thumb. The kinematic structure of the hand is illustrated in figure 2.2. For each joint, angular motion data is recorded for all three axes of rotation, i.e., about x, y, and z. The angular data recorded for each joint is relative to the local frame. The joint's local frames are aligned with the global frame when the fingers including the thumb are fully extended (i.e., in the pose that the little finger has in the figure). The naming convention for the three joints of each finger plus the end effector (EE) are also depicted on the little finger. The angular motion trajectories were recorded as time series data with a sampling rate of 84.232 Hz.

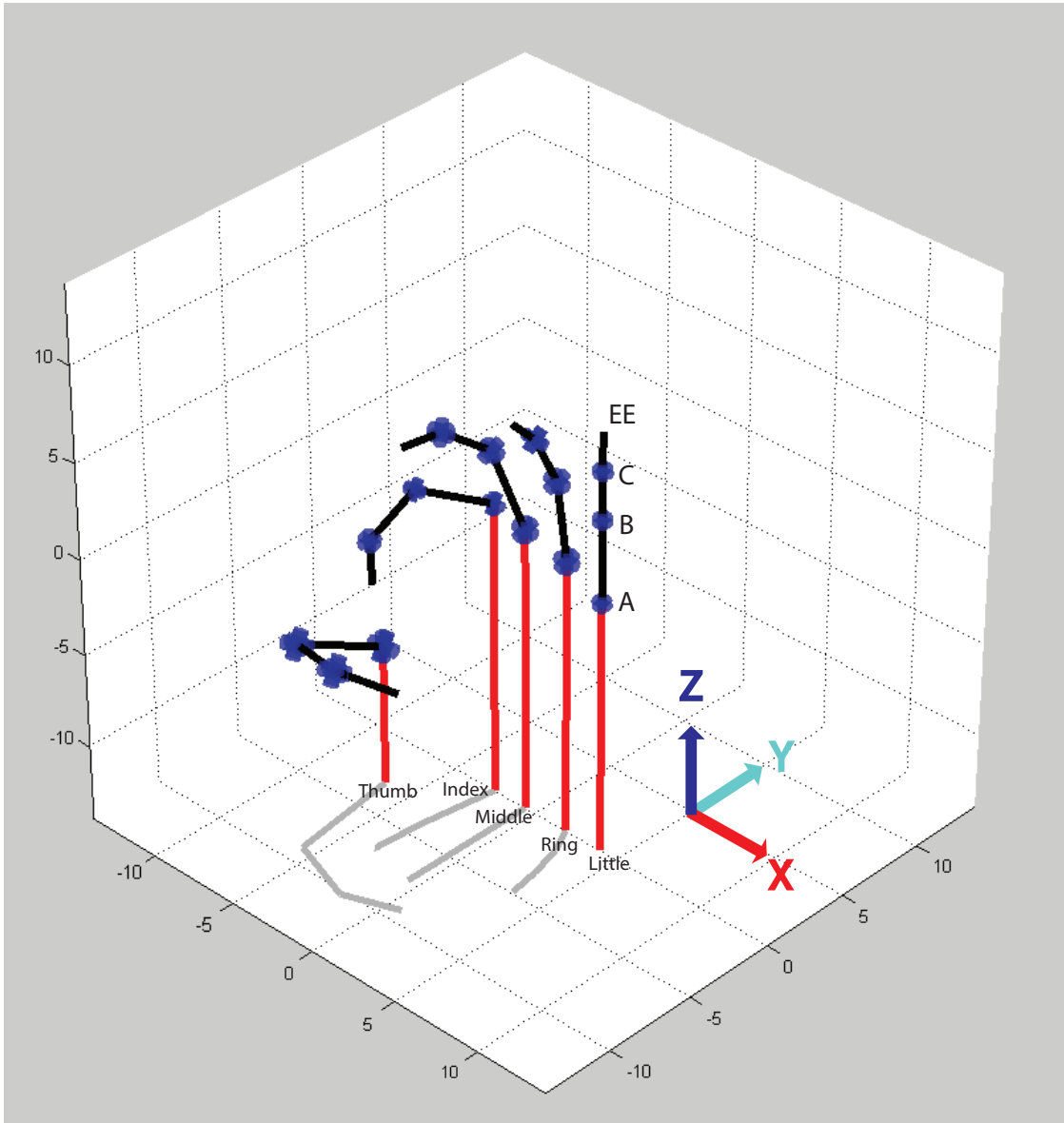


**Figure 2.2:** Kinematic structure of the hand recorded by the data glove [9] showing the orientation and the location of the joints

Thus, the recorded motion trajectory of the hand consists of  $3 \times 3 \times 5 = 45$  time series data columns. Many of the joints in the human hand cannot perform angular movement in all three DOFs. The exact number and complex nature of the DOFs of the thumb and

the palm are still under debate [19]. However, the B and C joints of the index, middle, ring, and little fingers, (i.e. the non-thumb fingers) can only rotate around the x-axis. Also, the A joints of the non-thumb fingers cannot rotate around the z-axis. Lastly, the C joint of the thumb can only rotate around the y-axis. Thus, only 23 time series data columns contain information about the motion of the hand. This number of DOFs is in line with the literature which models the hand with a range of 22-33 passive and active DOFs depending on the application [19].

Figures 2.3-2.5 illustrate the time plots of the 45 DOFs recorded by the glove for the three emotions of anger, joy, and sadness respectively. The plots contain multiple opening and closing motions. As expected, it can be observed that the physically unfeasible DOFs such as the y and z axes DOFs of the C joints of the non-thumb fingers don't have any movement. From the overlaid plots of the non-thumb fingers, it can be observed that the joints of these fingers perform very similar rotational movements during the trajectories of all three emotions (i.e., are coupled). The A joints of the non-thumb fingers mainly rotate around the x-axis and their rotation around the y-axis is minimal. The movements of the joint angles of the thumb are also illustrated in these figures.

The motion of the thumb is more complicated and involves more DOFs. This can also be observed from the plots as both joint B and joint A of the thumb exhibit movement in all three DOFs. However, for all three joints of the thumb, the motion around the y-axis is dominant. In addition, figures 2.3-2.5 illustrate the orientation of the end effectors of the fingers in Euler angles with respect to the global frame. The end effector orientations were obtained through the forward kinematic transformation. The end effector trajectories suggest that the end effectors of the non-thumb fingers mainly rotate about the x-axis and the end effector of the thumb mainly rotates about the y-axis during these affective motions. As can be seen from figure 2.2, for the non-thumb fingers, the bi-directional rotation of the end effector around the x-axis translates to the end effector approaching and retreating away from the palm of the hand, i.e. performing flexion and extension. Because the thumb is lowered and positioned in front of the palm, the rotation of the end effector of the thumb around the y-axis also translates to a similar flexion and extension motion. Therefore, to reproduce the motions contained in this dataset, it is sufficient that the IFLS performs end effector rotations around 1 axis. In other words, the IFLS representing the non-thumb fingers will only need to perform motion in the ZY plane, while the IFLS representing the thumb will only need to perform motion in the ZX plane.

Figures 2.3-2.5 also confirm that the A, B, and C joints of each finger rotate at almost the same time and with a similar rate i.e. their motion is coupled. This occurs in the trajectory of all three emotions. The coupled motion of the finger joints is in line with the literature which suggests that most common motions of the human hand, which are

often grasping tasks, involve the coupled motion of the fingers' joints [20]. In relation to the rotation of the end effector of the fingers, the coupled motion means that the joints contribute to the rotation of the end effector all at the same time. This further simplifies the motion that the IFLS needs to perform. It suggests that the joints that will contribute to the rotation of the end effector of the IFLS can all be coupled and thus can all be actively controlled by one actuator.

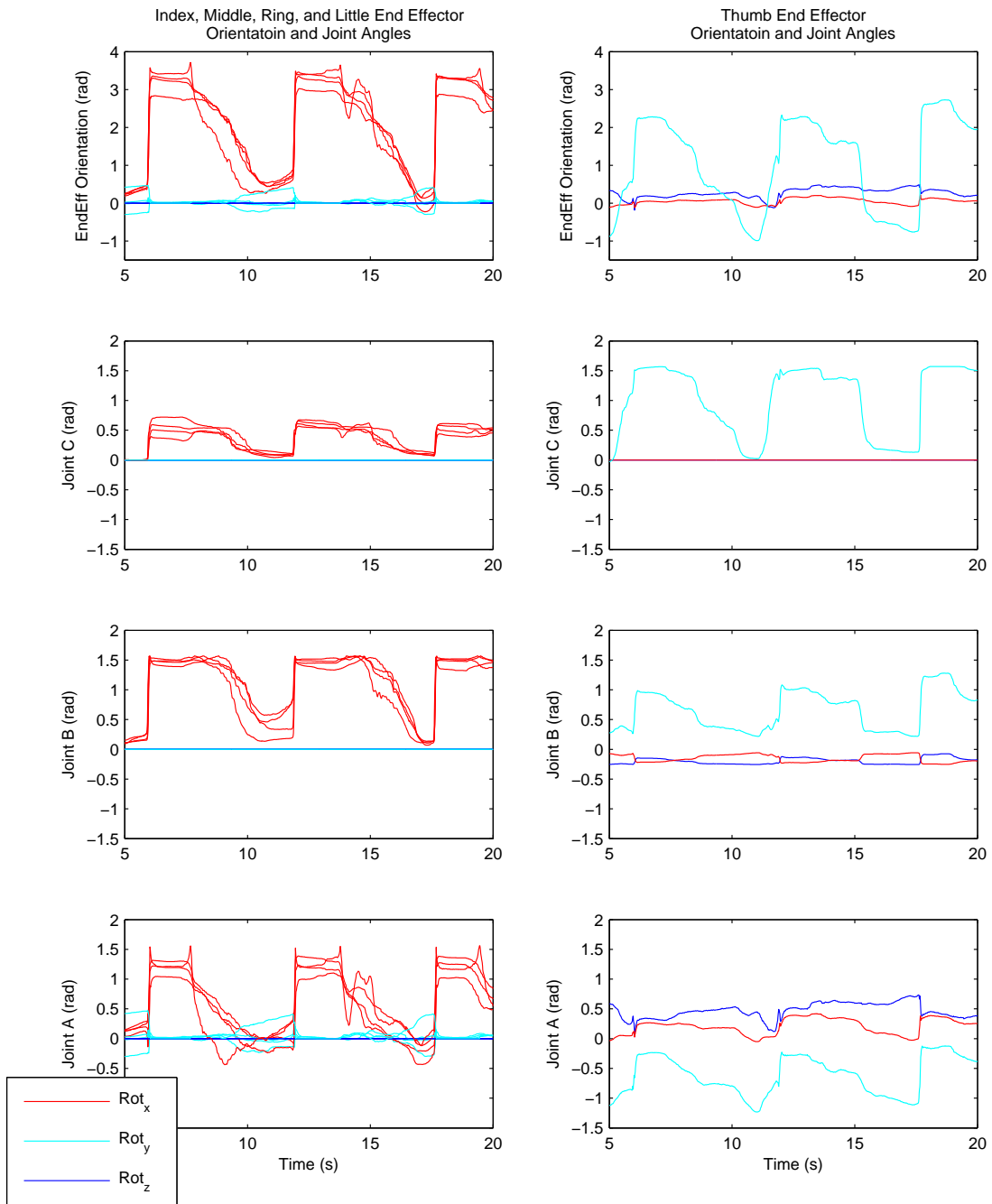


**Figure 2.3:** The local joint angle and the global end effector orientation of the five fingers during the trajectory for anger (Note, the y-axis scales are different between the subplots)

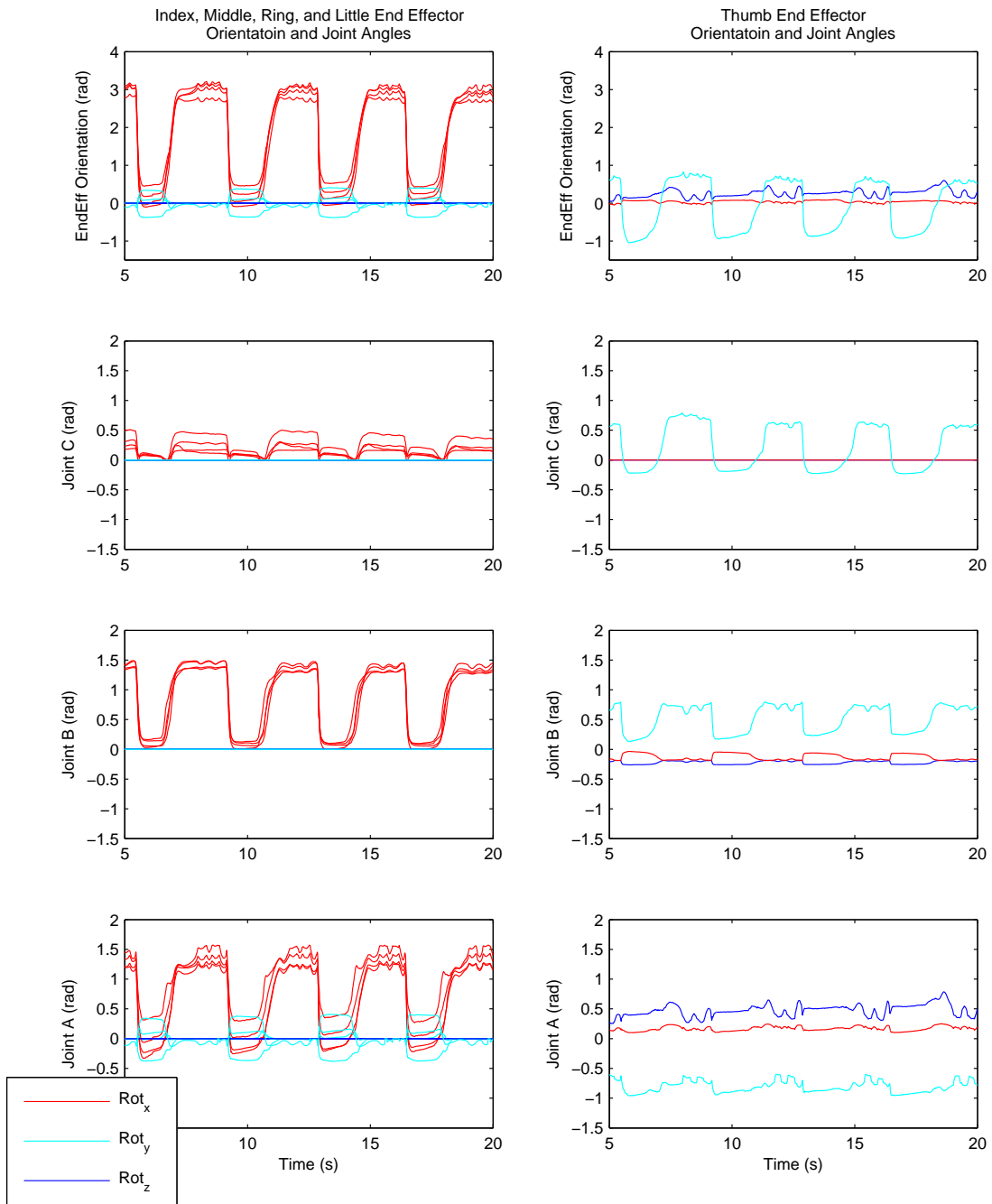


**Figure 2.4:** The local joint angle and the global end effector orientation of the five fingers during the trajectory for joy (Note, the y-axis scales are different between the subplots)

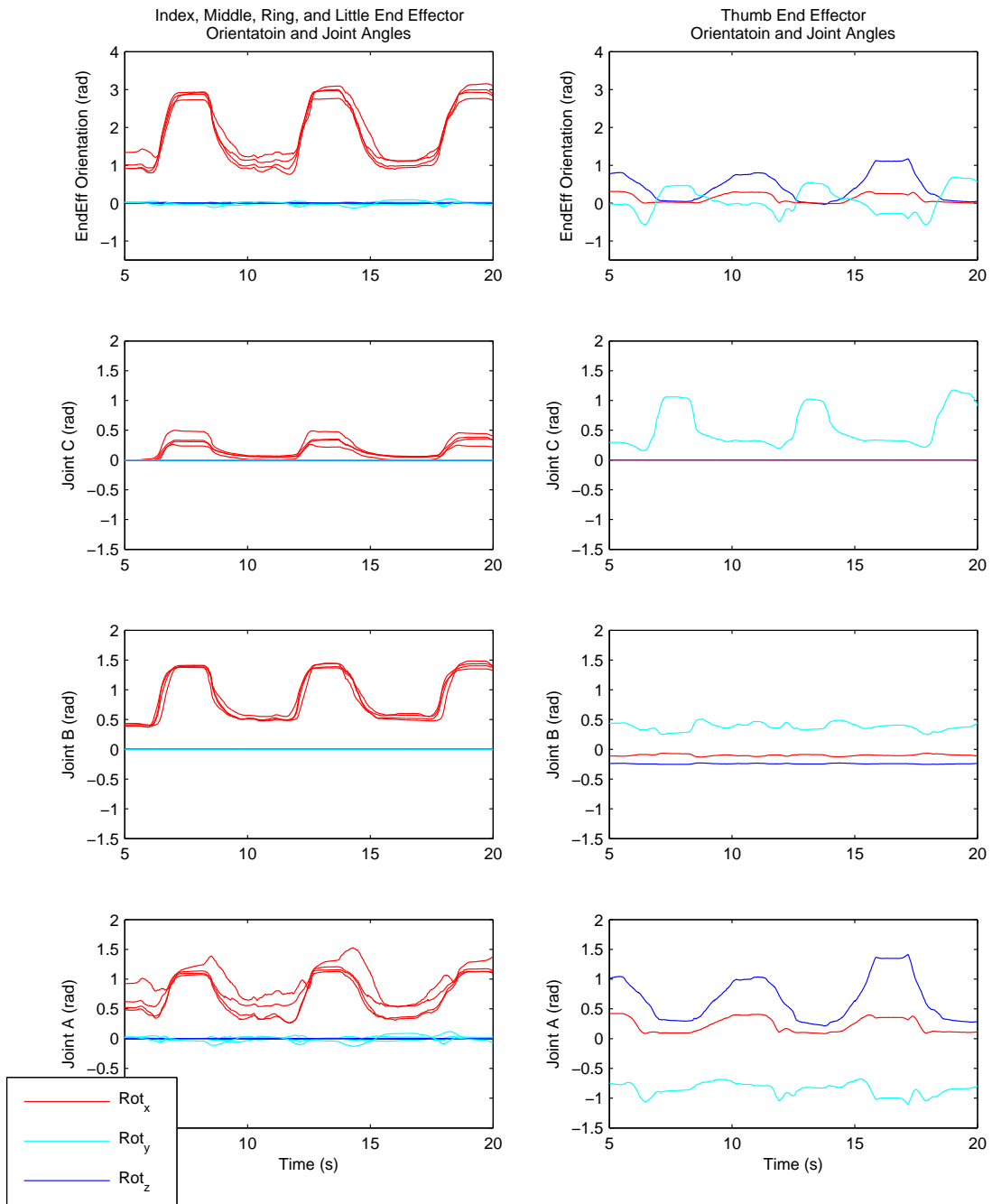


**Figure 2.5:** The local joint angle and the global end effector orientation of the five fingers during the trajectory for sadness (Note, the y-axis scales are different between the subplots)

## 2.2 Design Requirements

Multiple engineering designs are possible for the IFLS. The first step in choosing between these candidate designs is defining a set of requirements as the decision criteria. The requirements for the design of the IFLS can be classified into three categories. The first category of requirements stems from the target application, as the IFLS will be a component of an architectural exhibition. The second category relates to the physical and visual interaction of the sculpture with humans. The third category of requirements is dictated by the desired kinematic and dynamic motion response of the sculpture. These requirements apply to the entire electromechanical IFLS system.

The requirements stemming from the architectural application of the IFLS are not absolute thresholds and are measured qualitatively and relatively between the candidate designs. For example, if a particular design meets some criteria but not others, workarounds can be applied to accommodate a specific design, by modifying other parts of the installation or reducing the functional capabilities. For example, in the case of the Hylozic Soil installations presented in figure 1.1, a mechanism called the breathing pore was implemented in the installation that used Shape Memory Alloys (SMAs) for actuation. SMAs are highly desirable for the actuation of the breathing pore because they produce smooth motion without any noise. However, SMAs have low bandwidth and can only produce slow motions. Rather than rejecting SMAs as a result, only slow motion trajectories for the breathing pore were designed implemented as part of the installation and high velocity motions were avoided as a compromise to accommodate the low actuator bandwidth while benefiting from SMA's other desirable properties.

At a high level, the electrical part of the system consists of a controller that will control the motion of the sculpture, possibly with feedback from sensory mechanisms. For the mechanical part of the system, if conventional robotic techniques are to be used, the system consists of a rigid skeleton, a actuation mechanism that enables the skeleton to dynamically move, and a transmission mechanism that transfers the energy of the actuator to the skeleton. More recent robotic designs can also be considered for the IFLS that combine the three parts of the conventional designs. In these recent designs, the motion trajectory of the actuator resembles trajectories intended for the structure and thus the need for a separate skeleton and the necessary transmission mechanism is eliminated. The electronic part of the system interacts with the mechanical part through the driving system of the actuation mechanism, which also needs to comply with the requirements of the IFLS.

In this section the three requirement categories are presented. For each requirement category, first their importance with respect to the application of this work is discussed.

Second, the sub-categories of requirements are introduced and their effect on the electromechanical design is analysed. Third, qualitative or quantitative measures are presented for evaluating how well each of the requirements is satisfied.

### **2.2.1 Application-Specific Requirements (Interactive Architecture)**

The ultimate goal of the developed system is to enable affective motion generation within the domain of interactive architecture. Consequently, there are requirements on the design of the IFLS that stem from the architectural side of the work. As part of an interactive architecture exhibition, similar to the tentacles in the Hylozoic Soil series shown in figure 1.1, large numbers of IFLS modules are required for an installation. Therefore, cost is an important factor. The exhibitions are held in various cities and countries and are usually prepared for only a few months in advance. Therefore, the production of the IFLS modules should not require excessive person-hours. As part of an artistic project, the design of the IFLS should be customizable, i.e., the size, the kinematic structure, the orientation, and the location of the IFLS modules should be modifiable. In addition, the design should use components that are easily available. Lastly, the maintenance of the IFLS modules should be low cost and require little effort and time.

The architectural constraints discussed in the previous paragraph are: ease of production, cost of production, customizability, component availability, and maintenance. Within these constraints, customizability, component availability, and maintenance are qualitative constraints and are best evaluated when the candidate designs are compared against each other with respect to these constraints. Ease and cost of production are constraints that can be quantified. However, instead of determining precise limits on these constraints in terms of person-hours or dollars and analyzing each candidate design against them individually, it is more practical to comparatively analyze these requirements as well.

### **2.2.2 Human Interaction Requirements**

The IFLS mechanism is intended to interact with human observers both physically and visually. The mechanism creates a visual interaction with the human observers by performing movements that convey emotions. It is important that this affective interaction is not impacted by artifacts in the movement of the mechanism. As figures 2.3-2.5 illustrate, the motion of the fingers during the affective trajectories is very smooth. However, in robotic systems, there are common issues in both the control and the mechanical system that can

cause undesirable artifacts in the motion of the mechanism. These artifacts often result in robotic-looking and unnatural motion, and can significantly hinder the ability to convey affect via the mechanism's movement. Thus, the mechanical and the controller design of the system must avoid these artifacts as much as possible. In the mechanical design, non-linear responses such as stiction, which causes jerky movements, should be reduced. In the design of the controller, aggressive controls that cause artifacts such as visible vibration should be avoided as much as possible.

The physical interaction with the mechanism occurs when the human observer purposely or accidentally touches the sculpture. In both cases, a compliant interaction with the mechanism is far more desirable than an interaction with a stiff mechanism. A compliant mechanism will be considerably safer during the accidental bumps. It will also reduce the mechanical feeling of the interaction, which as discussed can hinder the affective capabilities of the mechanism. Therefore, compliance is a highly desirable feature for the IFLS.

### 2.2.3 Dynamic Requirements

It has been shown by a number of researchers that for conveying emotion through movement, the dynamics of the motion is critical to successfully convey a desired emotion through movement [18, 12, 11, 8, 7]. These works suggest that for higher-intensity emotions such as anger and joy, faster velocities and accelerations are required; while, for lower-intensity emotions such as sadness, lower velocities and accelerations are required. The velocities and the accelerations of the orientation of the end effector of the five fingers during the trajectories of the three emotions are presented in figures 2.6 and 2.7. These plots only include the velocities and accelerations of one closing and opening action of the human hand. The velocity and acceleration values were computed by discrete differentiation using Simulink. From these plots, it can be observed that the affective motion trajectories are in line with the literature. Higher intensity emotions, joy and anger, have higher velocities and accelerations than the lower intensity emotion of sadness. The motion for anger starts with a fast flexion of the fingers or making a fist; and is followed by a slow extension of the fingers or opening of the fist. The motion for joy is opposite to anger in the sense that the motion starts with a slow flexion of the fingers and is followed by a fast extension of the fingers or opening of the fist. Lastly, being a low intensity emotion, the motion for sadness starts by a slow flexion of the fingers and is then followed by a slow extension of the fingers.

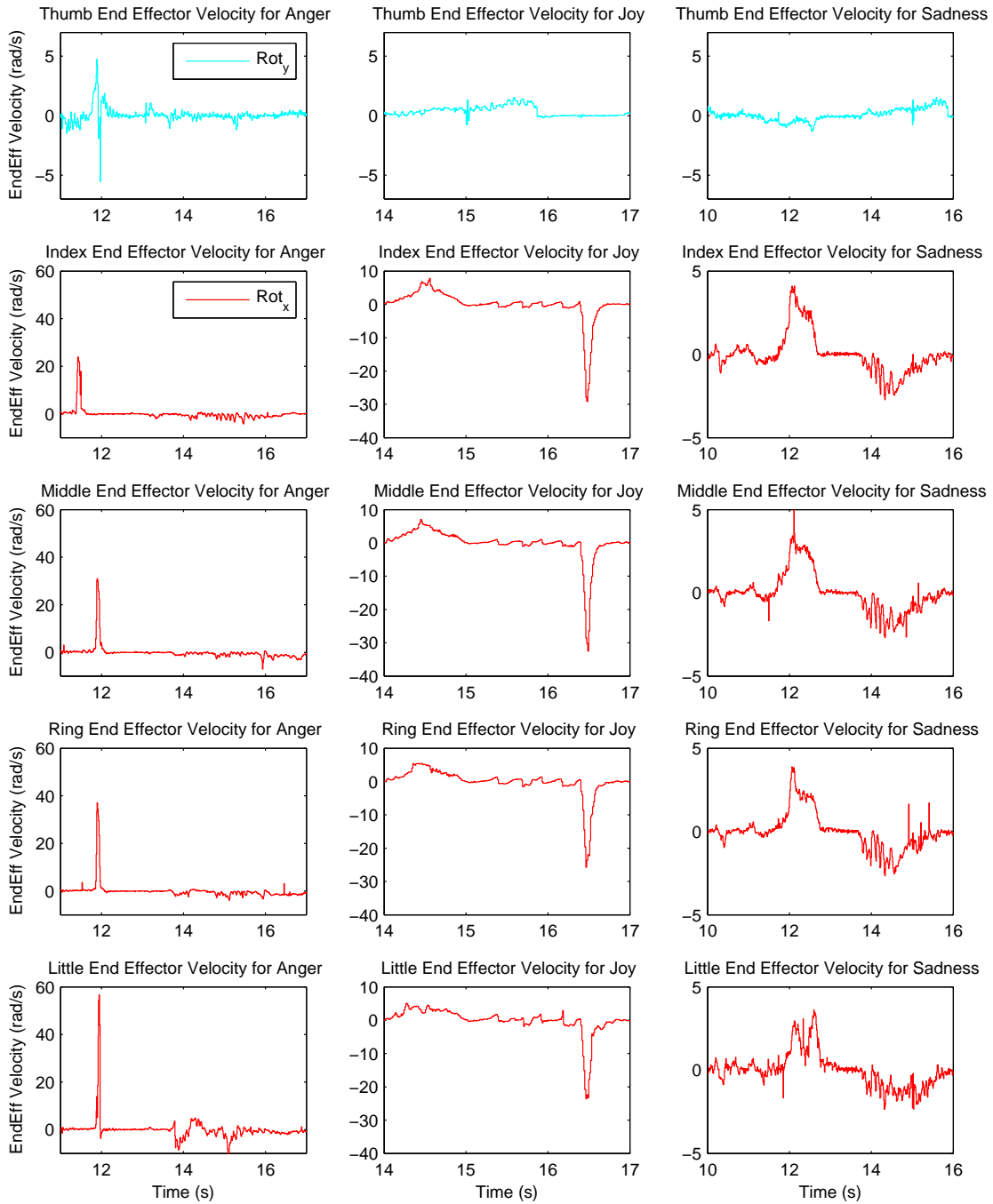


**Figure 2.6:** End effector angular velocity of each finger for joy, anger, and sadness (Note, the y-axis scales are different between the subplots)

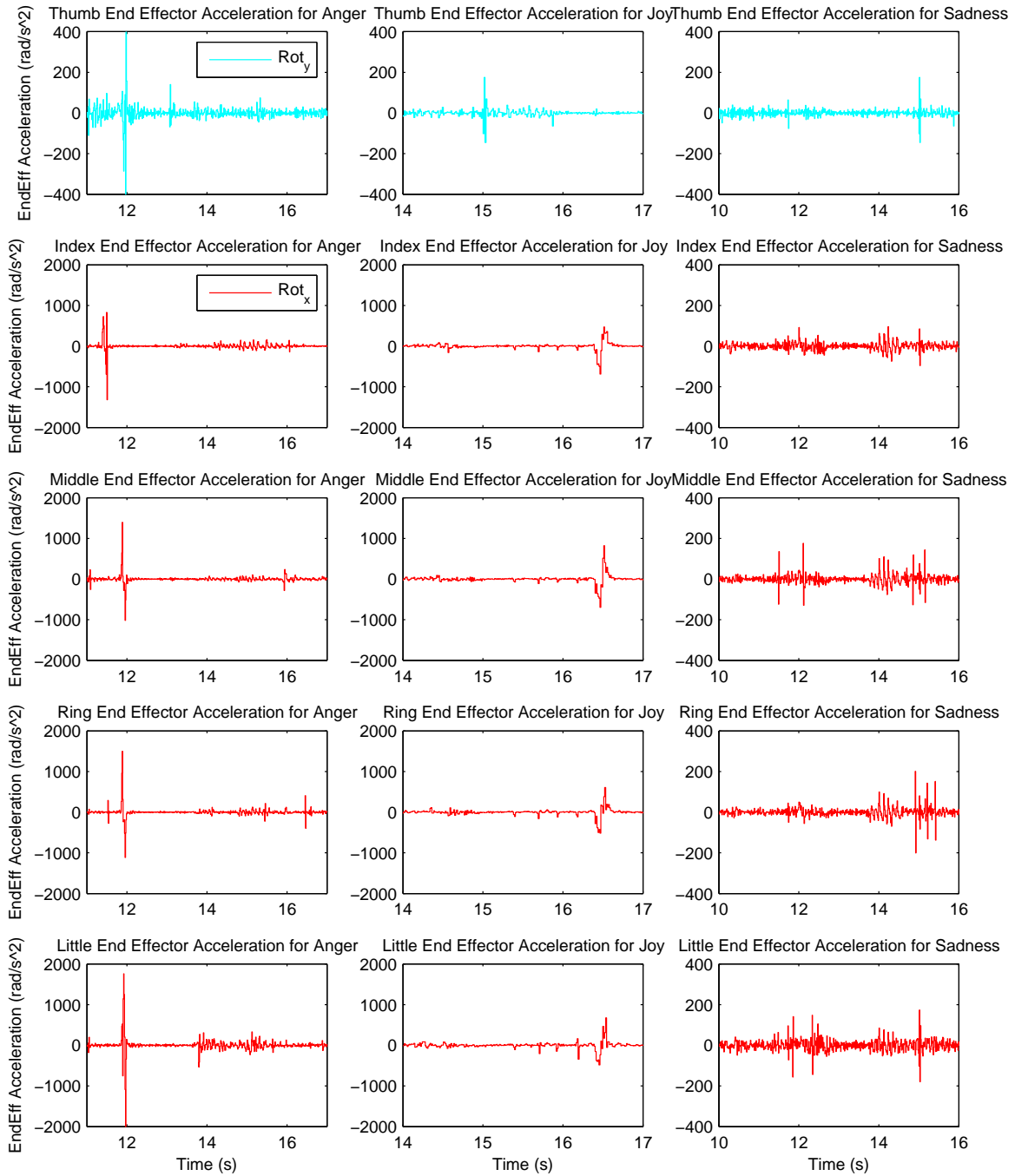


**Figure 2.7:** End effector angular acceleration of each finger for joy, anger, and sadness (Note, the y-axis scales are different between the subplots)

Tables 2.1 and 2.2 present the maximum and minimum end effector angular velocities and accelerations for all fingers during the three emotions. Note that the data for the thumb is not included in the tables as its velocity and acceleration values are considerably smaller than those of the other fingers.

**Table 2.1:** Maximum and minimum end effector angular velocity in  $rad/s$  for joy, anger, and sadness

	Anger		Joy		Sadness	
	Max	Min	Max	Min	Max	Min
<b>Index</b>	23.85	-6.099	7.779	-29.15	4.103	-2.72
<b>Middle</b>	30.94	-5.014	7.044	-32.53	5.103	-2.691
<b>Ring</b>	37.09	-5.588	5.426	-25.72	3.882	-2.662
<b>Little</b>	56.69	-4.941	5.088	-23.6	3.632	-2.353
<b>RANGE</b>	32.84	1.159	2.691	8.926	1.47	0.3676
<b>MEDIAN</b>	34.01	-5.301	6.235	-27.43	3.992	-2.676

**Table 2.2:** Maximum and minimum end effector angular acceleration in  $rad/s^2$  for joy, anger, and sadness

	Anger		Joy		Sadness	
	Max	Min	Max	Min	Max	Min
<b>Index</b>	828.3	-1318	468.3	-686.4	95.4	-95.4
<b>Middle</b>	1395	-1016	818.9	-695	175.9	-128.8
<b>Ring</b>	1500	-1114	604.6	-517.9	200.7	-200.7
<b>Little</b>	1758	-3661	675.2	-484.4	173.5	-179.6
<b>RANGE</b>	929.7	2645	350.6	210.6	105.3	105.3
<b>MEDIAN</b>	1448	-1216	639.9	-602.1	174.7	-154.2

It can be observed that, between all three emotions, the fingers achieve their maximum velocity and acceleration values during the motion for anger. In other words, active flexion motions with the highest velocities and accelerations occur during anger. Within the maximums of anger, there is a notable variation between the fingers, with the index

finger showing the smallest flexion velocity and acceleration. Thus, in order to ensure the resemblance of the fast flexion motion of at least one of the fingers during anger, the IFLS has to achieve the index finger’s end effector orientation velocity of  $23.8rad/s$  and acceleration of  $828rad/s^2$ . While these values are a lower limit on the maximum requirements, in order to assure a more accurate resemblance of the fast dynamics of anger, values closer to the median of anger’s maximum velocities ( $34rad/s$ ) and accelerations ( $1450rad/s^2$ ) are preferable.

Between all three emotions, the minimum velocity values are achieved during the motion for joy and minimum acceleration values are achieved during anger. However, as can be observed from the plots of anger in figure 2.7, these accelerations correspond to the fingers coming to a sudden stop, at high velocities, by hitting the palm of the hand. Only active responses of the fingers impose requirements on the design of the actuation mechanism and therefore, minimum acceleration values during anger will not be considered in the requirements analysis. This means minimum accelerations are also achieved during the motion for joy. In other words, active extension motions with the highest velocities and accelerations occur during this emotion. Within the minimums of joy, the little finger achieves the smallest extension velocity and acceleration. Therefore, the IFLS has to at least achieve the little finger’s end effector orientation velocity of  $-23.6rad/s$  and acceleration of  $-484rad/s^2$ . However, again, velocities and accelerations near the median of this column, which are  $-27.4rad/s$  and  $-602rad/s^2$ , would be preferred. Table 2.3 presents the required and the desired velocities and accelerations for the IFLS in terms of the flexion and extension motions of the mechanism.

**Table 2.3:** Required and desired velocity and acceleration of the flexion and extension motion of the IFLS

	Velocity ( $rad/s$ )		Acceleartion ( $rad/s^2$ )	
	Flexion	Extension	Flexion	Extension
<b>Required</b>	23.85	23.6	828.3	484.4
<b>Desired</b>	34.01	27.43	1448	602.1

## 2.3 Summary of Design Requirements

The requirements on the design of the IFLS are summarized in table 2.4.

**Table 2.4:** Summary of Design Requirements

<b>Interactive Architecture</b>	<b>Ease of Production</b>	Production effort should require low person-hours as large numbers of IFLS might be required for a single installation.		
	<b>Cost of Production</b>	The per unit cost of the IFLS mechanism should be low as large numbers might be required for a single installation.		
	<b>Customizability</b>	Being part of an architectural project, the design of the IFLS and its motion trajectory should be amenable to change and modification.		
	<b>Component Availability</b>	Difficult to source components should be avoided in the design of the IFLS.		
	<b>Maintenance</b>	The installations might not have any supervision while in operation, thus maintenance should be as easy, infrequent, and low-cost as possible.		
<b>Human Interaction</b>	<b>Visual Interaction</b>	No artifact in the behavior of the IFLS mechanism should interfere with the affective capabilities of the mechanism. The motion of the IFLS and its poses during motion should be natural and finger-like.		
	<b>Physical Interaction</b>	The IFLS has to be compliant in case of accidental collision with a human user. Compliant behaviors that can enhance physical interaction are also desired.		
<b>High Velocity and Fast Dynamics</b>	<b>Velocity (rad/s)</b>	Desired	Flexion	34.0
			Extension	27.4
	Required	Flexion	23.8	
		Extension	23.6	
	<b>Acceleration (rad/s<sup>2</sup>)</b>	Desired	Flexion	1450.0
			Extension	602.0
Required		Flexion	828.0	
		Extension	484.0	

# Chapter 3

## Mechanical System Design

This thesis investigates the construction of a hand-like dynamic structure for affective motion reproduction. Numerous designs for robotic hand or hand-like robots exist, which use various mechanical and electrical techniques to achieve a number of tasks such as grasping, gesturing, and exoskeleton assistance [14, 15, 16, 17]. Conventional mechanical designs of robotic hands consist of the following three components: actuator, transmission, and skeleton structure. The actuator provides mechanical energy which the transmission transfers to the joints on the skeleton structure. In recent years, a category of pneumatic actuators has emerged that eliminates the need for a separately designed skeleton structure, since the structure is incorporated into the design of the actuation mechanism. The motion trajectory of these pneumatic mechanisms can be programmed to be very similar to the closing and opening motions of the fingers.

For the mechanical design of the IFLS, initially, the actuators and transmission designs of the more conventional robotic hands are evaluated against the requirements. The selected designs are then compared against the more recent pneumatic actuators in order to select a suitable design for the IFLS.

### 3.1 Conventional Mechanical Designs

In conventional robotics, finger-like mechanisms have been developed [14] as small-sized manipulators with a series of revolute joints, connected to each other by straight rigid links. Since the IFLS's end effector only needs to rotate around one axis, its robotics manipulator design will consist of parallel revolute joints that could be coupled and are

linked together by the skeleton of the mechanism. A sample two joint IFLS design is illustrated in figure 3.1. The actuator design in this mechanism provides the mechanical energy to rotate these joints. This mechanical energy is transferred from the actuators to the joints by a transmission mechanism.

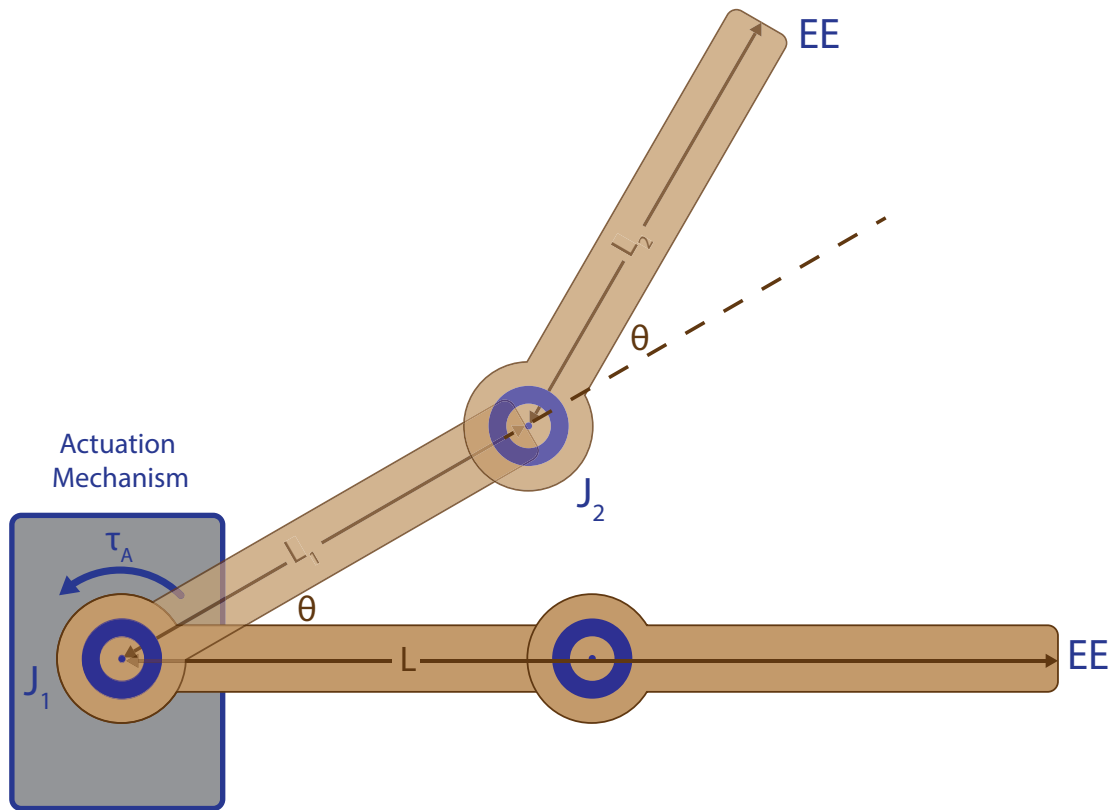


**Figure 3.1:** Sample robotic manipulator design for the IFLS

In this section, first the actuator mechanisms used in conventional robotic hands are investigated and actuation design candidates are chosen. Each design is evaluated against the three categories of requirements and the possibility of using the design for the IFLS is discussed. For the selected candidates, common transmission mechanisms are presented and are evaluated against the requirements. Based on the evaluations, suitable actuation and transmission pairs for implementation in the IFLS are recommended.

### 3.1.1 Actuators

Four of the main categories of actuators conventionally used for actuating robotic hands are: electromagnetic direct current (DC) motors, pneumatic actuators, hydraulic actuators, and SMA actuators [14, 15]. These actuation solutions are discussed individually in this section. A brief description of the physical phenomena that enable the output mechanical energy of the actuation concept is provided and the different variations of each actuation concept are analysed. In addition, methods for driving the actuation mechanism and controlling its mechanical energy are discussed. Lastly, each solution is evaluated with respect to the three categories of requirements.

#### DC Motors

Within all the investigated robotic hand designs [14, 15, 16, 17], DC motors are the most common actuation mechanism. These actuators convert electrical energy to mechanical power by opposing magnetic interaction between the stator and the rotor. The two main designs for DC motors are brushed and brushless DC (BLDC) motors. Brushed DC motors are cheaper, more easily available, produce more power and torque, and do not require expensive controller circuitry. However, brushed DC motors have low efficiency which causes more heat and noise, and also have a shorter life time due to the friction on the rotors [21]. BLDC motors provide better efficiency by eliminating rotor friction, achieve higher speed, have smoother torque outputs, and have longer lifetimes. The downsides of the BLDC motors are: higher cost, requirement for control circuitry that adds additional cost, and lower availability and variability in size [21].

The most common method for controlling the output power of both DC motor designs is to use digital pulse width modulated (PWM) electrical signals as the input of the motor. As a high-level overview, PWM signals allow packets of energy into the motor at a specific frequency. Changing the size of these energy packets, which corresponds to the duty cycle of the signal, results in changing the energy output of the motor. The most important benefit of using PWM signals is that they can be produced by commonly available digital microcontrollers. Depending on the impedance of the motor, the duty cycle of the PWM signal translates to a specific voltage at the input of the motor. The relationship between the duty cycle and the voltage is linear, making the control of the driver system of the motor relatively simple.

DC motors can rotate in both directions, therefore with the proper design of the transmission mechanism, they can provide bidirectional motion for the joints. This can considerably reduce cost and simplify control, as one actuator can produce active actuation for a

joint in both directions. DC motors in general operate at high angular velocities and low output torques. A variety of torque increase mechanisms exist that can bring the torque and velocity values of DC motors to more suitable ranges. Conventionally, gearboxes have been used to achieve torque increase for DC motors. The simple design of gearboxes makes them cheap and available in a variety of designs and torque increase ratios. Gear backlash or free play is one of the main issues with gearboxes, reducing efficiency and complicating control [21]. For the affective applications of the IFLS, backlash is particularly disadvantageous as it is a non-linear behaviour that will result in unnatural motions. Careful and high-precision designs and performing selective assembly and gear centring can significantly reduce backlash [21]. However, these actions can also significantly increase cost and production time and effort.

The authors in [21] suggest numerous alternative torque increase mechanisms to gearboxes. One of these solutions is the harmonic drive mechanism, which provide high torque increase ratios in compact sizes and do not suffer from backlash. On top of the general benefits of harmonic drives, the high speed robotic hand by Namiki *et al.* [22] provides results that suggest the high velocity and acceleration requirements on the IFLS can be achieved by DC motors paired with harmonic drives. Namiki *et al.* [22] use custom built BLDC motors that allow high current flows into the motor for short periods of time. This modification allows for fast velocities and accelerations to be achieved for those short time periods, before the motor overheats. In addition, by using harmonic drives they eliminate backlash, making it possible to perform high gain control that enables the mechanism to achieve considerably higher velocities and accelerations. In their results, Namiki *et al.* achieve a maximum angular velocity of  $300rpm$  and a maximum torque of,  $1.71Nm$ .  $300rpm$  translates to  $31.4rad/s$  in both directions of motion. This angular velocity is well above the minimum required flexion velocity of  $23.8rad/s$  and extension velocity of  $23.6rad/s$ . However, if the torque provided by the actuator is not sufficient to produce the required angular accelerations, the velocity trajectory of the affective motions cannot be followed properly and this can interfere with the affective capabilities of the motions.

The possibility of achieving the required acceleration is examined by looking at the theoretical amount of torque needed from the actuator that will enable the IFLS to achieve the required acceleration. In order to proceed with this analysis, the IFLS is considered to be a robotic manipulator with  $n$  parallel revolute joints. Figure 3.1 illustrates a sample IFLS design with  $n = 2$  joints. All the joints  $J_i, i > 1$  are considered to be coupled to the actuation mechanism on  $J_1$  with unity torque increase ratios and the assumption that no energy is lost due to friction. In other words, for any  $n > 1$  the mechanism will be underactuated. The coupling of the joints means that during the motion of the IFLS, the torque needed from the actuator is

$$\tau_A = \tau_1 + \tau_2 + \dots + \tau_n \quad (3.1)$$

with  $\tau_i, i = 1, 2, \dots, n$  being the torque required from the  $i^{th}$  joint that enables the end effector to follow the desired angular acceleration trajectory. The angular acceleration at the end effector is  $\alpha_{EE} = \alpha_1 + \alpha_2 + \dots + \alpha_n$  or the sum of the angular accelerations of the joints. Because of the unity torque increase ratio, the angular acceleration of all the joints are equal. Thus,

$$\alpha_i = \frac{\alpha_{EE}}{n}, i = 1, 2, \dots, n. \quad (3.2)$$

The required torque from each joint is:

$$\tau_i = \alpha_i I_i, i = 1, 2, \dots, n \quad (3.3)$$

with  $I_i$  being the moment of inertia that the  $i^{th}$  joint sees. Because of lower mass and shorter length,

$$I_i < I_{i-1}, i = 2, 3, \dots, n \quad (3.4)$$

for any joint angle configuration. Substituting equations 3.2 and 3.4 into equation 3.3 will result in:

$$\tau_i < \tau_{i-1}, i = 2, 3, \dots, n. \quad (3.5)$$

Substituting equation 3.5 into equation 3.1 means:  $\tau_A \leq n\tau_1$ . Substituting  $\tau_1 = \alpha_1 I_1$  and  $\alpha_1 = \frac{\alpha_{EE}}{n}$  in the equation results in:

$$\tau_A \leq \alpha_{EE} I_1. \quad (3.6)$$

The end effector angular acceleration  $\alpha_{EE}$  is at its maximum at the required acceleration value  $\alpha_{max} = 828 rad/s^2$ . The moment of inertia at  $I_1$  is at its maximum  $I_{max}$  when the manipulator is at the fully extended length  $L$  and the joint angles  $\theta_i = 0, i = 1, 2, \dots, n$ . In order to get an estimate on  $I_{max}$ , the manipulator is assumed to be a thin rod with uniform mass distribution. This results in  $I_{max} = mL^2/3$  with  $m$  being the mass of the manipulator. In this case the maximum required torque is less than or equal to:

$$\tau_{max} = \frac{mL^2\alpha_{max}}{3}. \quad (3.7)$$

We assume the manipulator has a length  $L = 15cm$ , which is double the average length of a human middle finger, and a cross section of  $4cm^2$ . This cross sectional area provides enough space in the links to achieve joint coupling. Assuming the manipulator is a solid cuboid piece of ABS plastic, which is a common thermoplastic used by 3D printers and has a density of around  $1g/cm^3$ , the mass of the rod is estimated to be around  $60g$ . Thus, the required torque at this manipulator mass and length is at most  $\tau_{max} = 0.373Nm$ . This required torque is considerably less than the torque of  $1.71Nm$  provided by the BLDC motor and harmonic drive pair. Therefore, the approach of Namiki *et al.* in [22] can achieve the required velocity and acceleration values with BLDC motors paired with harmonic drives.

Note, in equation 3.6,  $\tau_A = \alpha_{EE}I_1$  only holds when  $n = 1$  or the manipulator has only one joint. However, for the IFLS motion to resemble human-like hand opening and closing, at least two joints are required. This means that the torque needed  $\tau_A$  is smaller than  $\tau_{max} = 0.373Nm$ . Also, gravity was not considered in these estimate because the angular acceleration due to gravity is significantly smaller than the required angular acceleration.

In practice, energy loss due to friction, non-uniform mass distribution due to the coupling mechanism and joint location, and higher required lengths due to the architectural design criteria, can all increase the required torque from the actuation mechanism. However, there are multiple design modifications that can reduce the required amount of torque or increase the amount of available torque, without compromising the requirements. The required torque can be decreased by increasing the number of coupled joints or reducing the mass by for example changing the material. Also, Namiki *et al.* were highly constrained on the size of their actuation mechanism as they required individual joint actuation, requiring them to place the actuation mechanism in the links. However, in the design of the IFLS, since the joint motions are coupled, the actuation mechanism is only needed at joint  $J_1$ . This means that while the size of the actuation mechanism is still confined by architectural design constraints, the mechanical constraint on it is more lenient. A larger size for the actuator corresponds to higher achievable torques if necessary, or cheaper alternative designs. Considering the size of the skeleton of the IFLS to be  $15cm \times 2cm \times 2cm$ , about twice the average size of the human hand, an actuator is considered large when it is larger than this skeleton size and thus cannot be contained inside it.

High prices and low availability are the major issues with harmonic drives and BLDC motors. Second-hand harmonic drives are priced above 150USD online. With the additional price of around 30USD for BLDC motors [23], this solution costs at least 200USD.

Solutions consisting of BLDC motors coupled with conventional gearboxes are priced at around 70USD at RobotShop.com [24]. Costly and scarce options for BLDC motor design make brushed motors paired with conventional gearboxes that meet the required torque and angular velocity values more viable. This actuation pair will reduce efficiency, durability, and most importantly complicates high gain control due to backlash and noisier torque outputs. For example, the readily available geared DC motor solution provided by Pololu online robotic and electronic shop [25] can achieve an angular velocity of  $36.7\text{rad/s}$ , can output  $0.777\text{Nm}$  of torque, and costs about 25USD. These values are within the requirements on the IFLS. However, because of friction, gear backlash and freeplay, and non-smooth output torque, designing a controller that consistently achieves the maximum required torques and velocities in a smooth and natural-looking manner will be a cumbersome task, when complex motion trajectories, such as the affective motion trajectories, need to be tracked.

DC motor designs do not possess inherent compliance. Works such as [26] achieve active compliance during grasp actions performed by a robotic hand. However, while active compliance is beneficial for grasping tasks, for the purposes of this work, where frequent physical human interaction is a strong possibility, passive compliance is highly desirable. When the actuator driving mechanism is off or the controller is not active, something that can happen in an installation very frequently, these designs lose their compliance. They also add the need for an accurate and high-speed force or torque sensor for feedback, making their implementation very costly. Some levels of passive compliance can be achieved in a DC motor-based design by adding elastic and flexible elements to the structure of the system. The links of the manipulator can exhibit some levels of flexibility instead of being rigid, the joints can have elasticity such as the design in [27] for the joints of the iCub robot, or the structure can be covered with flexible material. These solutions complicate the design and implementation of the structure of the mechanism. They also reduce the precision of the trajectory-following controller.

In conclusion, a DC motor-based design can meet the majority of the design requirements of the IFLS mechanism. Inexpensive and easily available DC motor solutions exist that have the potential of meeting the required velocity and acceleration values. However, nonlinear responses in cheaper DC motor solutions can lead to unnatural and non-smooth motions. Also, compliance is difficult to achieve. The solutions for achieving compliance complicate the design of the trajectory-following controller and increase the production time and effort.

## Pneumatic Actuators

According to [28], the three main categories of pneumatic actuators used in robotics are: pneumatic cylinders [29, 30, 31], pneumatic artificial muscles (PAMs) [32, 33, 34, 35], and pneumatic motors [36], which are depicted in figure 3.2.

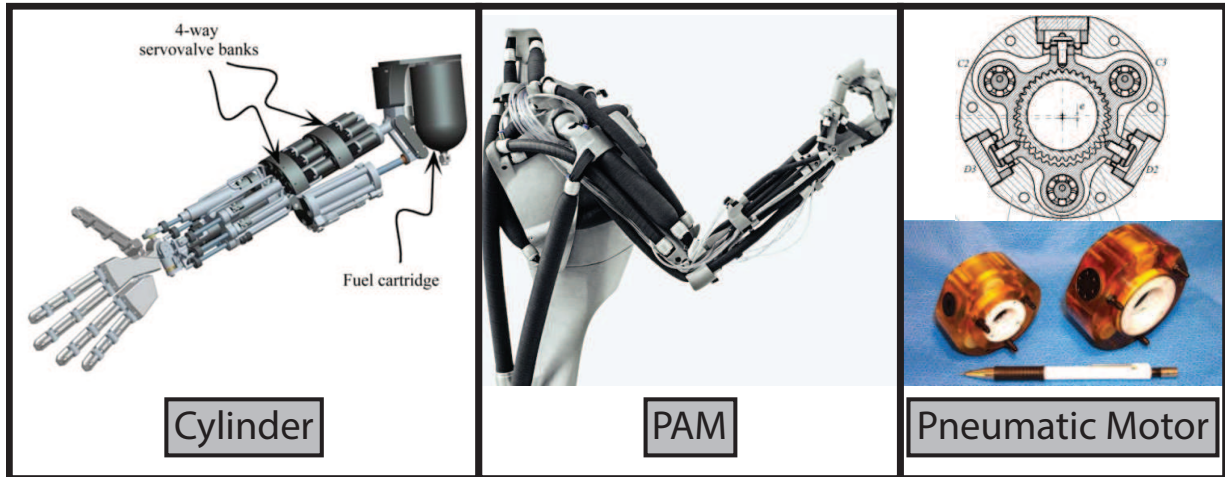


**Figure 3.2:** Illustration of the three main pneumatic actuators in robotics: pneumatic cylinder [30], pneumatic artificial muscle (PAM) [32], and pneumatic motors [37]

Pneumatic actuators transform the stored potential energy in pressurized gas into mechanical energy. These actuators are mainly known for their high power to weight ratio and their non-linear behaviour due to factors such as air compressibility [28, 38, 15, 21, 14]. With different levels of difficulty, these actuators can be custom designed and produced using 3D printing [37], machining [31], or simple do it yourself (DIY) techniques [34, 35].

Pneumatic motors provide rotational mechanical energy. They produce high torque rotational motion and therefore unlike DC motors they do not require torque increase mechanisms. Off-the-shelf pneumatic motors are expensive and scarce [39] and while they can be designed and 3D printed [37], the design process is time consuming. They also do not provide the high compliance that the other two pneumatic actuators provide. Therefore, if actuators with rotational motion and no inherent compliance are to be used, DC motors with torque increase transmission are a better candidate than pneumatic motors.

Pneumatic cylinders and PAMs both create linear motion. Pneumatic cylinders create the linear displacement by using air pressure to move a piston inside cylindrical shell. In PAMs, linear displacement is provided by restricting the 3D expansion of a pressurized

elastic core into a 1-dimensional linear motion. The operation of PAMs will be further discussed later in the section. Pneumatic cylinders are capable of providing bi-directional linear forces. These actuators also behave more linearly than PAMs. Their volume change has a linear relation with the displacement of the piston. This is unlike PAMs where the volume change has a highly non-linear relationship with the displacement of the actuator. However, due to their relatively simple design, PAMs are simple to customize and construct. Also, because of their lighter weight, these actuators provide higher power to weight ratios than pneumatic cylinders. Because of the elasticity of their core, they provide additional compliance on top of the compliance provided by the compressibility of air. Thus, due to their simple production methods, high customizability, and the fact that they provide more compliance, PAMs will be considered over pneumatic cylinders as a candidate for a pneumatic actuation solution.

Because of their simple design, there is a large variety of PAM actuator designs [40]. One of the first and still common PAM designs is the McKibben actuator [41]. The McKibben actuator consists of two main parts, the elastic hollow core and the braided sleeve that covers the core. When the elastic core is pressurized and starts to expand inside the braided sleeve, it forces the sleeve to elongate or shorten along a straight line [42] depending on the weaving design of the sleeve. The output force and displacement of the PAMs are controlled by controlling the internal pressure of the elastic core. PWM signals can be used to drive fast switching valves, such as the MHE2 series valves by Festo, in order to control the internal pressure of the PAM's membrane [43, 44, 45]. The output pressure of the fast switching valve, with respect to the duty cycle of the PWM input signal, is not linear. This adds to the difficulty of controlling these already highly nonlinear actuators. However, the PWM signalling of fast switching valves provides high bandwidth control over pressure and the ability to use digital microcontrollers for their control. Fast switching valves are relatively cheap as well, with the MHE2 series by Festo being around 100USD. The control of these actuators also requires a pressure source such as an air compressor. PAMs can be produced using simple DIY techniques which for example use cheap silicone hose as the elastic core and cable management braided sleeves. This makes PAMs highly customizable as well, with the possibility of different lengths, diameters and even colours for architectural purposes. In terms of durability and maintenance, the elastic core can wear out and the sleeves can start to tear. However, because the production process is simple and the costs are low, this is not a major issue.

While the displacement response of the PAM is not linear, its motion is smooth. This is mainly due to the damping effects of the compressed air and the elastic membrane. This means that with the appropriate transmission mechanism, this smooth motion can be transferred to the joints of the IFLS, resulting in smooth and natural motion for the

mechanism. As mentioned, PAMs provide inherent compliance as well. Thus, in terms of requirements on the visual and physical interaction with human observers, PAMs can perform well.

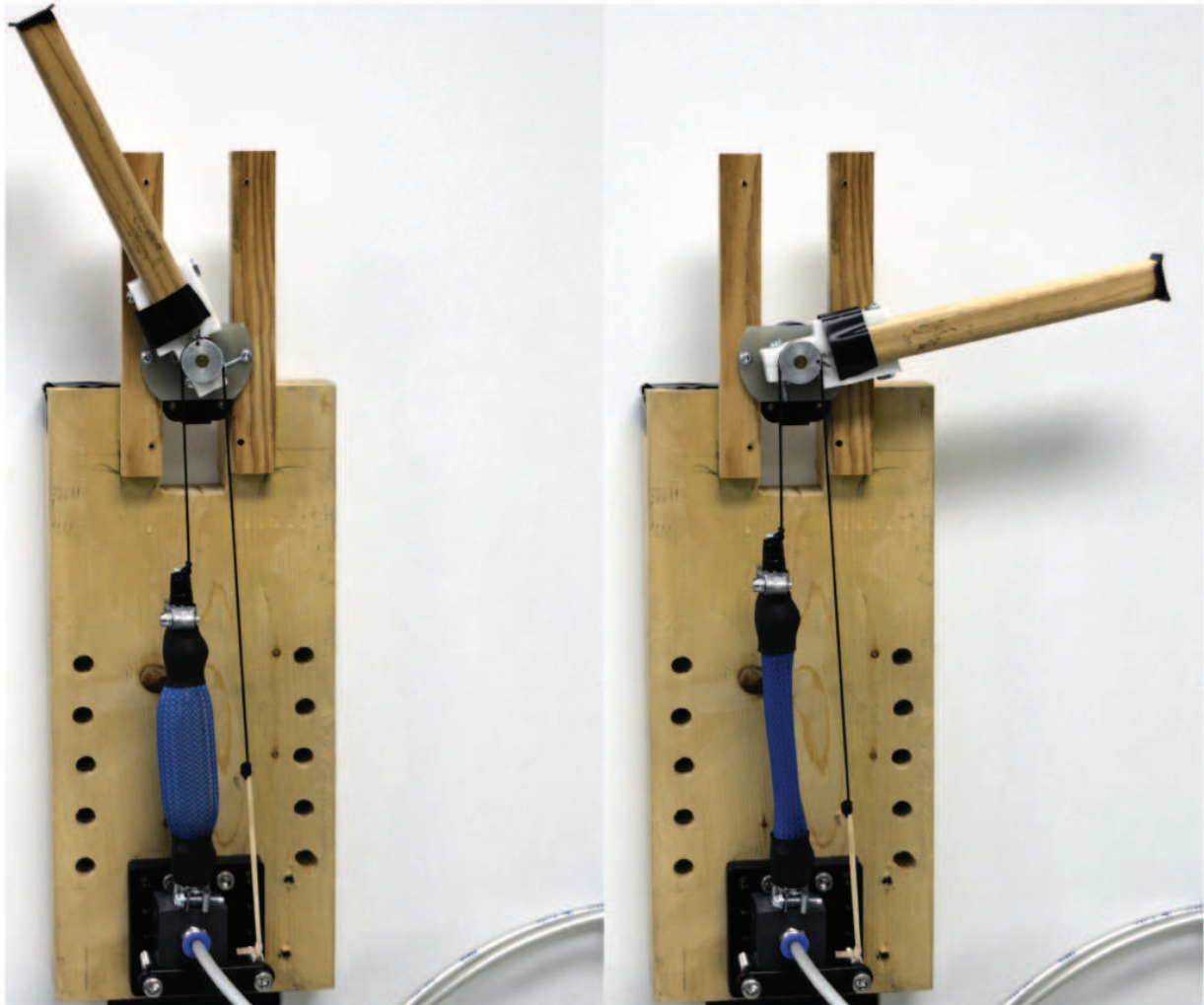


**Figure 3.3:** PAM dynamic response test apparatus. PAM pressurized to 450kPa shown on left and atmospheric pressure PAM shown on right.

In order to investigate the dynamic capabilities of PAMs, an experimental approach was taken. The test apparatus shown in figure 3.3 was designed to allow for the testing of different sizes of PAMs. The PAMs in the apparatus actuated a 1-DOF IFLS mechanism.

As discussed in the analysis of the DC Motors, 1-DOF IFLS require the most amount of torque or, in the case of PAMs, force. The link was a solid piece of wood with the size  $15\text{cm} \times 2\text{cm} \times 2\text{cm}$ , the same as the sample size used in the analysis of DC motors. The revolute joint was a low friction ball bearing and the force of the PAM was transferred to it by a short tendon and a pulley with a radius of  $1\text{cm}$ . Since PAMs only provide pulling forces, the pulley on the joint was also coupled with an elastic in order to achieve bidirectional movement. The end effector orientation was determined by integrating the angular velocity of the end effector, measured using an ITG 3200 digital gyroscopic sensor by InvenSense. Sample PAMs were produced at various lengths and diameters, using silicon hose and cable management braided sleeves. The open-loop pressure response of these sample PAMs was studied by inputting different pressure steps to the PAM and measuring the orientation at the end effector of the mechanism. Figure 3.4 illustrates the orientation plot of the end effector of the mechanism in response to a pressure step with an amplitude of  $450\text{kPa}$ . The sample PAM in this test had a sleeve diameter of  $2\text{cm}$ , membrane diameter of  $1\text{cm}$  and a length of  $10\text{cm}$ . Figures 3.5 and 3.6 show the angular velocity and acceleration of the end effector. The maximum velocity reached was  $35.6374\text{rad/s}$  and the maximum acceleration reached was  $1293\text{rad/s}^2$ . These figures are well above the required velocity and acceleration values required for the IFLS. Note that various passive actuation techniques or a secondary PAM for bidirectional active control of the joint can be used to achieve these dynamic response values for both directions of motion. Note, the vibrations observed in the velocity and acceleration plots are due to the fact that the gyroscopic sensor is attached to the tip of the structure using Velcro. High accelerations and sudden change of direction of motion causes the sensor to experience these vibrations and these are not actual tip vibrations. The magnitudes of the vibrations are small and cannot not be observed in the orientation plot.

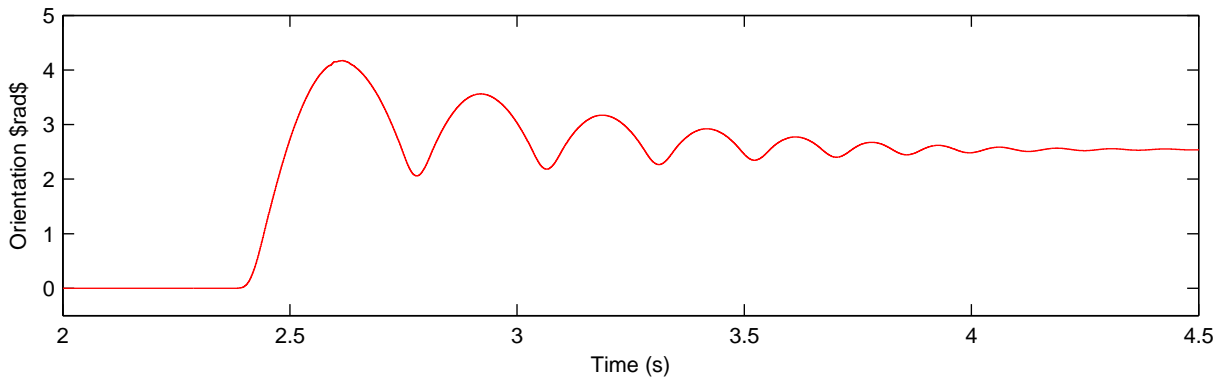


**Figure 3.4:** End effector orientation of PAM-actuated 1 DOF apparatus

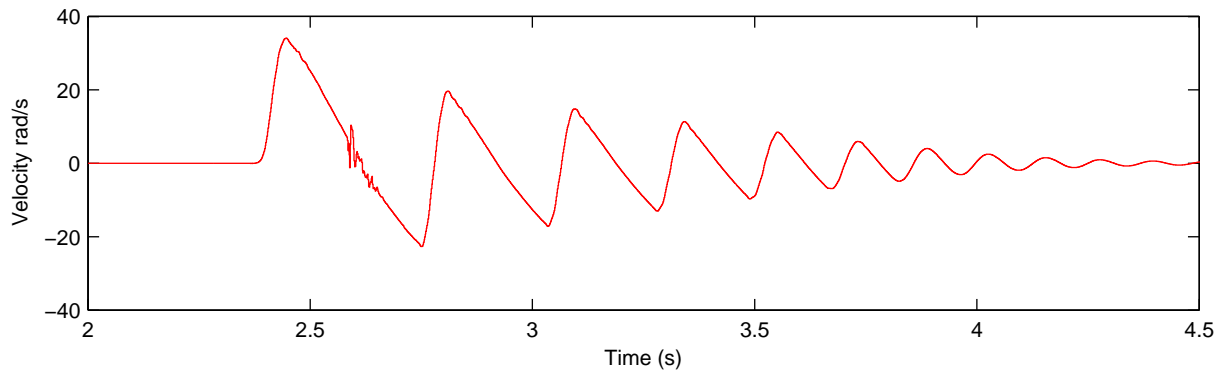


**Figure 3.5:** End effector angular velocity of PAM-actuated 1 DOF apparatus

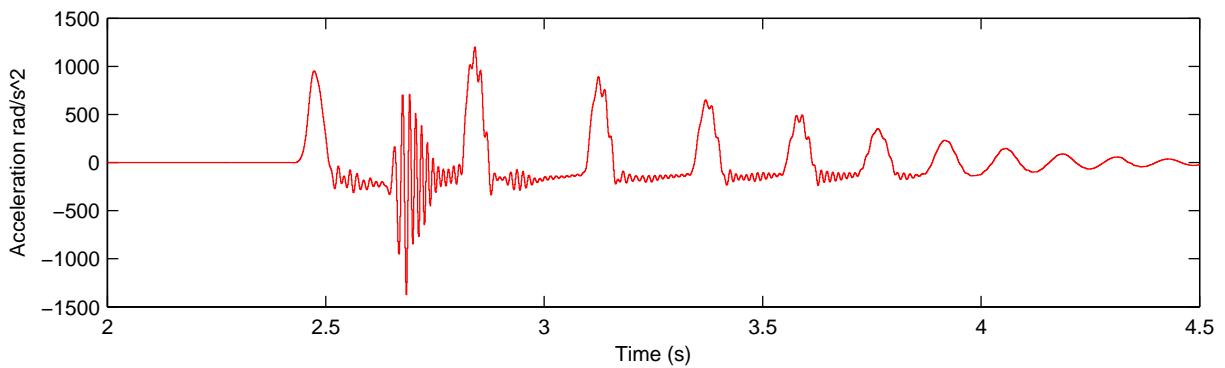


**Figure 3.6:** End effector angular acceleration of PAM-actuated 1 DOF apparatus

In summary, PAMs are a promising actuator solution for the IFLS. Their production is simple, they are very customizable and relatively easy to maintain. Their greatest advantage with respect to the applications of this work is their inherent compliance and smooth and natural looking motion. They also achieve the dynamic response requirements of the IFLS. One disadvantage of these actuators is their non-linear response which can make trajectory-following control difficult. In addition, the cost of the valve for driving these actuators is relatively high. However, cheaper pressure control techniques can be investigated to replace fast switching valves.

## Hydraulic Actuators

Hydraulic actuators are the other branch of fluidic actuators. They have many similar characteristics to pneumatic actuators, such as high power to weight ratio. The main advantage of hydraulic actuators over pneumatic actuators is their capability of providing high force ranges that in applications such as grasping can be very critical [46]. Also dexterous tasks such as calligraphy are performed by hydraulic actuated hands [47]. Liquid fluids used in hydraulic actuators are far less compressible than gas fluids used in pneumatic actuators. This reduces the non-linearity of these fluidic actuators in comparison to pneumatic actuators but also reduces their compliance. In addition, the maintenance of hydraulic actuators is more difficult and they are usually more expensive. Therefore, because high force ranges are not required in this application, and hydraulic actuators are less compliant, more expensive and harder to maintain, pneumatic actuators are the better fluidic actuator option for this work.

## Shape Memory Alloys (SMA)

SMAs are the actuators that are used in the tentacle mechanism of the Hylozoic Soil shown in figure 1.1. These actuators have also been used in robotic hands [48, 49]. In the operation of SMAs, thermal energy is used to reorient the crystal structure of metal atoms, resulting in a change in material modulus. Electromechanical actuators can be designed to capitalize on this modulus shift, resulting in a linear displacement at high force when the SMA is heated, often using electrical current. Due to their dependence on temperature change, which is a slow process, SMAs cannot achieve high bandwidth dynamic responses. These actuators also have nonlinear response with large hysteresis [50] which complicates their control. SMAs can meet the interactive architecture and human interaction requirements at a satisfactory level, mainly based on the fact that these actuators have been used in various interactive architecture installations before. However, due to their slow dynamic response and difficulty of control they cannot be considered for affective motion applications.

### 3.1.2 Transmission

The transmission mechanism in conventional robotic mechanism designs transfers the energy of the actuator to the joints of the mechanism. There are various transmission mechanisms that are used in robotic hand designs [14, 15]. The motion of the IFLS is coupled, meaning that the energy of the actuator located on the first joint has to be transferred to all the joints of the mechanism. Not every transmission mechanism has the capability of

providing coupling. As illustrated in figure 3.7, four possible remote transmission mechanisms that can provide coupling are: Belt and Pulley [51, 52, 53], Gear Series [54, 51], Linkage [55, 56, 57], and Tendon and Sheath [58, 59, 60]. Gear series suffer from backlash, high friction, high weight and design production complications and thus are not considered. Tendon and sheath are also not considered due to high friction and loosening of the tendons that can introduce non-linearities and cause unnatural motion. This leaves Belt and pulley, and linkage designs as the only remaining options. Linkage designs can have a simpler production process and higher customizability by the use of 3D printers. However, linkage designs also require a considerably longer design period. Both methods lose energy due to friction. In addition, in belt and pulley designs, slipping can occur especially when the belt starts to loosen up over time and lose grip. This means the maintenance and durability of belts and pulley designs are also worse. Thus, between the two mechanisms, each one has advantages and disadvantages. Depending the availability of a 3D printer, available design period, and concerns on durability each solution can be viable.

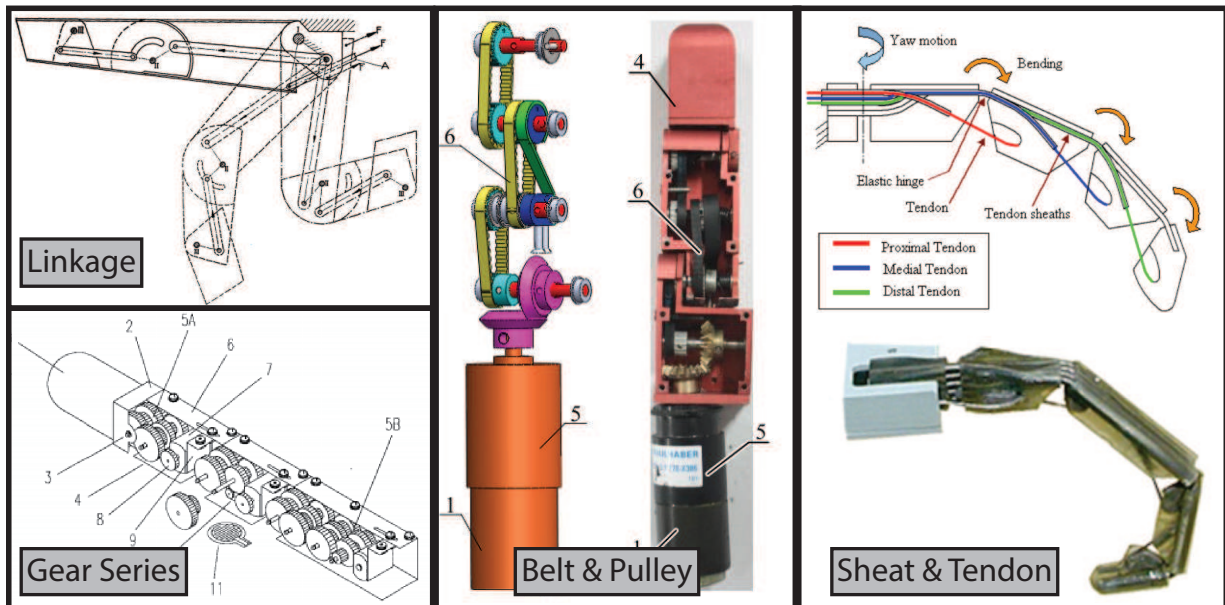


**Figure 3.7:** Illustrations of linkage [57], gear series [51], belt and pulley [53], and sheath and tendon [58] transmission mechanisms

## 3.2 Soft Pneumatic Artificial Muscles

### 3.2.1 Background

In recent years there has been a significant interest in a type of pneumatic actuator called soft pneumatic artificial muscle (SPAM). These actuators evolved from older pneumatic artificial muscle (PAM) designs such as the McKibben pneumatic muscles [61]. Conventionally, PAM designs [62] provide linear motion trajectories with high power to weight ratios, inherent stability, high motion speed, and inherent compliance. Unlike PAMs, SPAMs do not contain rigid links or transmission mechanisms, the body of the muscle chamber is used as the end-effector. SPAMs extend the benefits of PAM actuators by providing the potential for non-linear motion trajectories, such as curl or twist motions. These benefits make SPAMs suitable for a variety of applications, such as exoskeletons and rehabilitation assistance, shown in figure 3.8, images 1 and 2 [63, 64]; handling and grasping objects with complex geometry, or delicate objects such as food, shown in figure 3.8, images 3 to 6 [65, 66, 67, 68, 69]; and multi-DOF, multi-actuator, robotics mechanisms capable of performing sophisticated motions such as gait or swimming shown in figure 3.8, image 7 [70, 71].

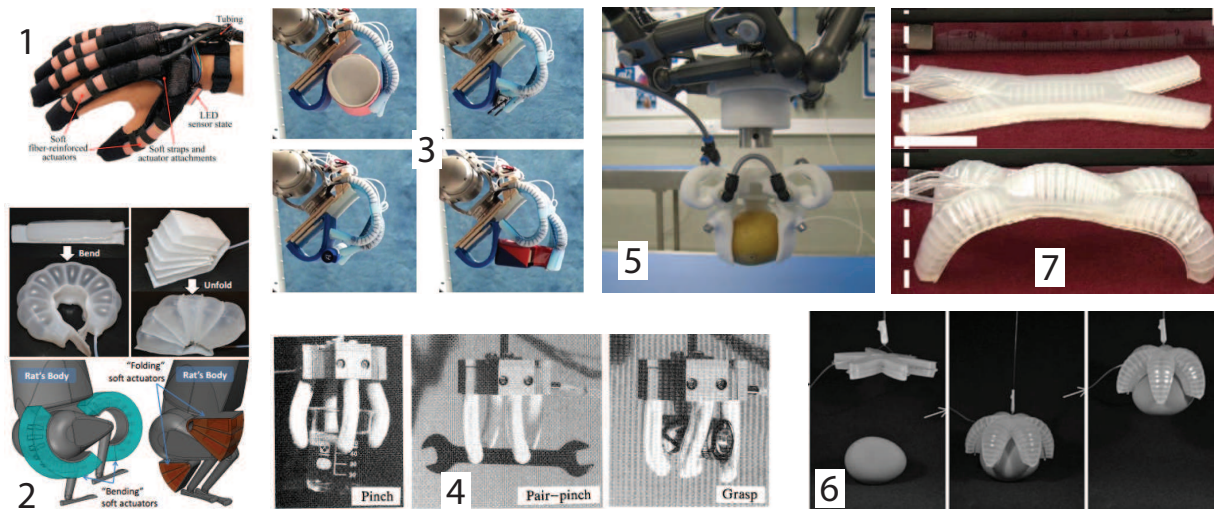


**Figure 3.8:** 1: Soft Fiber-reinforced Actuators [64] 2: Soft Pneumatic Actuators (SPA) [63] 3: PneuFlex [69] 4: Flexible Microactuator (FMA) [68] 5: Concentric Additive Manufacturing Actuators [66] 6: PneuNet [67] 7: Multigait Soft Robot [70]

The earliest designs for SPAMs were presented as flexible microactuators (FMA) by

Suzumori *et al.* in [72]. In the design of the FMA, 3 separate chambers are present in a rubber tube. Pressurizing one or two of the chambers while leaving the rest unpressurised or at lower pressures will cause the rubber tube to exhibit a bending motion. This is because of the difference in the elasticity between the outer surface of the pressurized chambers and the inner core of the rubber tube, with the outer surface being more elastic. Therefore, under pressure, the outer surface extends more than the inner core of the tube, causing the structure to bend. Fibers are also included in the outer surface of the rubber tube to prevent overstretching the outer surface and *bloating*. Bloating occurs when the elastic material of the SPAM stretches out from the unpressurized shape of the SPAM similar to a balloon (see, e.g., image 2 in figure 3.8). For the interactive architecture application considered in this work, bloating is highly undesirable. As Samadani *et al.* [9] suggest, the appearance of the mechanism performing the motion also influences the emotion conveyance capabilities of the mechanism. Bloating noticeably changes the appearance of the SPAM, which will make the appearance a factor for affective analysis and may inhibit the communication of affect. Furthermore, bloating can degrade the ability of the silicon to fully retract to its original shape, thus reducing durability.

Since the introduction of the FMA, many SPAM designs have been presented that utilize a similar method for implementing bending motions. In PneuNets [67], the hollow elastic core of the actuator is partially molded over with a lower-elasticity material, generating bending motion when pressurized due to the difference in the elasticity of the two materials. In designs such as PneuFlex [69] or soft pneumatic actuator (SPA) [73], the hollow elastic core of the actuator is partially covered with a much thinner and lighter material such as a silk mesh that is non-elastic but flexible. This design provides a larger difference between the elasticities of the vertical surfaces which results in more bending deformation. In [69], fiber threading around the hollow core is also introduced. While the introduction of the fiber threads might reduce the amount of bending, similar to the fiber in the FMA, it prevents bloating behaviours that are present in [67, 73], which can be undesirable for many applications.

There are several SPAM designs that produce finger-like motion [69, 71, 73]. SPAM designs similar to the PneuFlex [69] are the most suitable design for this work. PneuFlex is an actuator designed for grasping applications. Its rest pose and its motion trajectory both resemble that of the human finger. In comparison to other finger-like SPAMs, PneuFlex maintains its finger-like appearance during its motion, avoiding the distension often observed in SPAM designs (e.g., SPA in figure 3.8, image 2). PneuFlex SPAMs are also simpler to construct than the SPAM design from [71] for example, which requires more complex elastic hollow core and bend-causing mechanism designs.

### 3.2.2 SPAM Requirement Analysis

In this section, the SPAM actuator is analysed with respect to the three requirements categories discussed in section 2.2. The requirement analysis of SPAM actuators demands a slightly different approach than the previous actuation candidates for the IFLS. Because these actuators are recent and are mainly still in the research state, there are no off-the-shelf SPAMs available nor are there any well established manufacturing processes for producing them. A variety of do-it-yourself (DIY) approaches currently exist [69, 71, 73] which all exploit the new advances in 3D printing and silicone rubber technologies. In the case of the PneuFlex, for example, 3D printed molds are used to mold elastic silicone compounds into the desired hollow cuboid shape. Silk mesh and fabric threading are then used to restrict the motion of the SPAM to the desired trajectory. Driving mechanisms for SPAMs remain an area of research. Currently, various solutions exist each with their own advantages and disadvantages. This means that the design of SPAM actuators, their manufacturing process, and their driving mechanism are still active research topics with potential for significant contributions. Current SPAM designs can be modified to rectify known issues and make their design more suitable for specific applications such as the IFLS. These opportunities add an attractive dimension to SPAMs that the other actuation solutions for the IFLS do not possess. However, the early stage of the SPAM technology also makes analyzing the IFLS requirements more difficult. Since the PneuFlex actuators are the most suitable SPAM design for the IFLS, the design and the manufacturing process of these actuators is analysed for the IFLS requirements. The driving mechanism for SPAMs is also an important factor in analyzing how well these actuators meet the IFLS requirements. Conventional pneumatic driving mechanisms used for actuators such as PAMs and pneumatic cylinders are considered for the analysis of SPAMs.

PneuFlex actuators were designed for grasping applications and no data was available on their performance during fast dynamic motion. Therefore, a pneumatic driving mechanism was constructed in order to collect the open-loop step response of the PneuFlex actuator. Similar to the apparatus designed for conventional PAMs, the orientation change of the PneuFlex's tip during the open-loop response is determined by integrating the tip angular velocity, measured using the ITG 3200 gyroscopic sensor by InvenSense. The sensor communicates with a Teensy 3.1 Microcontroller over the I<sup>2</sup>C digital interface.

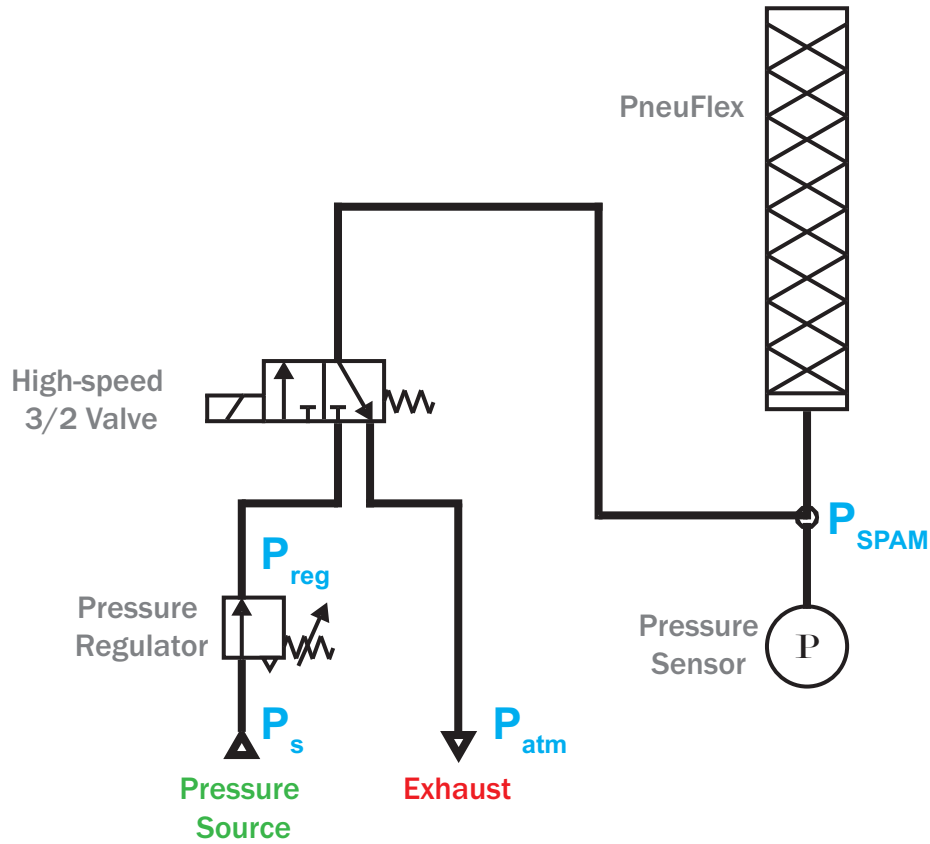


**Figure 3.9:** Pneumatic open-loop circuit

Figure 3.9 illustrates the pneumatic circuit that was designed and implemented to drive the PneuFlex actuator. The pressure  $P_s$  is provided to the circuit using the P15 TC compressor by Werther Internationals. This pressure needs to be regulated in order to prevent pressure drop when there is air flow in the circuit. The pressure from the compressor is regulated by the NAW2000-N02-2 regulator from SMC. The regulated pressure  $P_{reg}$  is fed to a 3/2 high-speed valve. Using a 3/2 valve enables the circuit to be pressurized to  $P_{reg}$  and depressurized to atmospheric pressure  $P_{atm}$  by a single valve. Festo’s MHE2-MS1H-3/2G-M7-K, capable of switching at 330 Hz, is used as the high-speed 3/2 valve. This valve is considerably more expensive than conventional slower switching valves. However, using pulse width modulation (PWM) signaling, high-speed valves can provide electronic control over their output pressure [43, 44, 45]. As discussed in detail in chapter 4, this feature will be essential in controlling the internal pressure of SPAMs and in turn, controlling the tip orientation. A pressure sensor (MPX5500DP by Freescale) is placed at the pressure intake

of the SPAM to measure its internal pressure. Pressure sensor analog measurements are read by a 12-bit ADC on the Teensy 3.1 microcontroller.

In order to improve the dynamic response of the PneuFlex SPAM, its air pressure intake had to be modified. The air pressure intake of the original PneuFlex is located on the side of the actuator and the intake tube is considerably narrower than the internal hollow core of the SPAM and the tubing of the pneumatic circuit. The narrow air intake affects the pressure response of the SPAM by reducing the mass flow rate and dampens its motion due to the resulting low pass filtering effects. As illustrated in figure 4.1, by bringing the intake of the SPAM to the bottom of the actuator it became possible to increase the intake tube size to 1/4" I.D., which is the tubing size of the pneumatic circuit and is much closer to the width of the SPAM hollow core.

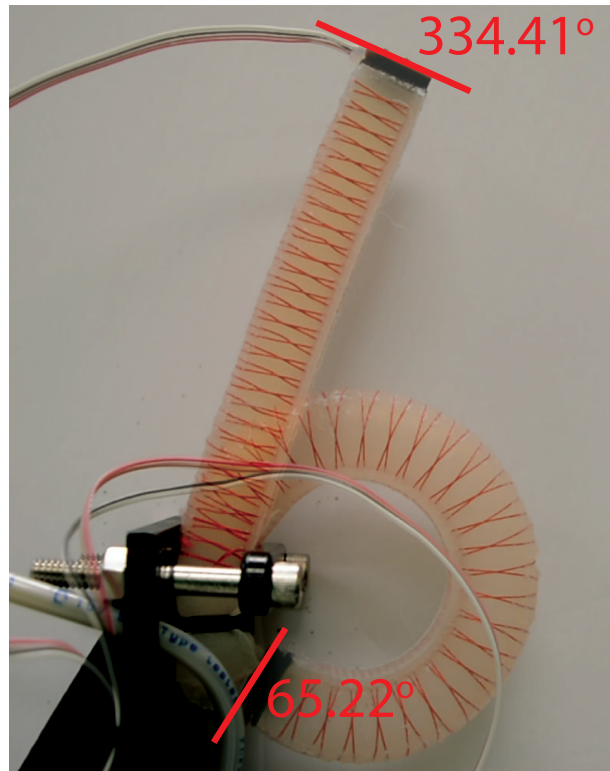


**Figure 3.10:** Absolute end effector orientation of the PneuFlex measured on still images

Using this pneumatic circuit and the new PneuFlex configuration, a test is performed on the ITG 3200 gyroscopic sensor to see if the sensor is capable of capturing all the

frequencies of motion of the tip of the PneuFlex. First, the sampling rate of the sensor is set to the maximum rate of 800 Hz. Second, a step pressure change which results in the PneuFlex travelling its full range of motion is applied to the actuator. Side-view images are taken of the PneuFlex at the rest pose and at the fully contracted pose. Third, the angular displacement of the tip orientation is measured using Adobe Illustrator from the two pose images as shown in figure 3.10. Fourth, the angular displacement of the tip is calculated by integrating the angular velocity measured by the sensor during the step response. Lastly, the two achieved angular displacements are compared to evaluate the validity of the gyro-measured data. The angular displacement from the images, as depicted in figure 3.10, is  $334.41^\circ - 65.22^\circ = 269.19^\circ = 4.6983$  rads. The angular displacement measured using the gyroscopic sensor is 4.6962 rads. This means that the discrepancy between the two methods is 0.0021 rads, which is small and suggests that the gyroscopic sensor is capable of measuring the angular displacement of the SPAM. Since the Teensy 3.1 microcontroller was fully capable of handling the data from the sensor at 800 Hz, no lower sampling rates were tested. The measured angular velocity was also translated to angular displacement online, in the Teensy 3.1 microcontroller. The pressure and angular displacement data was transferred in real-time from the Teensy 3.1 microcontroller to MATLAB Simulink on a Windows machine over USB.

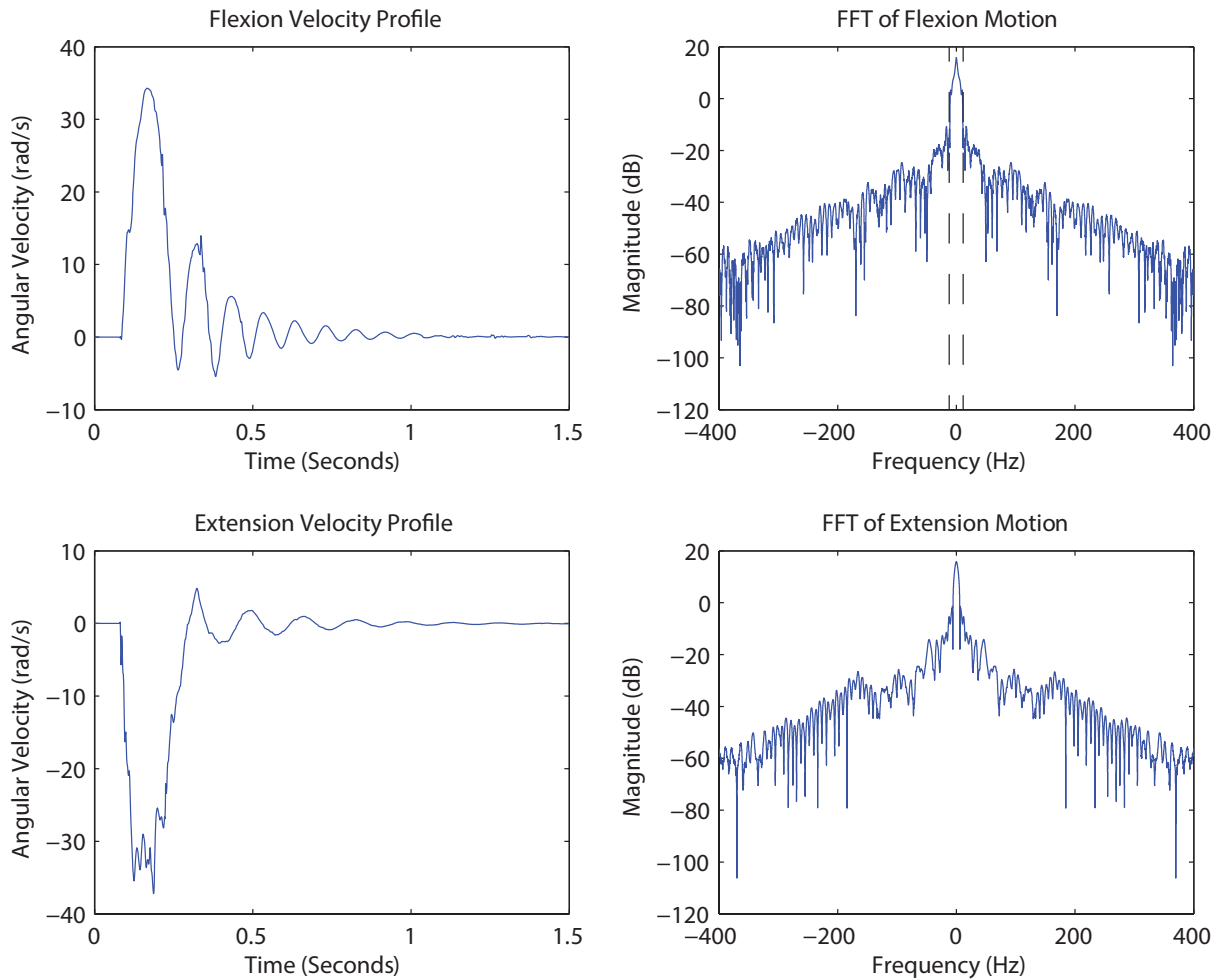


**Figure 3.11:** Frequency content of the velocity of SPAM’s full flexion and extension step response

The Fourier transform of the step response of the SPAM is also investigated in order to determine the magnitude of frequencies of motion of the SPAM actuator. Figure 3.11 shows the frequency content of the velocity signals during the flexion and extension of the SPAM. The fast Fourier transforms of the two motions show that there is a significant drop in frequencies above approximately 10 Hz marked by the dashed vertical lines in the figure. In fact, using the 400 Hz range of measured frequencies, 99.7% of the power of the flexion motion is in frequencies under 11 Hz and 99.3% of the power of the extension motion is in frequencies under 11 Hz. The exponential decrease in the power of frequencies above 11 Hz and the fact that the calculated displacement was inline with the measured

displacement, means that it is highly unlikely that the SPAM has any frequency of motion above 400 Hz, which is the Nyquist frequency of the control system.

## Interactive Architecture Requirements

The interactive architecture requirements for the IFLS are explained in section 2.2.1 of the requirements chapter. In order to analyze SPAM in this category of requirements, the production method for the PneuFlex SPAM and the presented pneumatic driving mechanism are individually analysed in each subcategory.

**Ease of production:** Deimel and Brock describe the production of PneuFlex actuators in [69]. In their procedure, a mold is designed and 3D printed for a hollow cuboid core. The negative design of the 3D printed mold leaves marks on the edges of the core that simplify the threading of fiber around the elastic core. After threading the fiber around the core, the non-elastic flexible mesh is applied to one of the four vertical faces of the core. While the design of the 3D printed mold might be time consuming and require trial and error in order to achieve the most suitable dimensions, it only has to be done once and afterwards, more molds can be printed or the same mold can be used multiple times. The degassing and curing process of the silicone rubber for the elastic core requires a long time. However, since no human effort is required during the curing process, the curing time should not cause issues as long as proper time management measures are in place. Threading of fiber around the core can complicate the production of PneuFlex actuators if repeatable motion between the produced actuators is a significant concern. The pattern and the spacing of the fiber threads dictate the motion trajectory of the actuator. Even with the marks on the edges of the elastic core, precisely repeating the thread patterns might not be easily achievable. However, for IFLS repeatable motion is not a paramount concern as long as the actuator does perform a finger-like motion. Thus, not a lot of effort and time should be spent on the precise threading of these actuators.

The production of the pneumatic driving circuit is relatively simple. It mainly involves buying off-the-shelf components and connecting them together with minimal effort. The compressor and the regulator are already sold assembled together. The high-speed valve needs to be equipped with the correct size fitting for the 1/4" tubing. The pressure and the gyroscopic sensors, and the Teensy 3.1 microcontroller require some passive components. At the early stages of production, this requires manual soldering on prototyping boards. However, at higher production volumes, PCB boards can be designed to significantly reduce the soldering effort required.

The most cumbersome task in the production of the PneuFlex actuator and its driving

pneumatic circuit is the threading of fabric around its elastic core. In addition, constructing the electronic circuit for the sensor and the microcontrollers can also be time consuming if no PCBs are designed and ordered for the electronic circuit. The curing period for the silicone is long (i.e., at least a day), therefore, in order to ensure a properly built silicone core, with no air bubbles or other defects, extra care must be taken during the casting stages of the silicone.

**Cost of production:** The cost for the PneuFlex actuator is low, especially if high volumes are being made and silicone can be bought in high quantities. Experimentally, it was determined that 22.5g of silicone is required for each PneuFlex actuator. Thus, with 7.2kg of silicone available at 200USD [74], more than 300 PneuFlex actuators can be produced. This results in a per-unit price of less than 1USD. Thus, the most significant portion of the cost is associated with the sensing and the pneumatic driving components. The cost of a PneuFlex actuator that is equipped with both pressure and angular position sensors and is individually controllable, i.e., requires an individual high-speed valve, will be 30USD+70USD+20USD+100USD+10USD = 230USD. These are the costs of the pressure sensor, gyroscopic sensor, Teensy 3.1, Festo’s high-speed valve, and other costs such as tubing, fitting, and silicone respectively. However, not all of the PneuFlex actuators need to be fully equipped in an installation. One advantage of SPAM actuators is their inherent stability, thus, these actuators do not necessarily need closed-loop control to achieve trajectory-following. The control signal of a closed-loop trajectory-following SPAM can be captured and fed to the SPAM in open-loop to achieve similar motion trajectories without the use of pressure and gyroscopic sensor. Also, not every SPAM needs to be individually controlled. Thus, multiple SPAMs that perform similar motions can be driven by a single valve. The cost of the air compressor and electrical power supply are not considered in these cost estimates, as these components are usually available in engineering and architectural working environments. However, if large numbers of these actuators are installed, multiple power supplies and air compressors might be required which considerably increases costs. Thus the per actuator cost of an installation largely depends on the number of required actuators, how different their motion trajectories will be, and the importance of disturbance rejection and tracking error performance.

**Customizability:** As the background section on the SPAM actuators suggests, the design of SPAMs and their output motion is highly customizable. The output trajectory of the SPAM and its appearance during motion are determined by the design of the casting of the hollow silicone core and the design of the motion-restricting mechanism. With the help of 3D printers and other prototyping methods, virtually a limitless variety of silicone castings can be designed, allowing for various types of motion and static and dynamic poses. In addition, a number of motion restricting methods are available, each resulting in

a different type of motion and pose. Fiber threading, flexible non-elastic silk mesh, rubbers of various stiffnesses, and higher wall thickness are some of the better known methods for restricting the motion of the elastic hollow core.

**Components availability:** The components used in the manufacturing of the SPAM actuators and their driving mechanisms are all largely available and are provided by well-established vendors. For the production of the SPAM actuator, multiple sources can be used to purchase the fiber for threading and the non-elastic flexible mesh. The silicone rubber is the EcoFlex series of silicone purchased from Smooth-On which is a well-established company capable of providing the chemicals in bulk. In the pneumatic driving circuit, the Festo high-speed valve is the only component that is unique and requires the specific model and brand. The other components in the circuit such as the compressor, the regulator, or the tubing, can be purchased from any provider as long as the component meets the design specification of the circuit. The design specifications of the circuit are within the common range of pneumatic components and thus finding these components is straight forward. The main electronic components of the driving mechanism, the Teensy 3.1, the gyroscopic sensor, and the pressure sensor, can all be purchased from online vendors such as DigiKey and SparkFun in large quantities.

**Maintenance:** As a pneumatic electro-mechanical system, there are routine maintenance tasks. The silicone in the SPAM actuator can tear and cause leaks from its interaction with the motion restricting mechanisms. Usually, the tear can be fixed by applying silicone and sealing the leak. Various designs can increase the robustness of the SPAM and reduce the amount of maintenance required. In addition, the compressor needs regular oil changes and the water accumulated in its pressure chamber needs to be drained out regularly.

## Human Interaction Requirements

In subsection 2.2.2 the requirements on the interaction capabilities of the IFLS actuator with human observers are discussed. There are two main concerns with the interaction between the IFLS and the human observer. Visually, there should be no features in the poses the IFLS achieves or the motion it performs that interfere with the ability of the IFLS to convey the desired affective content. In case of SPAMs, there are multiple SPAM designs that achieve poses that are unnatural, especially due to defects such as bloating of the silicone core. However, there are motion-restricting mechanisms, such as the fabric threading method in PneuFlex SPAM, that prevent this bloating behaviour. Due to the dampening effects caused by the elasticity of the silicone core and the compressibility of the air, the motion of the SPAM is smooth and under-damped in open-loop. However, small-magnitude vibrations are present in the open-loop response of the SPAM and PWM

control method for achieving variable internal pressures can cause additional vibration in the motion. Therefore, the performance of the controller is also critical in keeping the motion of the SPAM smooth.

A strength of SPAM designs is their physical characteristics during physical interaction between the IFLS and the human observers. Due to their inherent compliance and lack of rigid links, SPAMs are very safe during contact and physical interaction with human observers. They can possibly encourage human interaction due to the soft and natural feeling of the silicone both during motion and at rest.

## Dynamic Requirements

In order to analyze the velocity and acceleration requirements discussed in subsection 2.2.3, step pressure changes were applied to the SPAM until the required velocities and accelerations were met by the SPAM. The angular velocity of the tip of the PneuFlex was measured from the gyroscopic sensor and its angular acceleration was calculated online in Simulink. The open-loop step response trials were initiated with a regulator pressure of  $P_{reg} = 150kPa$ .  $P_{reg}$  was increased in  $50kPa$  increments until the required angular velocities and accelerations were reached during the flexion and extension response of the SPAM. As the internal pressure response of the SPAM depicted at the bottom of figure 3.12 suggests, at a regulator pressure of 250kPa, maximum and minimum dynamic requirements were achieved.

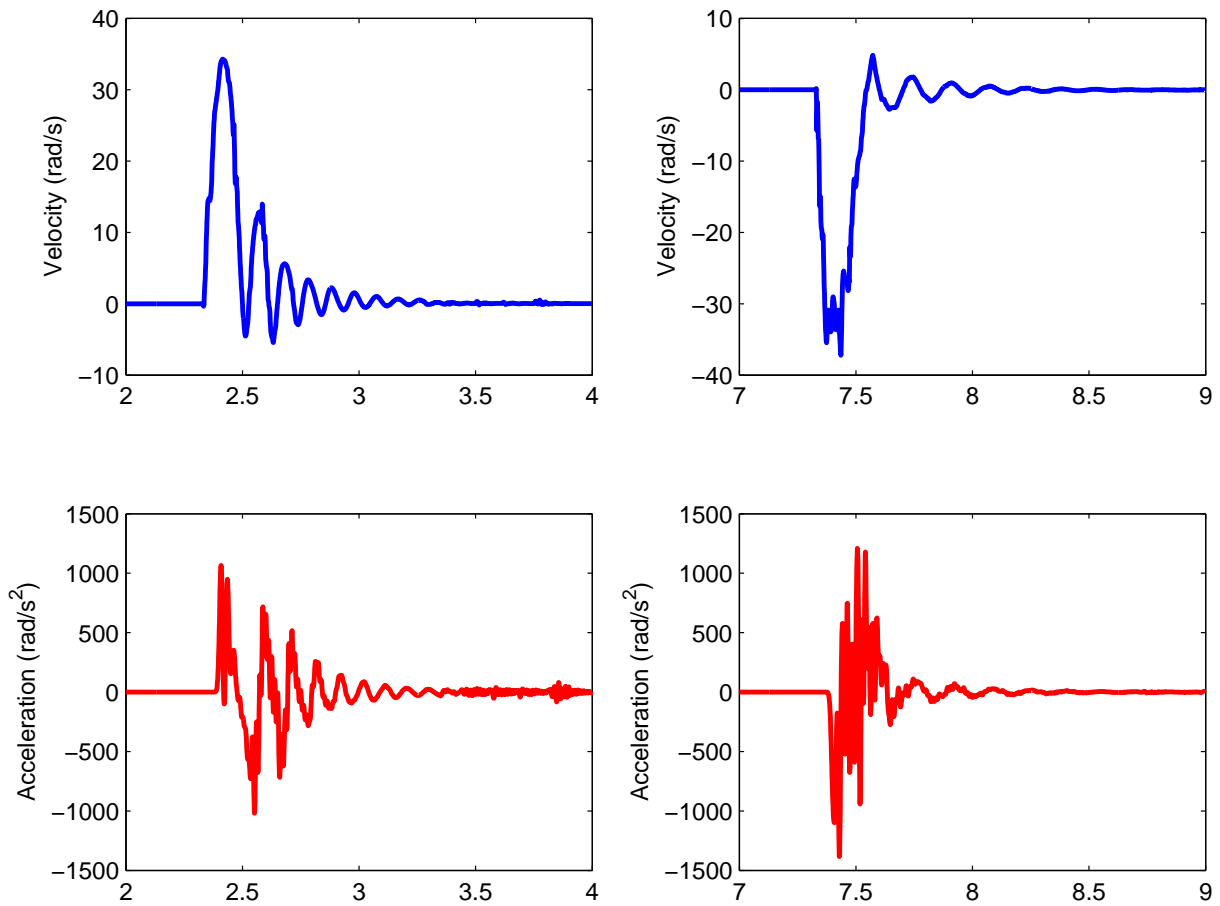


**Figure 3.12:** SPAM's full flexion and extension tip orientation response

Note the under-damped response of the internal pressure of the SPAM with respect to 250kPa step pressure at the valve. This under damped pressurization is due to the low pass filter behavior of the SPAM in the pneumatic circuit.

Table 3.1 presents the maximum and minimum achieved angular velocities and accelerations by the PneuFlex's end effector. It can be seen that in fact all the desired angular velocities and accelerations for the end effector of the IFLS presented in table 2.3 are achieved.

**Table 3.1:** End effector orientation, velocity, and acceleration of PneuFlex SPAM design

	<b>Max</b>	<b>Min</b>
<b>Orientation</b> ( <i>rad</i> )	4.696	0
<b>Velocity</b> ( <i>rad/s</i> )	34.84	-37.23
<b>Acceleration</b> ( <i>rad/s<sup>2</sup></i> )	1222	-1384
<b>Pressure</b> ( <i>kPa</i> )	251.2	102.7

### 3.3 Mechanical System Design Summary

In summary, because the SPAM actuator was capable of achieving the human interaction and fast dynamic requirements of the IFLS, it is chosen as the design for the IFLS mechanism. In some categories of interactive architecture requirements, SPAMs do not rate well. Depending on the design of the installation, deploying SPAMs can get costly. Their production can also get cumbersome and time consuming depending on the requirements for repeatability. However, they are very customizable and they do not require an external skeleton or a transmission mechanism. In addition to meeting the requirements in most categories, SPAM research is still in the early stages, with a significant potential for innovation and further discovery.

As the three most suitable actuation designs for the IFLS, the performance of the SPAM actuator, DC motors, and PAMs against the IFLS requirements is compared in table 3.2.

**Table 3.2:** Comparison of the three most suitable actuation options against the requirements for the IFLS mechanism

	DC Motor	PAM	SPAM
<b>Ease of Production</b>	Skeleton design and attachment of actuation to skeleton is difficult	Skeleton design and attachment of actuation to skeleton is difficult	With no skeleton requirements, the production effort is low
<b>Cost of Production</b>	Higher if BLDC designs are chosen but medium with brushed motors are used	Costly if control using high-speed valve is used for every individual actuator	Costly if control using high-speed valve is used for every individual actuator
<b>Customizability</b>	Not much customization is possible except through transmission mechanism and the skeleton	Variety in size and color is possible, however, full customization of the mechanism is hindered by the transfer mechanism and the skeleton	Highly customizable both in static pose and looks, and in the motion trajectory
<b>Components Availability</b>	DC motors and their required components are largely available through online vendors with multiple alternatives	Most components are available online with multiple alternatives. Only few options are available for High-speed valve	Most components are available online with multiple alternatives. Only few options are available for High-speed valve
<b>Maintenance</b>	Low maintenance as DC motors designs are robust	The compressor requires monitoring for oil levels, leaks are possible but easy to fix	The compressor requires monitoring for oil levels, leaks are possible but easy to fix
<b>Visual Interaction</b>	Achievable through expensive designs with minimal non-linearities	With simple low-friction transmission mechanism and skeleton, smooth and natural motion is possible	Natural and smooth motion is inherently available
<b>Physical Interaction</b>	Achievable with complex and costly designs without any passive compliance	While the actuator provides compliance, the rigid structure will limit the compliance	Highly compliant and "soft" even when not actuated
<b>Velocity (rad/s)</b>	Possible with either large size and heavy motors or high-cost small motors (up to 10x smaller in volume or weight)	The desired velocities were experimentally achieved	The desired velocities were experimentally achieved
<b>Acceleration (rad/s<sup>2</sup>)</b>	Possible with either large size and heavy motors or high-cost small motors (up to 10x smaller in volume or weight)	The desired velocities were experimentally achieved	The desired velocities were experimentally achieved

# Chapter 4

## SPAM Control<sup>1</sup>

In applications of SPAMs such as grasping [69], low speed gait [70], and rehabilitation assistance [63], open-loop feedforward controllers are used to control the SPAMs. These applications are mainly exploiting the compliance properties of SPAMs to conform to the body or grasped object and provide appropriate force, at relatively slow velocities and accelerations. To the best of the author’s knowledge, no work on SPAMs focuses on controlling the fast dynamic response of these actuators to generate high velocity and acceleration motions. In particular, no work to date achieves closed-loop control over the high speed response of these actuators.

Due to the similar design of SPAMs and conventional PAMs, closed-loop controller designs for conventional PAMs are investigated as a starting point for designing a closed-loop controller for SPAM actuators. Modeling PAMs is a difficult task because of the non-linear relationship between the change in the pressure of the elastic core and the change in the actuator’s geometry and volume [75]. The non-linear response of these actuators complicates their position or force control. Joupilla and Ellman [45] and Minh *et al.*[76] use linear PID pressure and position controllers in cascade mode and achieve acceptable position tracking results. In their design, the inner loop of the cascade controller uses pressure feedback to control the pressure at the intake of the actuator. The outer loop uses the reference position trajectory and position feedback to provide the reference trajectory of the inner loop pressure controller. The idea of cascade controller with feedback for both pressure and position is investigated in order to design a cascade PID controller for the SPAM actuator.

In section 3.2.2, an electromechanical system with pneumatic and electronic circuitry

---

<sup>1</sup>An early version of this chapter has been submitted to IROS 2015

was designed that enables the PneuFlex SPAM to achieve fast dynamic responses in open-loop. The system also provides feedback on both the tip orientation and the internal pressure of the SPAM. In order to achieve closed-loop control, the pneumatic circuit is modified to improve the noise levels of the variable pressure driving mechanism. A linear PID pressure and position controller in cascade mode, similar to controllers for conventional PAMs [45, 76], is designed and implemented in the system to control the position output of the SPAM.

In this chapter, first, an approach for controlling the PneuFlex actuators is proposed. The slight modifications to the design of the PneuFlex are explained, the electromechanical system for providing electronic control over the actuator is presented, and the closed-loop controller is discussed. Second, the proposed approach is implemented and verified experimentally.

## **4.1 Proposed Approach**

### **4.1.1 PneuFlex Actuator design modification**

During the early stages of experimentation, it was observed that the PneuFlex actuators show signs of damage at the points where the fabric threads meet the edges of the SPAM. This issue was amplified when the PneuFlex actuator was driven at higher velocities. Leaks started to occur after only a few high-speed trials and lots of effort and time had to be put in to fix the leaks. In order to improve durability and prevent this damage, and also to relocate the air pressure intake to the bottom of the actuator, modified PneuFlex actuators were designed. Wide ribbons, which do not cut through the silicon as easily, were used as a replacement for the original thin fibers. The resulting custom built SPAM structure and its curved motion trajectory is shown in figure 4.2. From this point on, SPAM will refer to this custom built actuator based on the PneuFlex.

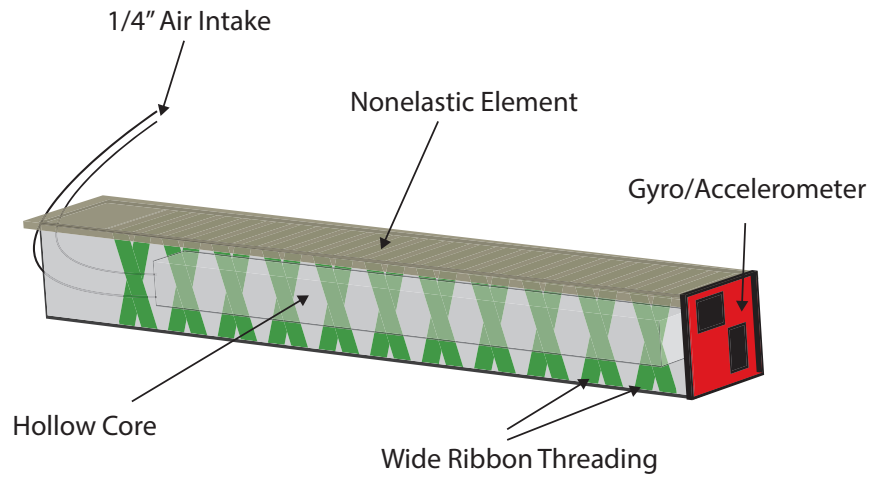


**Figure 4.1:** Components of the modified SPAM-based on the PneuFlex actuator

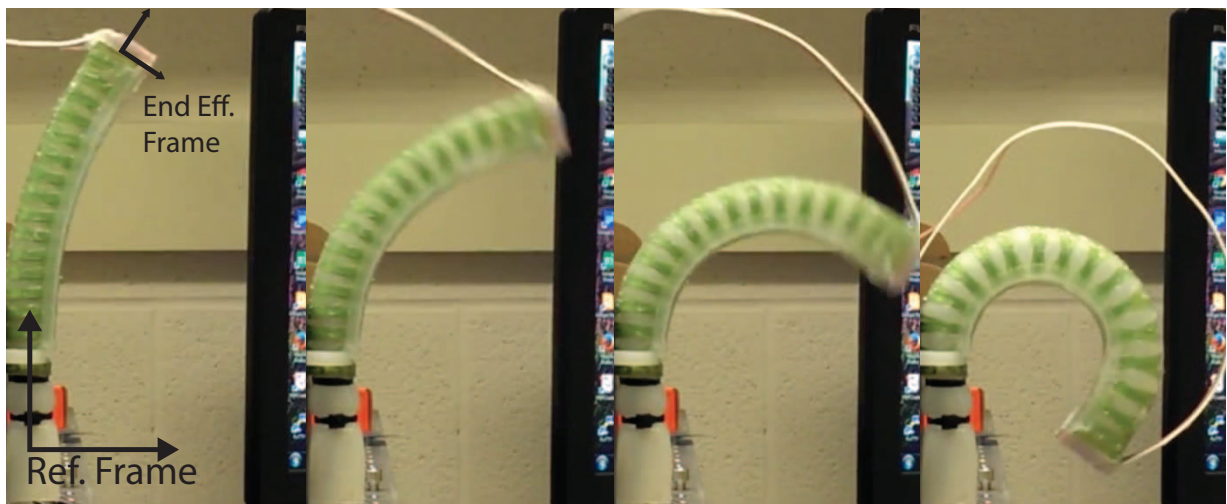


**Figure 4.2:** The motion frames of the custom built SPAM with curved motion trajectory (Note, still frames taken from video)

### 4.1.2 Electromechanical Driving Mechanism

In this section, the pneumatic and the electromechanical systems that enable the actuation of the SPAM are discussed, starting with a brief theoretical analysis of the SPAM actuator. In order to model SPAMs, similar to conventional PAMs [75], conservation of

energy can be used to determine the relationship between the internal pressure  $P$ , actuator volume  $V$ , torque  $\tau$ , and angular position  $\theta$ . The law of conservation of energy states that,  $dW_{out} = dW_{in}$  where for SPAMs the output work is  $dW_{out} = -\tau d\theta$  and the input work is  $dW_{in} = (P - P_{atm})dV$ . Combining these equations results in:

$$-\tau d\theta = (P - P_{atm})dV. \quad (4.1)$$

Equation (4.1) suggests that the output torque and angular displacements of the SPAM are determined by its internal pressure and its changing geometry during motion. Since this geometry change is pre-determined by the physical design, internal pressure is the only parameter available for controlling the force and position output of the SPAM. In this thesis, only the position output of the SPAM is a concern.

Pulse Width Modulation (PWM) of high-speed valves ([43, 44, 45]) is used to control the internal pressure of the SPAM actuator. The main benefits of PWM with high-speed valves are low size and cost, quick response time or low latency, low hysteresis, and relatively linear operating regions [44]. In the PWM approach, the duty cycle of the high-speed valve determines the output pressure of the valve. Thus, this duty cycle is the control signal of the feedback closed-loop controller.

Figure 4.3 depicts the pneumatic circuit of the system which is similar to the open-loop experimentation circuit depicted in figure 3.9. Many of the components of the closed-loop driving circuit are the same as the components in the open-loop circuit. The high-speed 3/2 valve used is Festo's MHE2-MS1H-3/2G-M7-K, capable of switching at 330 Hz. Pressure is provided to the valve by a pressure source (P15 TC by Werther Internationals) and pressure regulator (NAW2000-N02-2 by SMC) pair. The electronic circuit of the closed-loop system is also similar to the circuit for the open-loop system. The pressure sensor (MPX5500DP by Freescale) provides analog electronic feedback on the internal pressure of the SPAM. The analog signal is read by the 12-bit ADC of a Teensy 3.1 microcontroller. The orientation of the SPAM is measured using the ITG3200 gyroscopic sensor by InvenSense which interfaces with the Teensy 3.1 microcontroller over I<sup>2</sup>C. In the closed-loop control system, the controller is implemented on the Teensy 3.1 and the PWM control signal for the valve is provided by one of Teensy's 16-bit PWM outputs. The PWM signal is fed to a switching mode MOSFET that drives the high-speed valve at its rated voltage of 24V.

One of the main disadvantages of using high-speed valves for pressure control is that the output pressure is not smooth. The output pressure of the valve is produced by the valve pushing in or letting out high pressure packets of air at the rate of switching. This

discrete application and exclusion of air, while providing variable mean pressure at different switching duty cycles, results in a high magnitude of noise at the output pressure of the valve. This noise makes the readings from the pressure and the gyroscope sensors noisy as well, which will complicate the feedback control task using these readings. In order to reduce the magnitude of noise in the system, a pneumatic Low Pass Filter (LPF) is designed and implemented. Figure 4.4 shows a picture of the pneumatic LPF. It consists of two main pneumatic components: the pressure tank and the pneumatic resistance. The pressure tank is a syringe and the pneumatic resistance is provided by inserting a porous plug into the output tube of the LPF (here, we used a pipe cleaner). This low cost noise filtering solution provides the ability to fine tune the low pass filter in a simple and quick manner by changing the volume of the syringe or the length of the porous plug. By tuning these two parameters, at 3mL syringe volume and 2.5cm porous plug length, the magnitude of oscillation on pressure caused by PWM was reduced to less than  $\pm 5\%$  at 50% duty cycle.

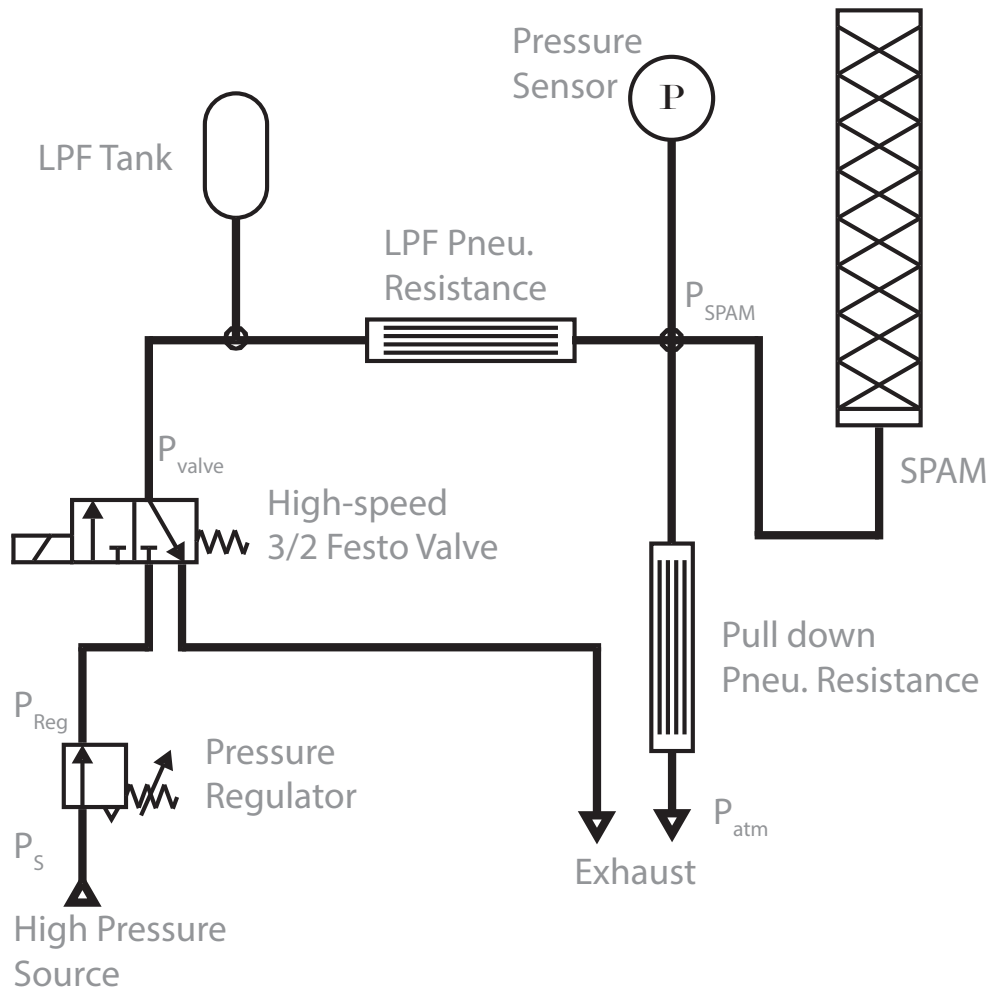


**Figure 4.3:** The pneumatic circuit for the control of the SPAM actuator



**Figure 4.4:** Pneumatic low pass filter

In order to better understand the functionality of the pneumatic circuit, an analogy to electrical circuits can be made using bond graph principles [77]. Figure 4.5 represents the electrical circuit analogous to the pneumatic circuit in figure 4.3. Between these two circuits, pressure is analogous to voltage and mass flow rate to electrical current. The pneumatic LPF corresponds to an RC LPF circuit and the SPAM is represented as a resistive and capacitive load.

The inclusion of the LPF dampens the system and reduces the maximum achievable velocity. In order to rectify this issue, for the angular velocity during pressurization, i.e., during the closing motion, the pressure is increased until required velocities are reached. During depressurization, i.e., opening motion, the SPAM, which is a capacitive and a resistive load, is depressurizing through its own resistance and the resistance of the pneumatic low pass filter. In order to decrease the time constant of this circuit, a pull down pneumatic resistor is introduced at the pressure intake of the SPAM that reduces the time constant of the depressurization circuit by reducing its resistance. Before the addition of the pull-down resistor, the opening motion of the SPAM did not reach the required velocity. The SPAM reaches its maximum opening velocity when, after being pressurized, the duty cycle is switched to zero. This opens the valve fully to the exhaust port, connecting atmospheric pressure to the valve output. In the electrical circuit analogy, 0% duty cycle corresponds to the transistor  $Q2$  being off and transistor  $Q1$  being on, grounding the voltage node  $V_{Valve}$ . Without the pull-down resistor  $R2$ , the capacitor of the SPAM  $C1$  has to discharge through  $R1 + R3$  so the time constant for the discharge is,  $\tau_{w/oR2} = C1(R1 + R3)$ . With the pull-down resistor  $R2$ ,  $R3$  and  $R2$  are in parallel when  $V_{Valve}$  is grounded. Thus,  $C1$  discharge time constant is  $\tau_{w/R2} = C1(R1 + \frac{R2+R3}{R2R3})$ . Since  $R2$  is positive,  $\tau_{w/oR2} > \tau_{w/R2}$  holds for any value of  $R2$ . In other words, the inclusion of a pull-down resistor will reduce the discharge time of the capacitor. For the pneumatic circuit this means that the SPAM reaches atmospheric pressure faster. The equilibrium point of the SPAM with no external force and at atmospheric internal pressure is at the fully open position. Therefore, if atmospheric internal pressure is achieved faster, the SPAM reaches the fully open position faster as well, hence it achieves faster velocities.

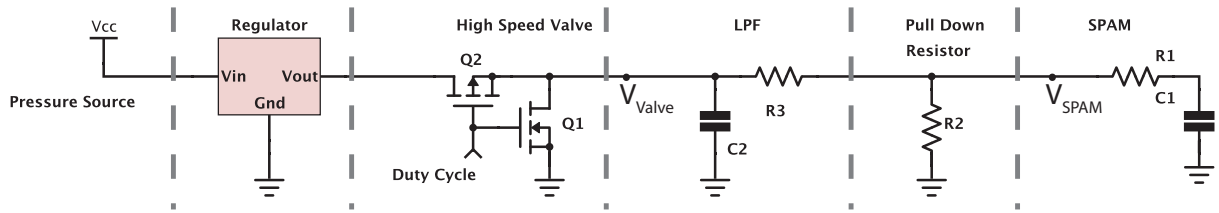


**Figure 4.5:** Electrical circuit analogy of the pneumatic circuit with low pass filter and voltage divider

This low cost and easily tunable pneumatic resistor and low pass filter enable the PWM signalling of fast response pneumatic valves in order to control the out pressure of the circuit. These components reduce noise to levels suitable for feedback closed-loop control. The reduction is achieved without compromising the benefits of using PWM signaling of fast valves, which are: low latency, low hysteresis, and near linear operation region. The SPAM is also capable of achieving fast dynamics with the inclusion of these pneumatic components.

### 4.1.3 Controller

Considering the plant of the SPAM actuation system including the pneumatic circuit, the system can be divided into two sub-plants, as depicted in figure 4.6. The first sub-plant represents the pneumatic circuit of the system and is mainly governed by the switching response of the valve, the LPF and the pull-down resistor, and the SPAM as a pneumatic load. The input to the plant is the duty cycle of the valve and the output is the pressure at the intake of the SPAM. The second sub-plant of the system is the mechanical structure of the SPAM actuator and its end effector orientation response with respect to its internal pressure. The input of the plant is the pressure at the intake of the SPAM and the output of the plant is the end effector orientation. Feedback is provided for the output of both of these sub-plants using the pressure and gyroscope sensors. The sub-plants are connected in series and there is no direct control over the input of sub-plant 2, i.e., the pressure at the intake of the SPAM can only be controlled by the pneumatic circuitry. Thus the controller has to be capable of controlling the end effector orientation of the SPAM using the valve duty cycle as its control signal.

The controller depicted in figure 4.6 is similar to cascade controllers previously used for PAMs [76, 45]. However, instead of using the outer loop position controller to provide a reference for the inner loop pressure controller, the pressure reference trajectory is obtained

by assuming a linear relationship between the internal pressure change of the SPAM and its end effector orientation. The relationship is obtained from the open-loop analysis of the pressure step response of the SPAM actuator. At an internal pressure of 250kPa the SPAM reaches around 3.97 rad steady-state orientation. Using these values, the relationship between pressure and orientation at 101kPa atmospheric pressure is,  $p = \frac{250-101}{3.97}\theta_{ref} + 101$ . This relationship is used to calculate the required pressure reference signal from the end effector orientation reference signal. Both controllers have duty cycle signals as their output which are summed in order to determine the final control signal. The duty cycle signal has 12-bits of resolution and the frequency of the PWM signal is 300 Hz. With respect to this duty cycle resolution, the PID gains of the position controller are,  $K_p = 200$ ,  $K_i = 10$ ,  $K_d = 20000$ . The gain for the pressure controller was 1.63. The controller is tuned so that the control signal is mainly determined by the pressure feedback controller and the position controller will only fine tune the resulting motion of the SPAM actuator towards the desired position trajectories. A Teensy 3.1 microcontroller was used for the implementation of this controller. The controller loop was set at 800 Hz.

By taking advantage of the modifications and solutions discussed in the previous sections, such as reducing the PWM signaling noise of the fast pneumatic valve, it is shown that a linear cascade controller is capable of controlling the non-linear SPAM actuator. The performance of this controller is presented in the following section.

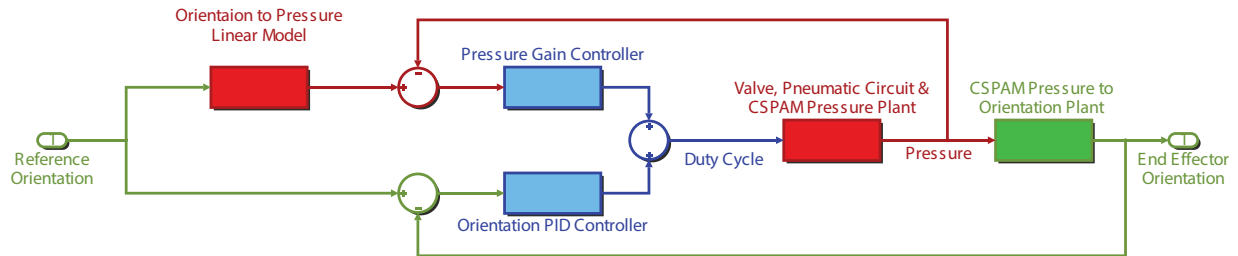


**Figure 4.6:** Pressure-orientation closed-loop controller system for SPAM actuators

## 4.2 Experiments

### 4.2.1 Reference Signal

The parallel controller depicted in figure 4.6 requires orientation reference trajectories. The goal of the controller is to drive the SPAM actuator to emulate, as closely as possible,

the opening and closing of a single finger during affective hand movement. The finger tip orientation data from the dataset [9] of affective hand opening and closing movements described in section 2.1 was used to generate the reference trajectories. More specifically, the finger tip orientation trajectories of the middle finger for the three emotions of joy, anger, and sadness were chosen as the reference signal for the controller. In the dataset from [9], the joint angle data was collected using a data glove at 84 samples/second. The calculated fingertip orientation from this dataset was interpolated to 800 Hz to match the control system frequency, and low pass filtered at a cut off frequency of around 84 Hz, which is well above the Nyquist frequency of the sampled data. The low-pass filtering resulted in a smoother response from the controller.

## 4.2.2 Control System Requirements

The two categories of requirements discussed in 2.2 that apply to the controller performance are the human interaction and velocity and fast dynamic response categories. Achieving the required velocities and accelerations are an important requirement for the controller and the SPAM actuators. Analysis of the SPAM actuators during the design of the system has shown that the required peak velocities and accelerations are achievable in open-loop. Closed-loop control is required to ensure that both the peak velocities and accelerations and the expressive modulations of the velocity during movement are accurately reproduced. Tracking error during the entire trajectory in orientation, velocity, and acceleration are also important if the SPAM movement is to resemble the closing and opening motion of the finger.

Human interaction requirements should also be met by the controller design. Visually, the controller should not introduce artifacts that divert the observer’s attention away from the main goal of emotion conveyance. Therefore, behaviours such as visible vibrations are highly undesirable. Physically, the inherent compliance of the SPAM actuator should not be diminished due to aggressive control.

## 4.2.3 Controller Results

Figures 4.7, 4.8, and 4.9 show the end effector orientation, the respective reference, and the tracking error of the joy, anger, and sadness motion trajectories respectively. The motion for joy starts by closing the finger with medium velocities and accelerations. After performing subtle back and forth motion near the closing pose, the finger opens with high velocity and acceleration. The trajectory for anger starts with rapid closing motion of

the fingers. After a period of no motion, the fingers are opened at medium velocities and accelerations. The trajectory for sad starts with a slow closing motion of the fingers and is followed by their slow opening motion. Since a short delay in the response of the controller does not impede emotion conveyance, the response of the system has been slightly time-shifted to align it with the reference signal for all three trajectories.

In order to determine whether the tracking error performance of the system is acceptable for each target emotion, the variation between the end effector trajectories of the non-thumb fingers in the human demonstrations, as illustrated in figures 2.3 to 2.5, are considered. The maximum variation between the trajectories of the non-thumb fingers in the human demonstrations are  $0.87rads$  for anger,  $0.34rads$  for joy, and  $0.27rads$  for sadness. Table 4.1 presents the maximum magnitude and the mean of the orientation tracking error achieved by the IFLS and the proposed controller. The mean error is smaller than the trajectory variation observed in the human demonstrations for all three emotions. From the plots in figures 4.8 and 4.9, it can be observed that the tracking error is below the variation values during the entire trajectory for anger and sadness. The maximum tracking error within all three trajectories occurs during the closing motion of the joy trajectory, shown in figure 4.7. The plot of the tracking error for joy illustrates that, except during the opening motion of the SPAM, the tracking error is smaller than the variation observed in the human demonstrations of joy. In particular, the tracking error is low when subtle movements are performed near the closed pose, where the velocities are lower and tracking error will be more noticeable.

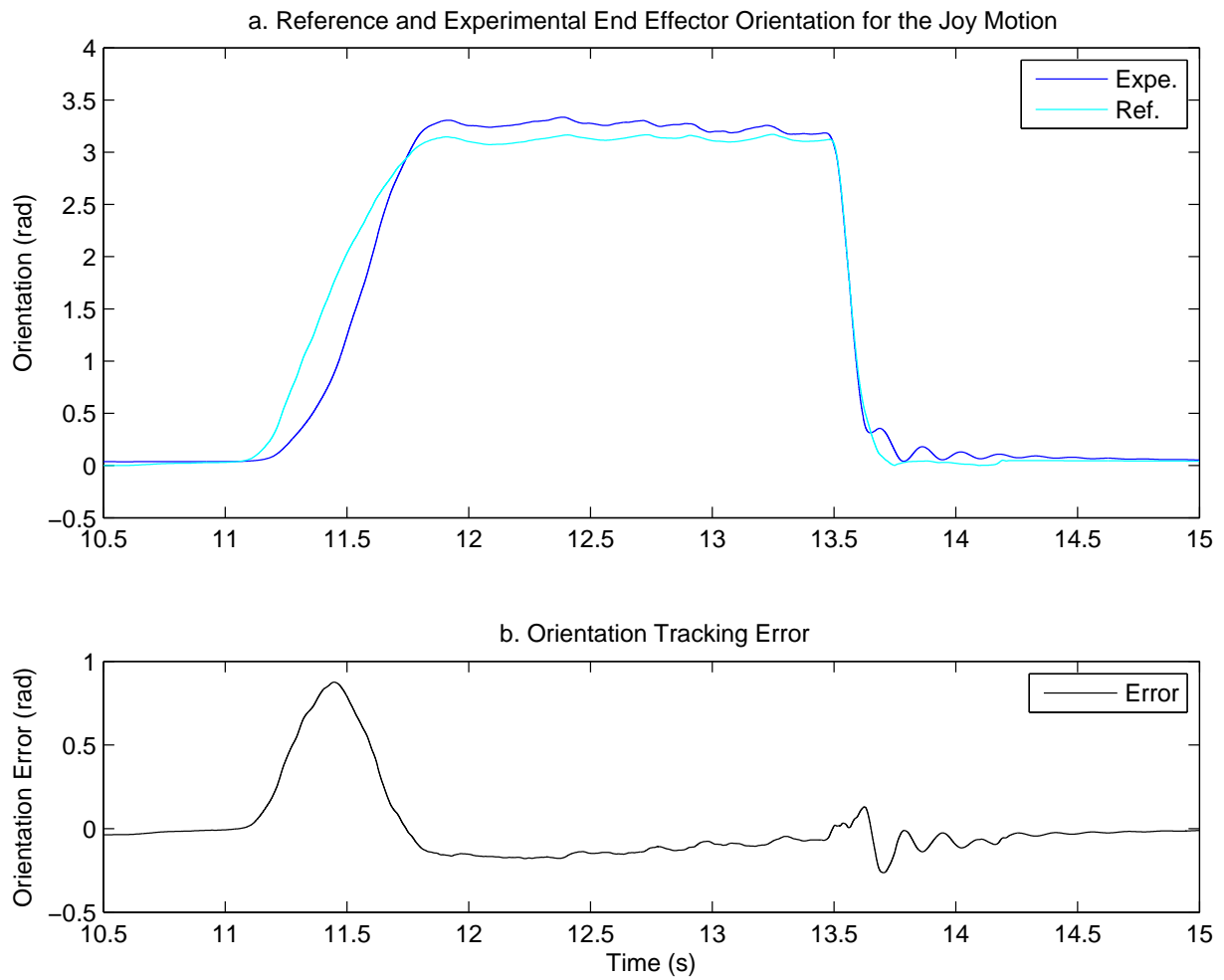


**Figure 4.7:** a. Reference and experimental end effector orientation for the joy motion b. Orientation tracking error

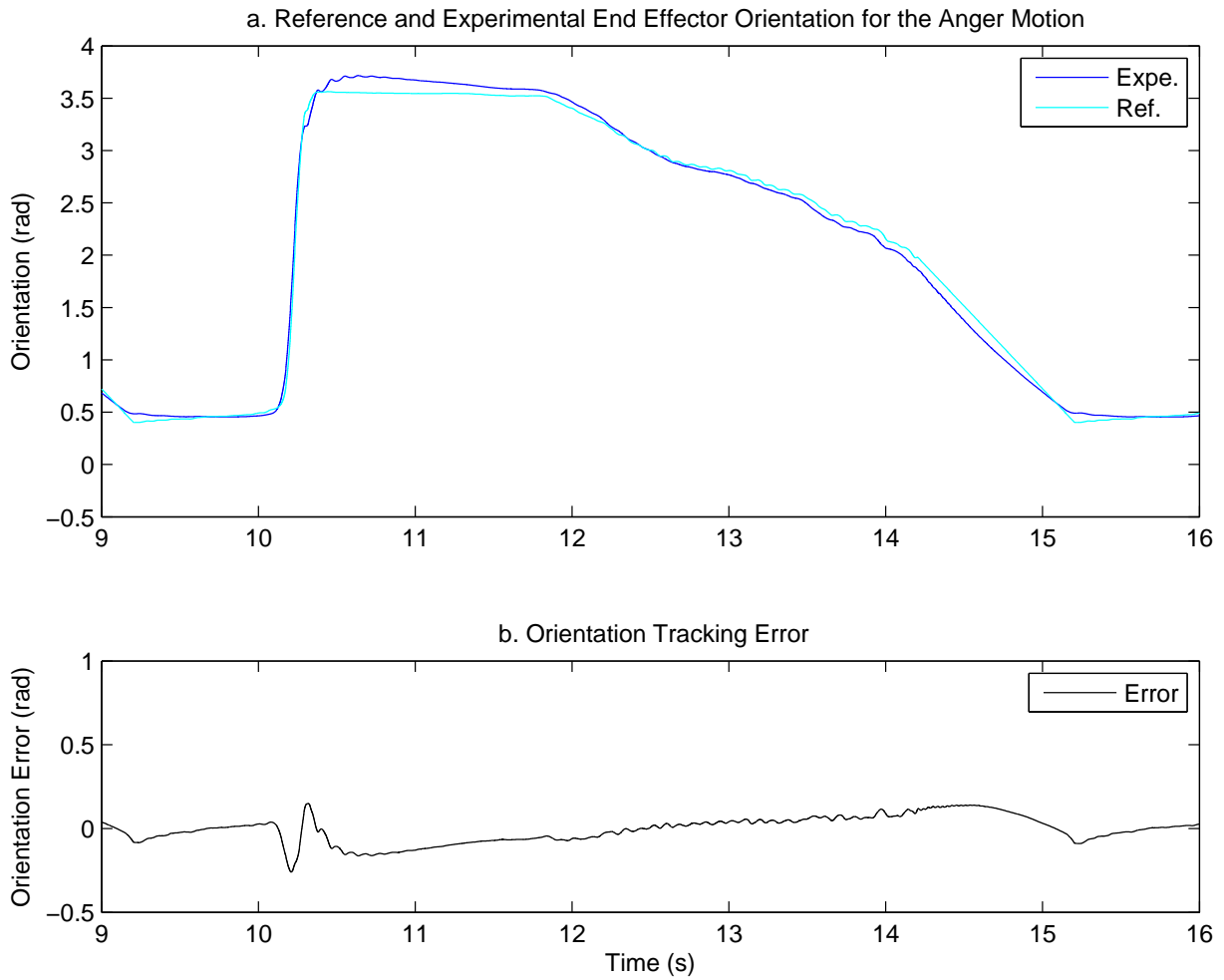


**Figure 4.8:** **a.** Reference and experimental end effector orientation for the anger motion **b.** Orientation tracking error

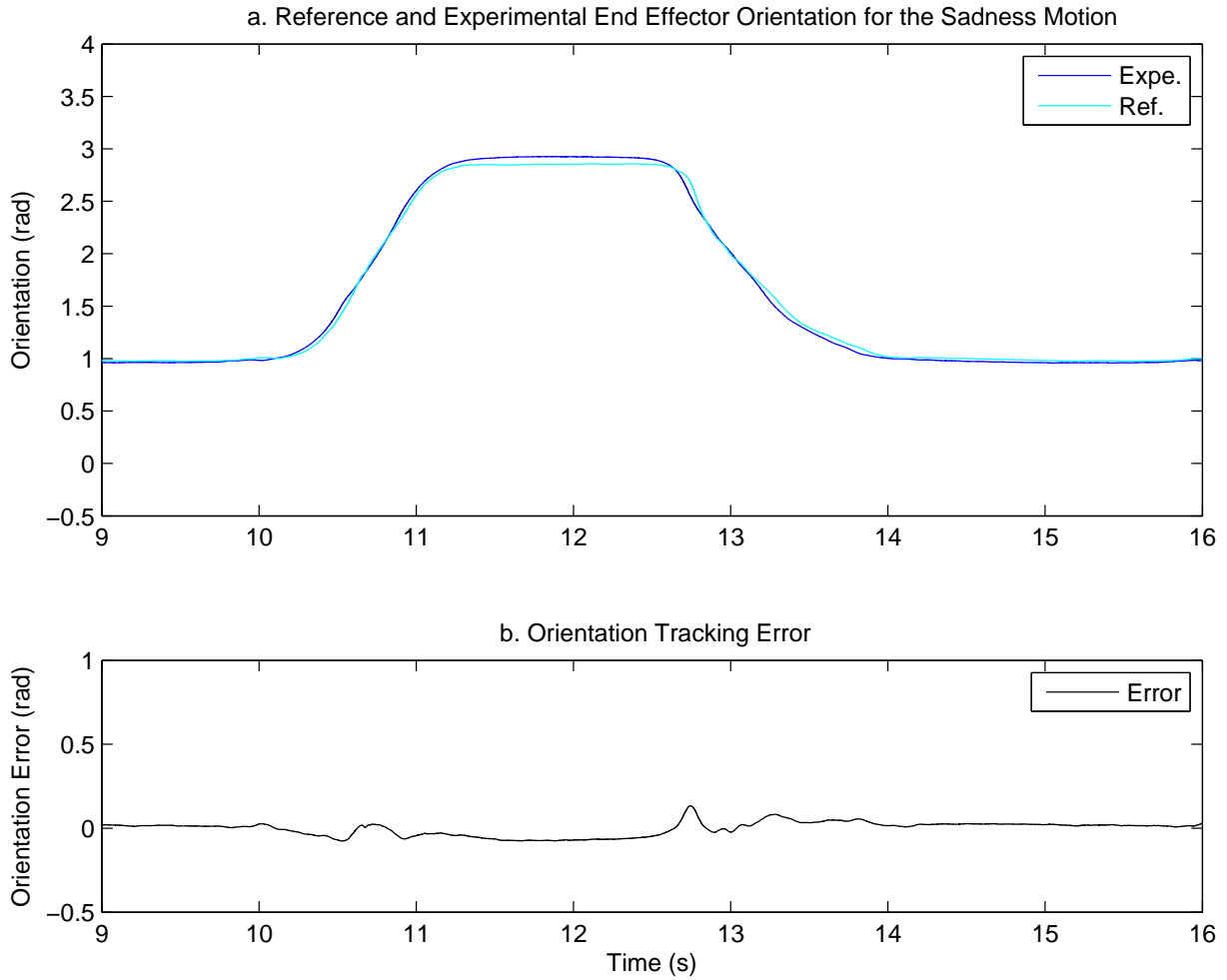


**Figure 4.9:** a. Reference and experimental end effector orientation for the sadness motion b. Orientation tracking error

**Table 4.1:** Measured end effector orientation, velocity, and acceleration error, for joy, anger, and sadness trajectories

	Joy	Anger	Sadness
<b>Orientation Max Error (rad)</b>	0.93	0.322	0.173
<b>Orientation Error Mean (rad)</b>	0.00266	0.0133	0.0289

Figures 4.10, 4.11, and 4.12 show the end effector's angular velocities for the motion trajectories conveying joy, anger, and sadness respectively. The corresponding tracking errors are also presented at the bottom of each figure. The angular velocity is calculated from the measured orientation using discrete differentiation in Simulink. Looking at the peak velocity tracking errors, it can be deduced that the peaks occur during higher velocity closing and opening motions of anger and joy. These error peaks are mainly related to the different velocity profiles of the SPAM actuator and the human finger. For example, in the orientation trajectory plot of joy (figure 4.7), it can be observed that the human finger has a concave-down trajectory while the SPAM has a concave-up trajectory. As the velocity plot confirms, to reach the same orientation value the finger accelerates quickly and decelerates slowly while the SPAM accelerates slowly and decelerates quickly. This discrepancy in acceleration and deceleration behaviours results in tracking error during the closing motion.

The velocity plots also show that especially during the motion trajectory for sadness, high frequency vibrations are present. These vibrations are due to the PWM signaling of the valve. The velocity vibrations have zero mean and as the orientation plots confirm, they do not show up in the orientation change of the end effector and thus are not a concern in terms of interfering with affective capabilities of the motions. The vibrations make the acceleration plots of the motion trajectories very noisy and significantly reduce the analytical merit of the acceleration tracking performance. Therefore, only maximum achieved angular accelerations are discussed and acceleration tracking error is not considered.

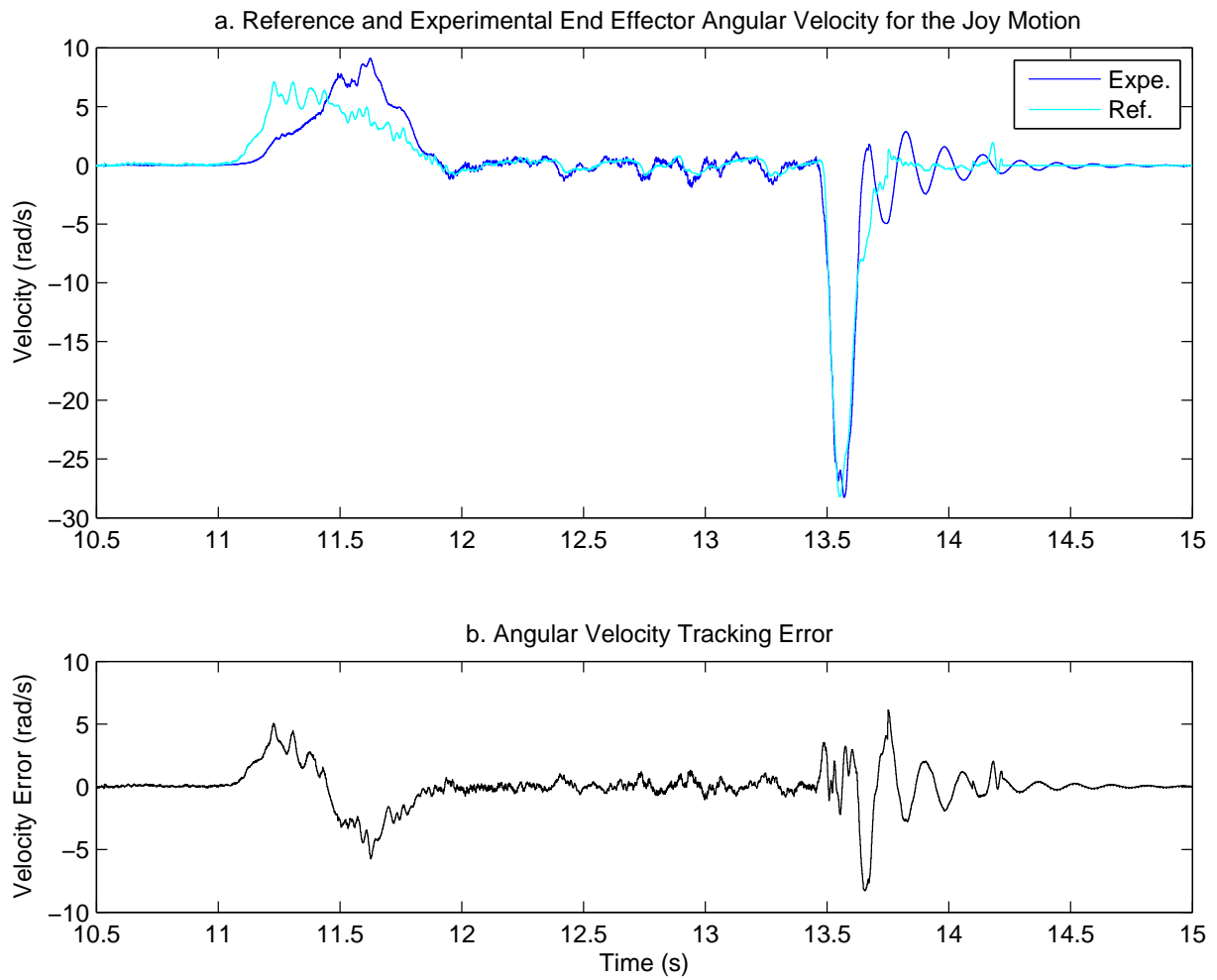


**Figure 4.10:** **a.** Reference and experimental end effector angular velocity for the joy motion **b.** Angular velocity tracking error

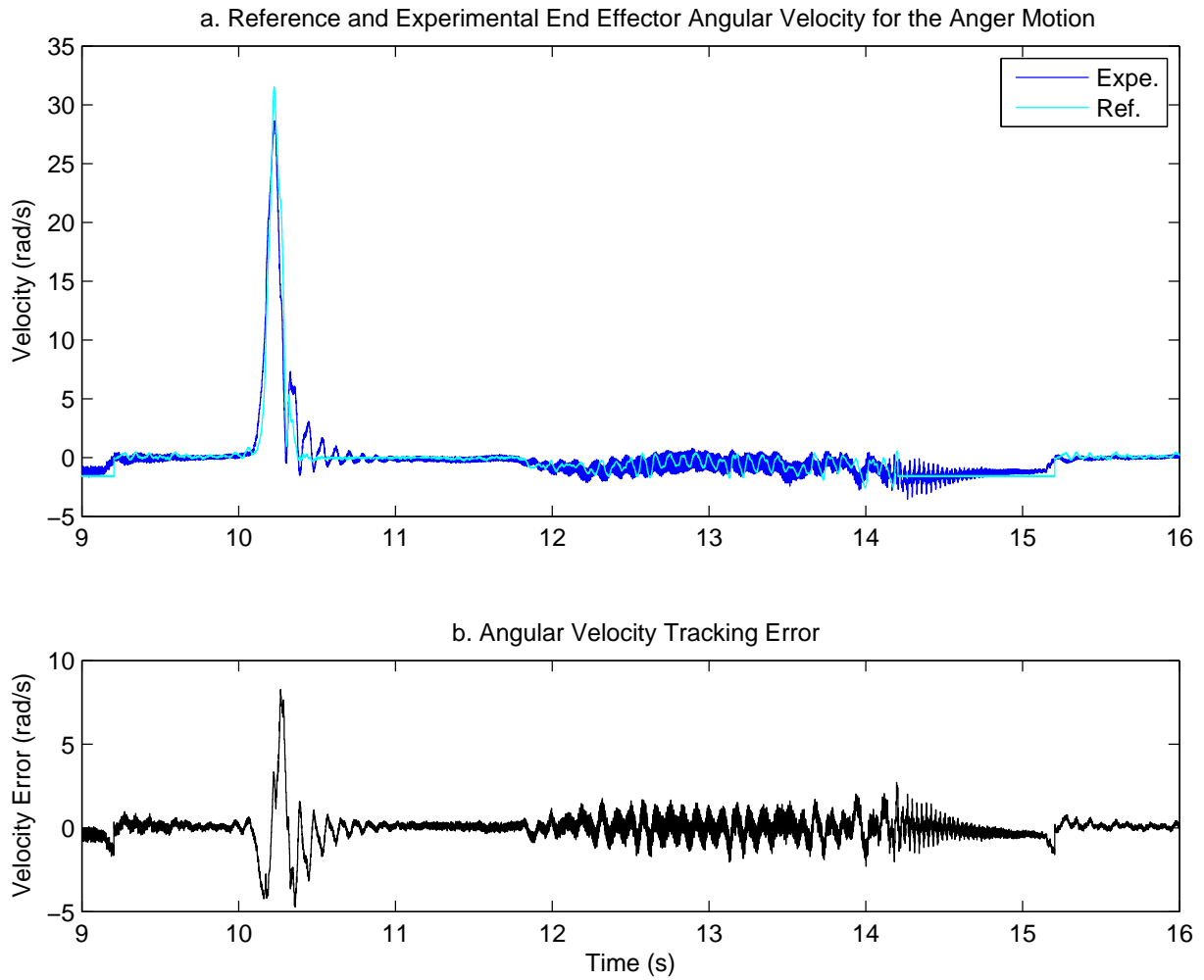


**Figure 4.11:** a. Reference and experimental end effector angular velocity for the anger motion  
 b. Angular velocity tracking error

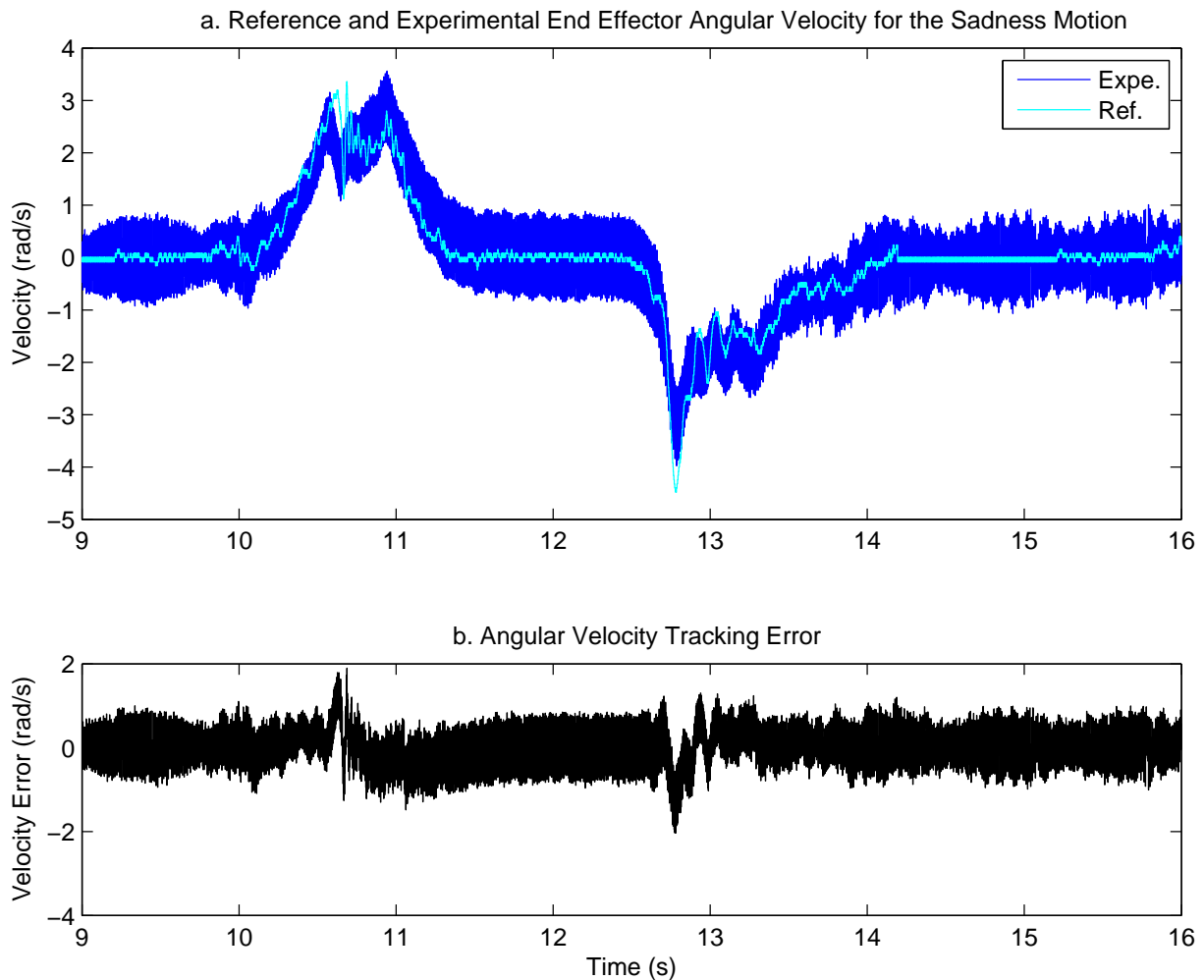


**Figure 4.12:** a. Reference and experimental end effector angular velocity for the sadness motion  
b. Angular velocity tracking error

Maximum and minimum reference and achieved velocities and accelerations are presented in table 4.2. Note that the maximum and minimum values of the reference signal are different from the data presented for the middle finger in table 2.3 because of the low pass filtering of the original trajectories. The maximum reference velocity and acceleration occur during the closing motion of the angry trajectory. These values refer to a rapid flexion motion by the IFLS. Both the achieved and the reference velocities are above the requirements for the flexion motion presented in table 2.3. However, the reference and the achieved accelerations are below the required values. The required acceleration could

**Table 4.2:** Maximum and minimum end effector orientation, velocity, and acceleration, for joy, anger, and sadness trajectories

	<b>Reference</b>	<b>Achieved</b>	<b>Error</b>
<b>Max Velocity</b> ( <i>rad/s</i> )	31.5	28.6	2.89
<b>Min Velocity</b> ( <i>rad/s</i> )	-28.2	-28.3	-0.0338
<b>Max Acceleration</b> ( <i>rad/s<sup>2</sup></i> )	551	607	-55.2
<b>Min Acceleration</b> ( <i>rad/s<sup>2</sup></i> )	-664	-757	-92.4

be achieved by low pass filtering the reference trajectory at higher frequencies and using higher PID gains for the controller. However, higher bandwidth for the LPF of the reference signal reduced the smoothness of the motion and the higher PID gains produced undesirable overshoot. These artifacts were more distracting than the error in maximum acceleration. The minimum velocity and acceleration occur during the opening motion of the joy trajectories. These values refer to a rapid extension motion by the IFLS. Both the achieved and the reference velocities and accelerations are above the requirements for the extension motion presented in table 2.3.

The plots in figure 4.13 present the reference and response trajectories where maximum and minimum velocities and accelerations occur. These plots suggest that the controller can follow the reference velocity and acceleration profiles at critical parts of the trajectories.

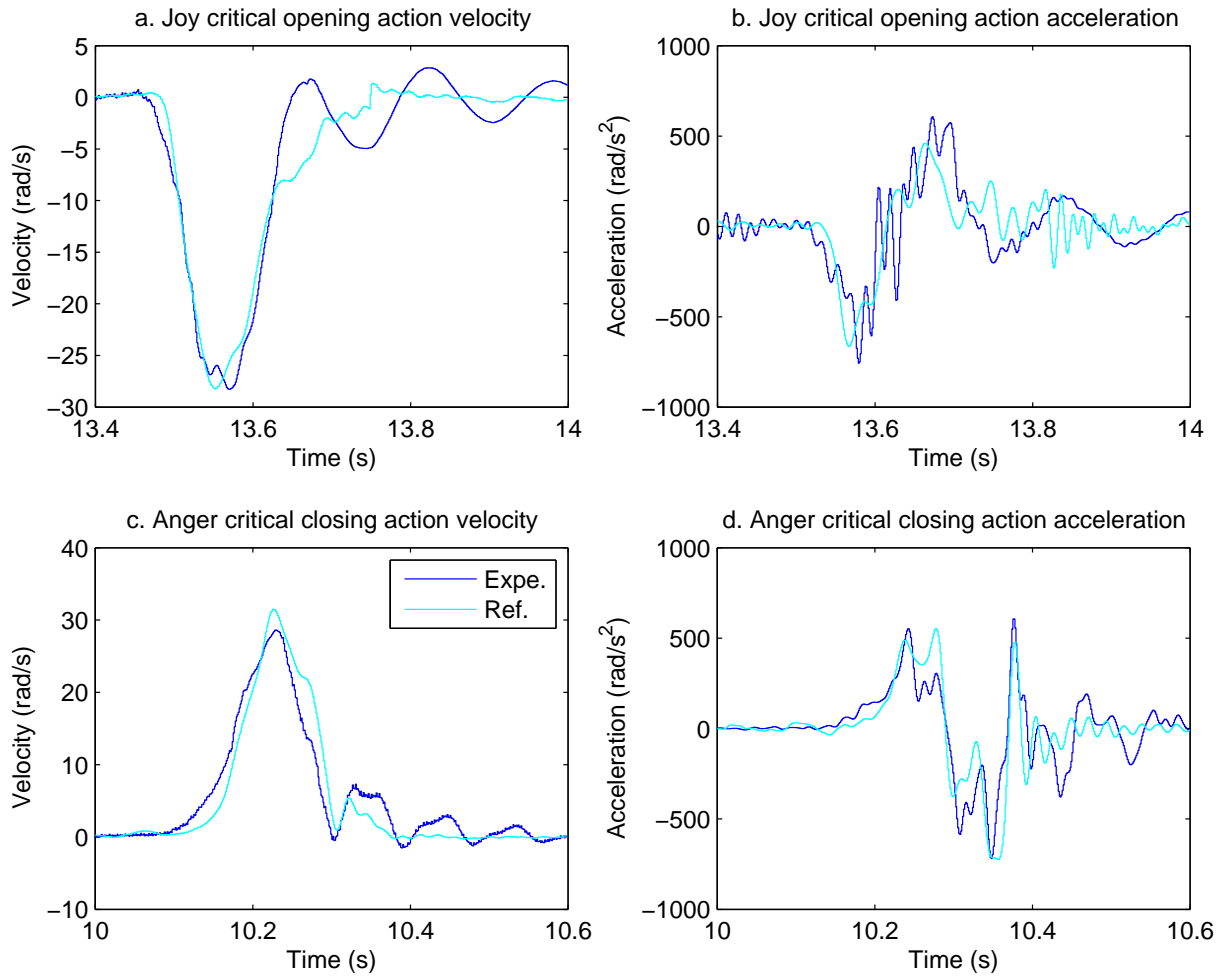


**Figure 4.13:** Reference vs experimental motion response of the sections that include maximum and minimum velocities and accelerations

The experimental results suggest that tracking of the desired affective trajectories using the proposed cascade controller was achievable with small errors. These results also show that the closed loop controller is capable of taking advantage of the fast dynamics of the SPAM actuators and can enable them to achieve the high velocities and accelerations that were obtained during the open-loop analysis of these actuators. Qualitatively, the controller had acceptable results as well. There were no undesirable motions such as visible vibrations that would interfere with the affective qualities of the motion.

# Chapter 5

## WSPAM<sup>1</sup>

The production methods for SPAMs such as PneuNets [67] and SPA [73] require relatively complex molds for producing the elastic hollow core of the actuator. The bend trajectory of these actuators is mainly determined by the relative elasticity of the component materials and the mold design. This allows for a repeatable production method for these actuators. However, because elements such as the fiber in the FMA or the threading in the PneuFlex are not present, there is visible bloating and overstretching during bending. This behaviour can be both visually unappealing and can also accelerate the mechanical degradation actuator. Modifications to the motion trajectory of these actuators can also be relatively cumbersome and complex as they require modifications to the mold of the elastic material. FMA [72] and PneuFlex [69] designs do not suffer from bloating behaviours, however the threading or inclusion of fiber makes the production method very complex and acceptable reproducibility in manufacturing is difficult to achieve.

In this chapter of the thesis, a novel design for SPAMs called wrapped SPAM (WSPAM) is introduced. The WSPAM design produces SPAMs with no bloating behaviours, a highly repeatable manufacturing process, and an easily modifiable motion profile. The WSPAM design consists of a simple silicone hollow core and a customizable silk mesh wrapping. We develop a model relating the steady-state range of motion of the WSPAM to the cutting pattern on the silk mesh wrapping. The model is based on the geometry of the cutting pattern and the elastic properties of the silicone material. A procedure for extracting the parameters of the model is presented. Using the extracted parameters, the proposed model is validated through experiments on WSPAM prototypes, and shown to predict the motion range accurately.

---

<sup>1</sup>An early version of this chapter has been submitted to IROS 2015

## 5.1 WSPAM Production Process

In this section, we introduce the WSPAM design and describe its production process. An WSPAM prototype is shown in figure 5.1.

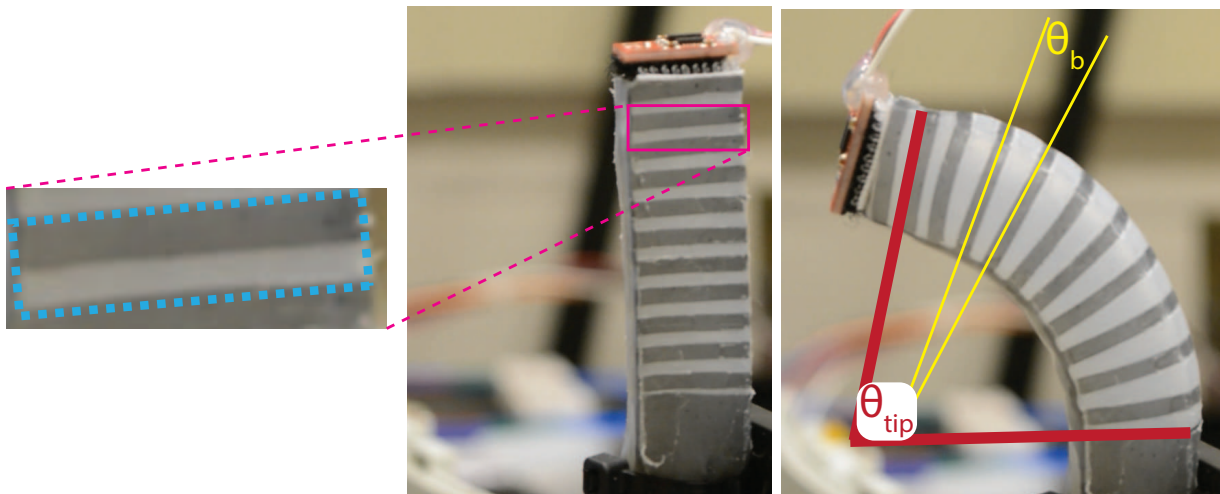


**Figure 5.1:** Cuboid WSPAM in the unpressurised and pressurized state. The silicone gap (white) and mesh cover (grey) pair block is shown on the left

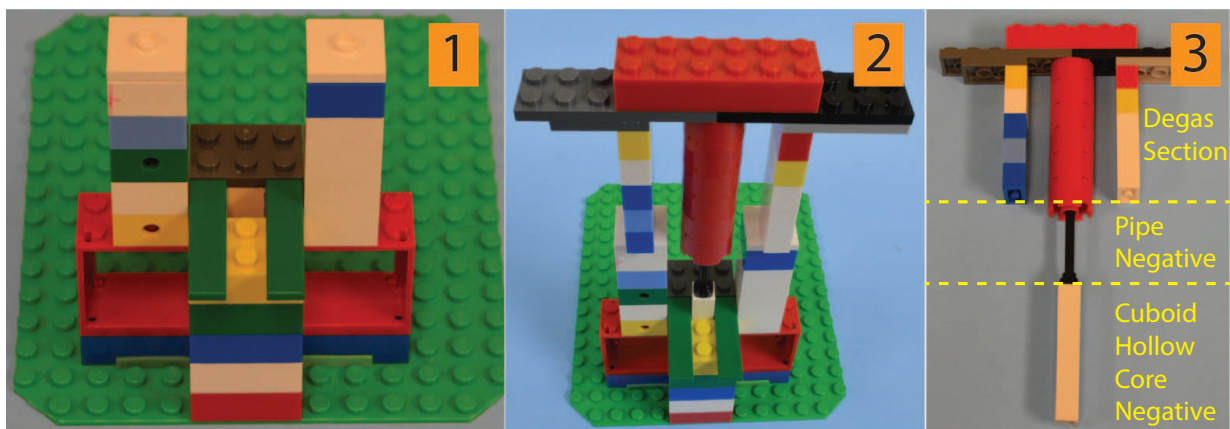
WSPAMs achieve bending motion trajectories similarly to PneuFlex [69] and SPA [73] by utilizing a flexible non-elastic element such as a silk mesh to partially cover its outer surface and cause bending. The novelty in the design of WSPAMs is to wrap the entire outer surface of the hollow elastic core with a purpose-cut silk mesh. The cut patterns are designed such that different sections of the resulting WSPAM will acquire different effective elasticities. This difference in the elasticities will result in different motion trajectories in 3D space. For example, in the case of the cuboid WSPAMs illustrated in figure 5.1, one of the four vertical surfaces and the surface of the tip are entirely covered with silk mesh. The three remaining vertical surfaces are covered by horizontal strips of silk mesh. The vertical surface entirely covered with silk mesh will cause the WSPAM to bend and the silk mesh strips on the other three vertical surfaces will prevent bloating. The geometrical parameters of the stripe pattern determine the motion profile of the WSPAM and are easily modifiable during fabrication. This makes it easy to construct WSPAMs with different motion profiles. From this point on, WSPAM will refer to cuboid WSPAMs with horizontal stripe patterns similar to the WSPAM depicted in figure 5.1.

The mold for producing the hollow cuboid core of the WSPAM is implemented using LEGO pieces and plexiglass. Using LEGO pieces in the design of the mold provides several advantages over prototyping methods such as using 3D printers. LEGO-built structures, unlike 3D printed structures, have smooth surfaces and as the negatives for the surface of the molded silicone, this results in a smooth surface on the molded silicone structure. The sizing standard for LEGOs provides a platform that enables rapid production of various alignment and fixating apparatuses, as will be demonstrated in the following paragraphs. It also results in a standard molded silicone that is compatible with LEGO-built structures. While not as modifiable as 3D-printed molds, LEGO-built molds are also very modifiable and various designs can be experimented with in order to determine the most suitable mold design. Figure 5.2 shows the outer section of the mold for the silicone hollow core. Two of the four walls of the mold are built using plexiglass. This is for two reasons: first, to reduce the number of LEGO pieces, and second, to make the mold transparent so the degassing process, which will be explained further in the text, can be observed more easily.



**Figure 5.2:** LEGO-built outer mold with plexiglass covers

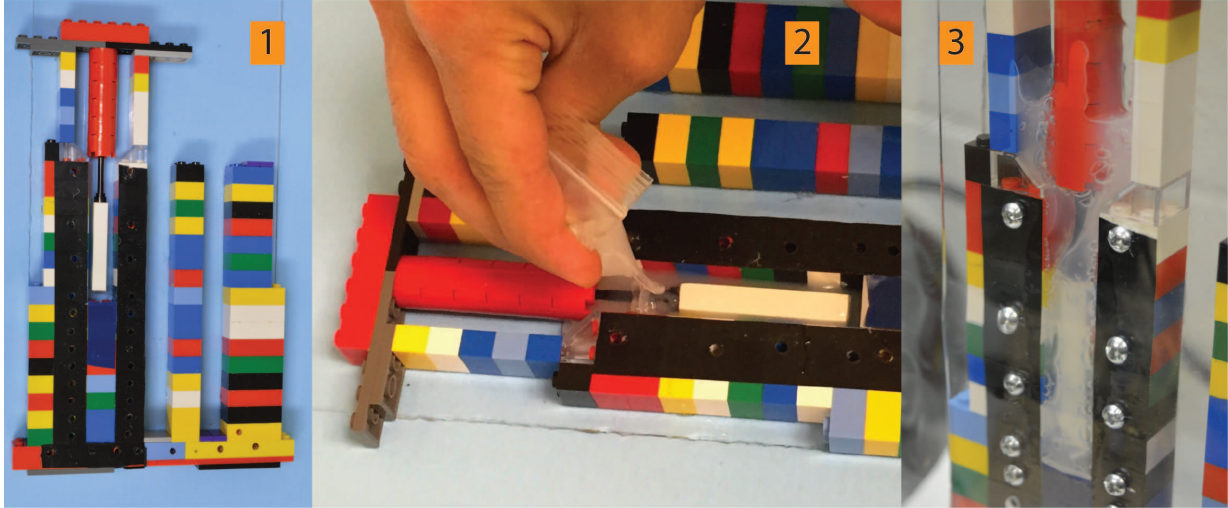
Figure 5.3 shows the process of aligning the inner section of the mold. This piece shown in image number 3 of the figure, will be the negative for the hollow core and the air supply tube. The piece also includes the section for the excess silicone during the degassing process. The LEGO pieces of this part of the mold are not permanently attached together. This is because, after the silicone cures, the inner mold has to be pulled out of the cured part and this process requires high forces. If the LEGO pieces are attached together, bending and damage can occur to the more delicate LEGO pieces. By allowing the LEGO pieces to come apart, this process will be simplified and much less damaging to the LEGO pieces. However, because the LEGO pieces can come apart, they cannot be permanently aligned. As a result, the apparatus shown in image number 1 of figure 5.3 was designed using LEGOs in order to align the inner part before it is attached to the rest of the mold. The alignment process sets the height of the pipe negative that can slide into or out of the de-gas section. It also aligns the cuboid negative with the outer cuboid mold. Image 2 of the figure shows the alignment process for the inner part.



**Figure 5.3:** Pictures of the alignment procedure and apparatus **1:** Alignment apparatus **2:** Aligning the inner LEGO-built mold **3:** Aligned internal mold

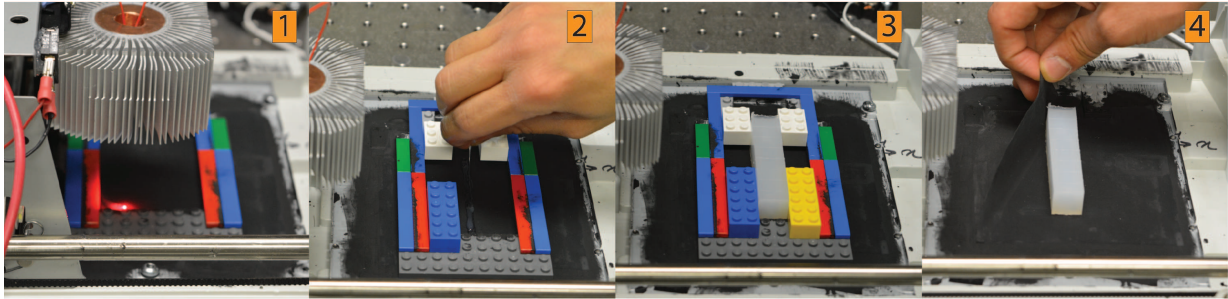
The assembled mold with both the inner and the outer part is shown in image 1 of figure 5.4. This mold is laid horizontally on a flat surface and silicone is poured into the mold as depicted in image 2 of the figure. The silicone used for the WSPAM production is the two part EcoFlex slow 10 silicone. Note that safety glasses and chemically protective gloves should be used when handling the silicone. 10 mL of each parts of the silicone were mixed thoroughly together resulting in 20mL of uncured silicone. After pouring the silicone, the plexiglass cover is attached to the mold using 1/8" bolt and screws. Next, the silicone filled mold is placed vertically in a vacuum chamber for de-gassing. The de-gassing process

is depicted in image 3 of figure 5.4.



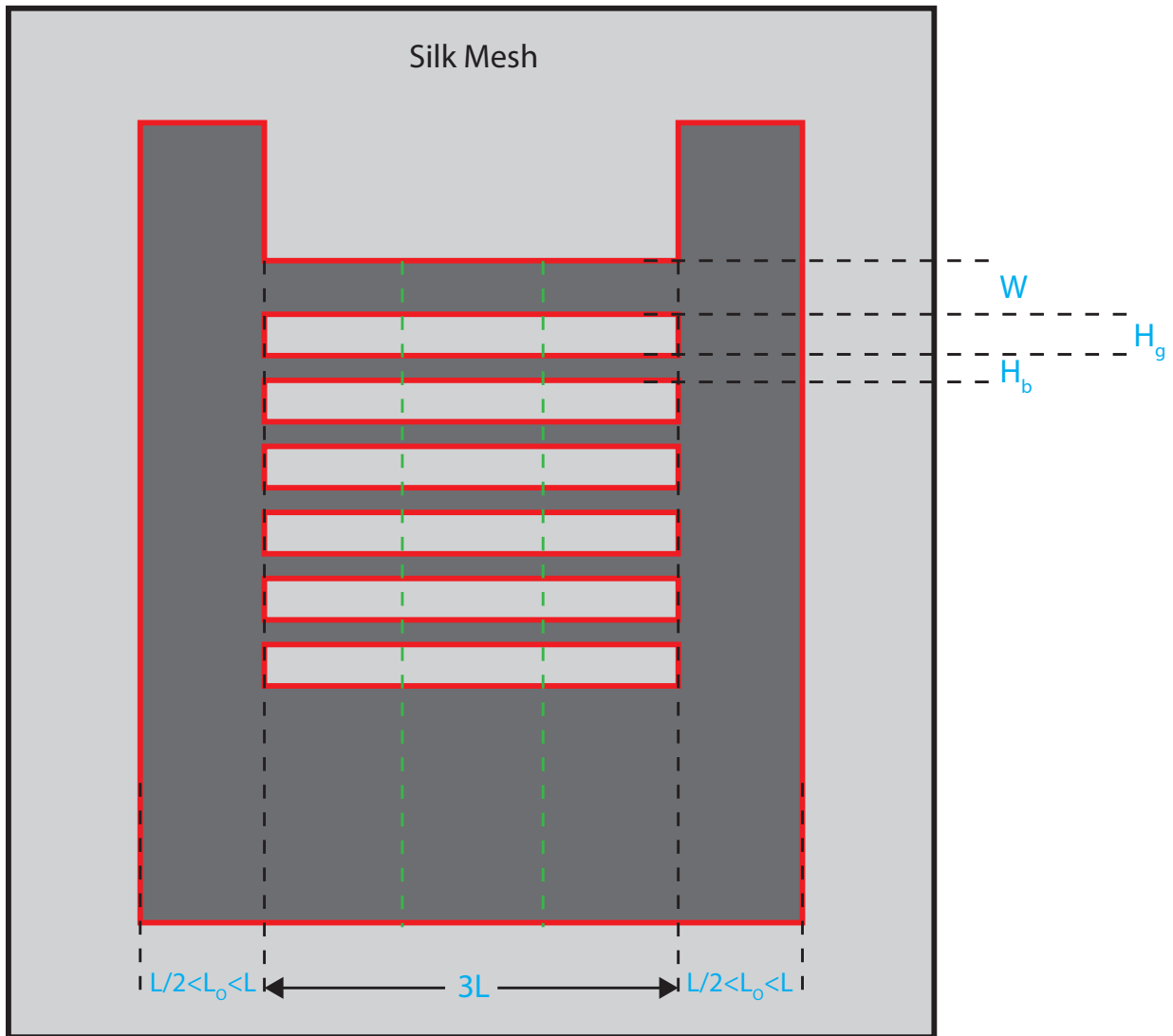
**Figure 5.4:** Pictures of the silicone molding procedure **1:** Assembled mold **2:** Pouring the silicone into the mold **3:** De-gassing of the silicone

Figure 5.5 demonstrates the process of cutting the silk mesh and aligning and fixating the mesh to the silicone core. First, the silk mesh is placed on the cutting plate of the laser cutter and is colored black using diluted water-soluble color such as acrylic paint. The mesh is colored black so that it can absorb more laser energy and thus can be cut with lower power lasers. The coloring with diluted color also ensures that the mesh does not have any waves and is smoothly and flatly stuck to the cutting plate of the laser cutter. Note that other flexible materials that are not stretchable and can be cut with a laser cutter can be used instead of silk mesh. As shown in image 1 of the figure, after the color dries, the laser cutter cuts the desired WSPAM pattern on the mesh. A sample cut pattern is illustrated in figure 5.6. In the figure, red lines demonstrate the lines the laser cutter needs to cut.  $W$  is the width of silicone wall at the tip.  $H_g$  is the height of the gap section.  $H_c$  is the height of the cover section.  $L$  is the width of the cuboid silicone core of the WSPAM.  $L_O$  is the overlapped portion of the uncut mesh which will become the motion restricting portion of wrapping that causes bending. The laser cutter is custom built from scrap computer peripherals. The laser diode is extracted from a DVD writer, and mounted on a laser diode housing. A CPU heatsink is modified to be used for cooling the laser diode, purchased online. The laser diode module is attached to a 2D CNC which is built using stepper motors from scrapped scanners and printers. Note that proper laser protection eye wear has to be used during the operation of the laser cutter.



**Figure 5.5:** Pictures of laser-cutting the mesh and aligning the silicone core **1:** Laser cutting the silk mesh **2:** Pouring adhesive silicone for fixing the silicone core **3:** Aligning and fixating the silicone core to the laser-cut mesh **4:** Removing the fixated silicone core

After the pattern is cut, adhesive silicone is then poured on top of the mesh. Around 2mL of adhesive is poured in the middle section of the cut mesh and alignment LEGO pieces are put in place. The alignment pieces are the  $2 \times 8$  pieces in blue and yellow and the  $2 \times 3$  pieces in white, which are placed on the mesh in order to make sure the silicone core is precisely placed in the middle of the cut mesh, the portion that is illustrated with dashed green lines in figure 5.6. When the adhesive is cured, the silk mesh, which is attached to the silicone core, can be pulled off the cutting board as shown in image 4 of figure 5.5. Because the material of the mesh melts during the laser cutting process, the cut areas are stuck to the mesh and need to be removed using tweezers with slight force.



**Figure 5.6:** Sample laser cut pattern for WSPAM. The red line indicates the lines the laser cutter needs to cut.

Using the jig in image 1 of figure 5.7, the silk mesh is completely wrapped around the silicone core. Notice the uncut part of the mesh sticking out of the jig which is the motion restricting side of the WSPAM that causes it to perform bending motion. This part also includes the mesh cover for the tip of the WSPAM. About 6mL of adhesive silicone is poured on the three naked vertical faces of the silicone core. After the mesh and the core

are placed in the apparatus, the remaining parts of the mesh, which cover the tip and the bending face of the core, are tucked into place and as shown in image 2 of figure 5.7, a cover is clamped over them to keep everything in place while the silicone cures. Image 3 of figure 5.7 shows the cured SPAM still in the wrapping apparatus.

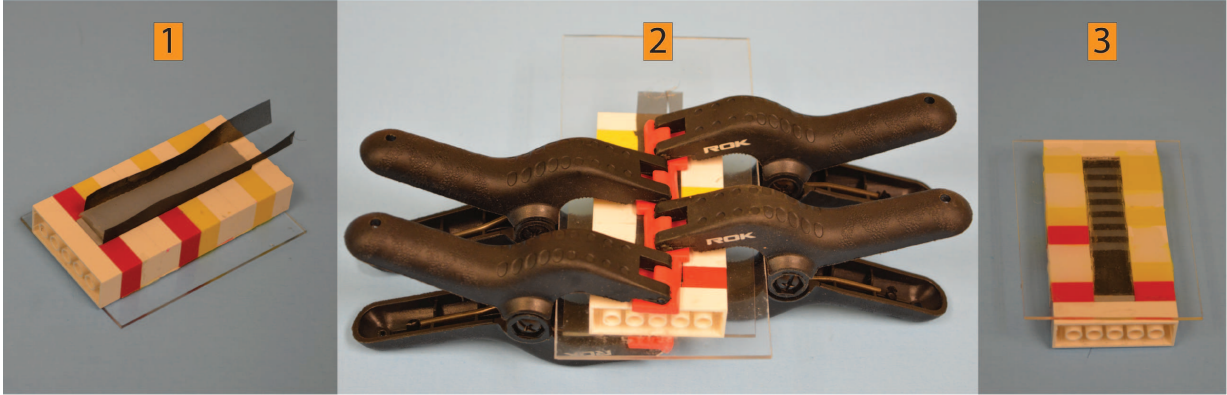


**Figure 5.7:** Pictures of the procedure for precisely wrapping the mesh around the core **1:** Applying adhesive silicone and wrapping the laser-cut mesh around the core **2:** Clamped curing process of the silicone core and mesh **3:** cured WSPAM still in the wrapping apparatus

After the adhesive silicone on the wrapping cures, the WSPAM is ready to be pressurized and perform the motion unique to the laser-cut pattern of the mesh.

## 5.2 Steady state modelling

In this section, a model is developed for the deformation of the WSPAM during pressurization. This model focuses on the angular displacement of the tip of the WSPAM when it reaches the equilibrium point after pressurization. A pressurized WSPAM is depicted in the right most panel of figure 5.1. The middle panel shows an unpressurised WSPAM. It can be seen from this image that the WSPAM consists of a series of silicone gap and mesh cover pair blocks. An image of one of these blocks, outlined with a blue dotted rectangle, is depicted in the left panel in figure 5.1.

The angular displacement of the tip of the WSPAM as shown in figure 5.1 can be defined by,

$$\theta_{tip} = \sum_i \theta_{bi}, \quad (5.1)$$

with  $\theta_{bi}$  being the angular displacement of the  $i^{th}$  block. Therefore, in order to model the angular displacements of the tip of the WSPAMs, the angular displacement of the gap and cover blocks needs to be modelled.

The gap and cover block of the WSPAMs is a hollow cuboid piece of silicone partially covered with silk mesh. Figure 5.8 illustrates the cross-sectional area of the WSPAM, with wall width  $W$  and wall length  $L$ . Figure 5.9 illustrates the side views of an unpressurised and pressurized block. The block is divided into two stacked sections. The top section is covered by silk mesh on all four vertical sides and has height  $H_c$ . The gap section is covered by silk mesh on one vertical side and has height  $H_g$ . The height of the block is therefore  $H_b = H_g + H_c$ . On the right side of figure 5.9, the pressurized state of the block is illustrated, depicting the forces that the block experiences and their resulting net torque and angular displacement.

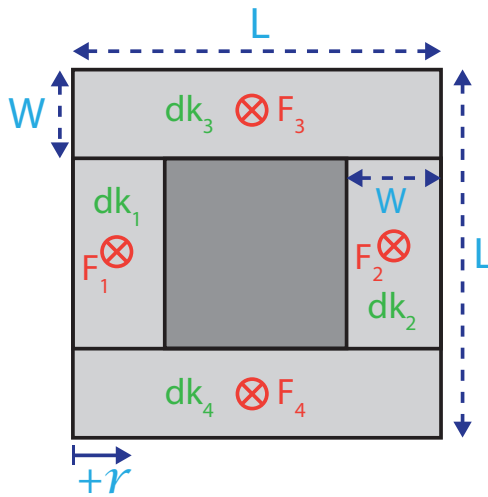


**Figure 5.8:** Parameters of the gap and cover block from top view.  $W$  is the thickness of the silicone wall,  $L$  is the width of the WSPAM with a square cross section.

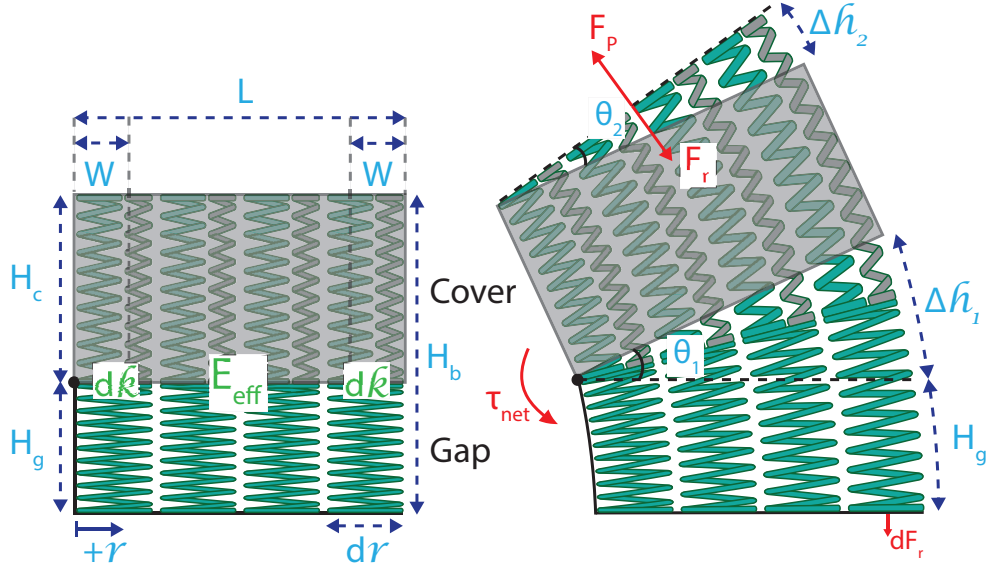


**Figure 5.9:** The physical parameters of the gap and cover block

The total angular displacement of the block is defined as  $\theta_b = \theta_1 + \theta_2$ .  $\theta_1$  is the angular extension of the block below the cover section and  $\theta_2$  is the angular extension of the block above it. The net torque that the block experiences is,  $\tau_{net} = \tau_P - \tau_r$  with  $\tau_P$  being the pressurization torque caused by  $F_p$  and  $\tau_r$  being the reaction torque caused by the reaction force  $F_r$ . Both  $F_p$  and  $F_r$  are illustrated in figure 5.9. When the block is fully pressurized and stops its motion,

$$\tau_P = \tau_r. \quad (5.2)$$

The force  $F_p$ , illustrated in figure 5.9, is exerted by the internal pressure of the WSPAM on its tip. The area of the tip that experiences that pressure is  $(L - 2W)^2$ . Thus,

$$F_p = (L - 2W)^2 P. \quad (5.3)$$

The moment arm of this force is  $\frac{L}{2}$ . Therefore, the torque exerted by the internal pressure  $P$  is,

$$\tau_p = \frac{L}{2} (L - 2W)^2 P. \quad (5.4)$$

In order to determine  $\tau_r$ , the reaction torque of the block at equilibrium, the gap and cover block is considered as a parallel combination of infinitesimal linear springs with spring

constant  $dk$ . An effective Young's modulus  $E_{eff}$  is assigned to the gap and cover block in order to define  $dk$  in terms of the geometrical parameters of the block.  $E_{eff}$  is assumed to be uniform along the cross sectional area of the block. The infinitesimal spring constant  $dk$  is determined by multiplying  $E_{eff}$  by its infinitesimal cross sectional area and dividing by its constant height  $H_b$ . Note that  $E_{eff}$  of the block is different from the Young's modulus of the silicone alone because the cover mesh has a considerable effect on the elasticity of the silicone. The effects of the mesh cover on the elasticity of the hollow silicone core will be discussed in section 5.3.

As illustrated in figure 5.8, the  $dk$  in each wall of the WSPAM is defined separately. Equations 5.5 and 5.6 define these spring constants along the  $r$  axis, illustrated in figure 5.8.

$$dk_1 = dk_2 = E_{eff} \frac{L - 2W}{H_b} dr \quad (5.5)$$

$$dk_3 = dk_4 = E_{eff} \frac{W}{H_b} dr \quad (5.6)$$

The infinitesimal force exerted by each of the spring blocks can be defined as  $dF_i = \Delta h dk_i$ , where  $\Delta h = \Delta h_1 + \Delta h_2$  is the total amount of extension of the block, as illustrated in figure 5.9. The extension at any point along the  $r$  axis is,

$$\Delta h = r\theta_1 + r\theta_2 = r\theta_b. \quad (5.7)$$

The force  $F_i$ , as shown in figure 5.8, exerted by each wall is thus the integration of  $dF_i$  along the  $r$  axis. Since the moment arm along the  $r$  axis is perpendicular to these forces, the resulting infinitesimal torque is,

$$d\tau_i = r \times dF_i = r \times \Delta h dk_i = r^2 \theta_b dk_i. \quad (5.8)$$

Thus the resulting torques from each wall are,

$$\begin{aligned}
\tau_1 &= \int_0^W E_{eff}\theta_b \frac{L-2W}{H_b} r^2 dr \\
&= E_{eff}\theta_b \frac{L-2W}{H_b} \int_0^W r^2 dr \\
&= \frac{E_{eff}\theta_b(L-2W)}{3H_b} r^3 \Big|_0^W \\
&= \frac{E_{eff}\theta_b(L-2W)W^3}{3H_b}
\end{aligned} \tag{5.9}$$

$$\begin{aligned}
\tau_2 &= \frac{E_{eff}\theta_b(L-2W)}{3H_b} r^3 \Big|_{L-W}^L \\
&= \frac{E_{eff}\theta_b(L-2W)(L^3 - (L-W)^3)}{3H_b}
\end{aligned} \tag{5.10}$$

and for  $\tau_3$  and  $\tau_4$  the dks from equation 5.6 result in,

$$\begin{aligned}
\tau_3 = \tau_4 &= \frac{E_{eff}W\theta_b}{3H_b} r^3 \Big|_0^L \\
&= \frac{E_{eff}\theta_bWL^3}{3H_b}
\end{aligned} \tag{5.11}$$

Therefore, the total amount of torque  $\tau_r$  exerted by the silicone is,

$$\begin{aligned}
\tau_r &= \tau_1 + \tau_2 + \tau_3 + \tau_4 \\
&= \frac{E_{eff}\theta_b}{3H_b} (2WL^3 + (L-2W)(W^3 + (L^3 - (L-W)^3))) \\
&= \frac{E_{eff}\theta_b}{H_b} f(L, W)
\end{aligned} \tag{5.12}$$

Thus, at equilibrium, using equations 5.4 and 5.12 results in,  $\frac{L}{2}(L-2W)^2P = \frac{E_{eff}\theta_b}{H_b} f(L, W)$ . Isolating  $\theta_b$ ,

$$\theta_b = \frac{PH_b}{E_{eff}}g(L, W) \quad \text{where,} \quad (5.13)$$

$$g(L, W) = \frac{L(L - 2W)^2}{2f(L, W)}.$$

Equation 5.13 shows that the amount of motion provided by the gap and cover block is dependent on five parameters: the effective Young's modulus of the block  $E_{eff}$ , internal pressure  $P$ , and the geometrical parameters,  $L$ ,  $W$ , and  $H_b$ .  $P$  is the independent variable and will be the control signal for the position control of WSPAM actuators. Geometrical parameters  $L$  and  $W$  are determined by the mold that is used for constructing the hollow silicone core and their modification requires changes to the silicone mold.  $E_{eff}$  and  $H_b$  are determined by the design of the wrapping fabric which can be modified much more easily than the silicone mold. It should be noted that  $E_{eff}$  depends on both the wrapping and the Young's modulus of the silicone used. To simplify the analysis of the effect of  $E_{eff}$  and  $H_b$  on the angular displacement of the block, the  $L$  and  $W$  parameters are assumed constant and are substituted into function  $g$  to give  $C = g(L_o, W_o)$ . Thus, equation 5.13 simplifies to,

$$\theta_b = C \frac{PH_b}{E_{eff}}. \quad (5.14)$$

### 5.3 Modelling the Effective Young's Modulus

In the development above, an effective Young's modulus  $E_{eff}$  was defined for the entire gap and cover block. In this section, we derive the characteristics of  $E_{eff}$  in more detail. The formulation in Section 5.2 allowed for the definition of the spring constant  $dk$  in terms of the geometrical parameters of the infinitesimal linear spring. The infinitesimal spring itself can be represented by a series combination of two linear springs, similar to the spring system depicted in figure 5.10. One spring represents the cover section and one represents the gap section of the block. The associated Young's moduli of the springs of the cover and gap sections are represented by  $E_c$  and  $E_g$  respectively. This results in respective spring constants,

$$K_c = \frac{E_c A_o}{H_c} \quad (5.15)$$

$$K_g = \frac{E_g A_0}{H_g}. \quad (5.16)$$

Where  $A_0$  is the cross sectional area of the spring system. While  $A_0$  varies depending on the specific wall geometry, it is constant in each of equations 5.15 and 5.16, and in Figure 5.10, for a given wall of the WSPAM.

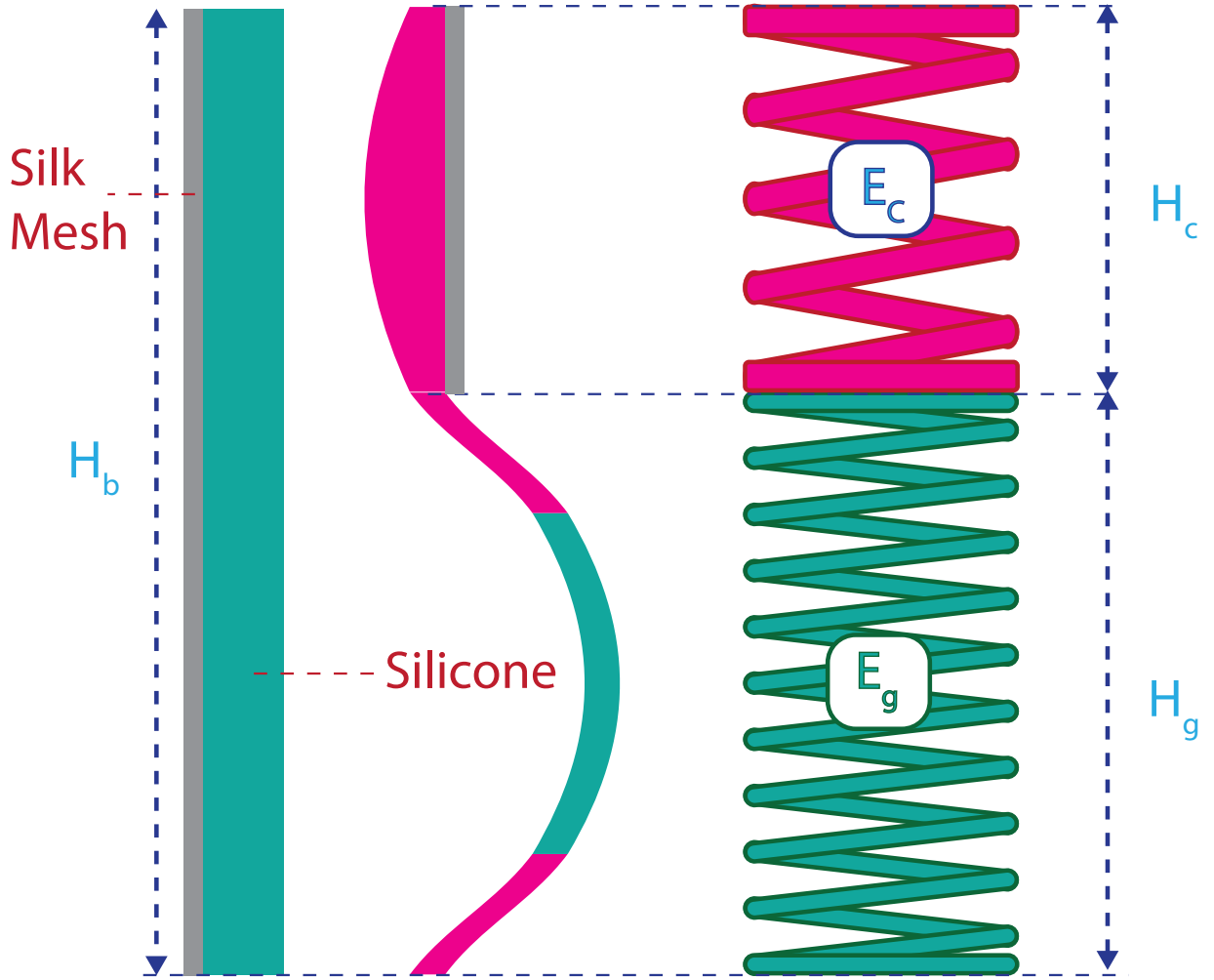


**Figure 5.10:** The left-hand drawing shows a side view of one cover-gap pair block when pressurized and the right-hand drawing shows the equivalent spring model. Bending of the block was not depicted for illustration purposes

The effective spring constant of the block can be defined as

$$K_{eff} = \frac{E_{eff}A_o}{H_b}. \quad (5.17)$$

Since the springs representing the cover and gap sections are in series, the effective spring constant of the block can also be defined as,

$$K_{eff} = \frac{K_g K_c}{K_g + K_c}. \quad (5.18)$$

Substituting 5.16 and 5.15 into equation 5.18 results in,

$$K_{eff} = \frac{E_c E_g A_o}{E_c H_g + E_g H_c}. \quad (5.19)$$

Equating equation 5.17 with equation 5.19 and isolating for  $E_{eff}$  results in,

$$E_{eff} = \frac{E_c E_g H_b}{E_c H_g + E_g H_c}. \quad (5.20)$$

Substituting equation 5.20 into equation 5.14 results in,

$$\theta_b = CP \frac{H_g}{E_g} + CP \frac{H_c}{E_c}. \quad (5.21)$$

Intuitively, the covered section is not as elastic as the gap section, therefore  $E_g < E_c$ . Physical experiments were performed next to determine if this model is a good representation of the WSPAM spring block and also to estimate values for  $E_c$  and  $E_g$ .

During the initial stage of the experimental verification of the model for the WSPAM spring system, it was discovered that as  $H_c$  is increased, there is a critical height  $H_s$  beyond which the Young's modulus of the cover section switches to a higher value. Figure 5.11 depicts the case when  $H_c > H_s$ . This figure illustrates that when  $H_c > H_s$ , the middle part of the silicone behind the cover mesh, which is depicted in light blue in the figure, does not contribute to the elasticity of the cover section as much as the end sections of the silicone, depicted in red. This behaviour of the cover section can be modelled as a system of springs depicted on the right side of figure 5.11. The middle section silicone can be modelled as a parallel spring system of the mesh and silicone with Young's moduli  $E_m$  and

$E'_c$  respectively. The silk mesh is non-elastic meaning its Young's modulus  $E_m$  is large i.e.  $E_m \gg E'_c$ . Thus the Young's modulus of middle section is,  $E_m + E'_c \approx E_m$ . The spring representing the middle section is in series with two springs at both ends that represent the end sections of the covered silicone. Thus, when  $H_c < H_s$ , there is no middle section silicone and the Young's modulus stays at  $E_c$ . However when the rest height reaches  $H_c > H_s$ , the cover section switches to a series spring system. This means for  $H_c > H_s$  the block consists of a series configuration of three types of springs. In other words, equation 5.21 can be extended to,

$$\theta_b = CP \frac{H_g}{E_g} + CP \frac{H_s}{E_c} + CP \frac{H_c - H_s}{E_m} \text{ for } H_c > H_s. \quad (5.22)$$

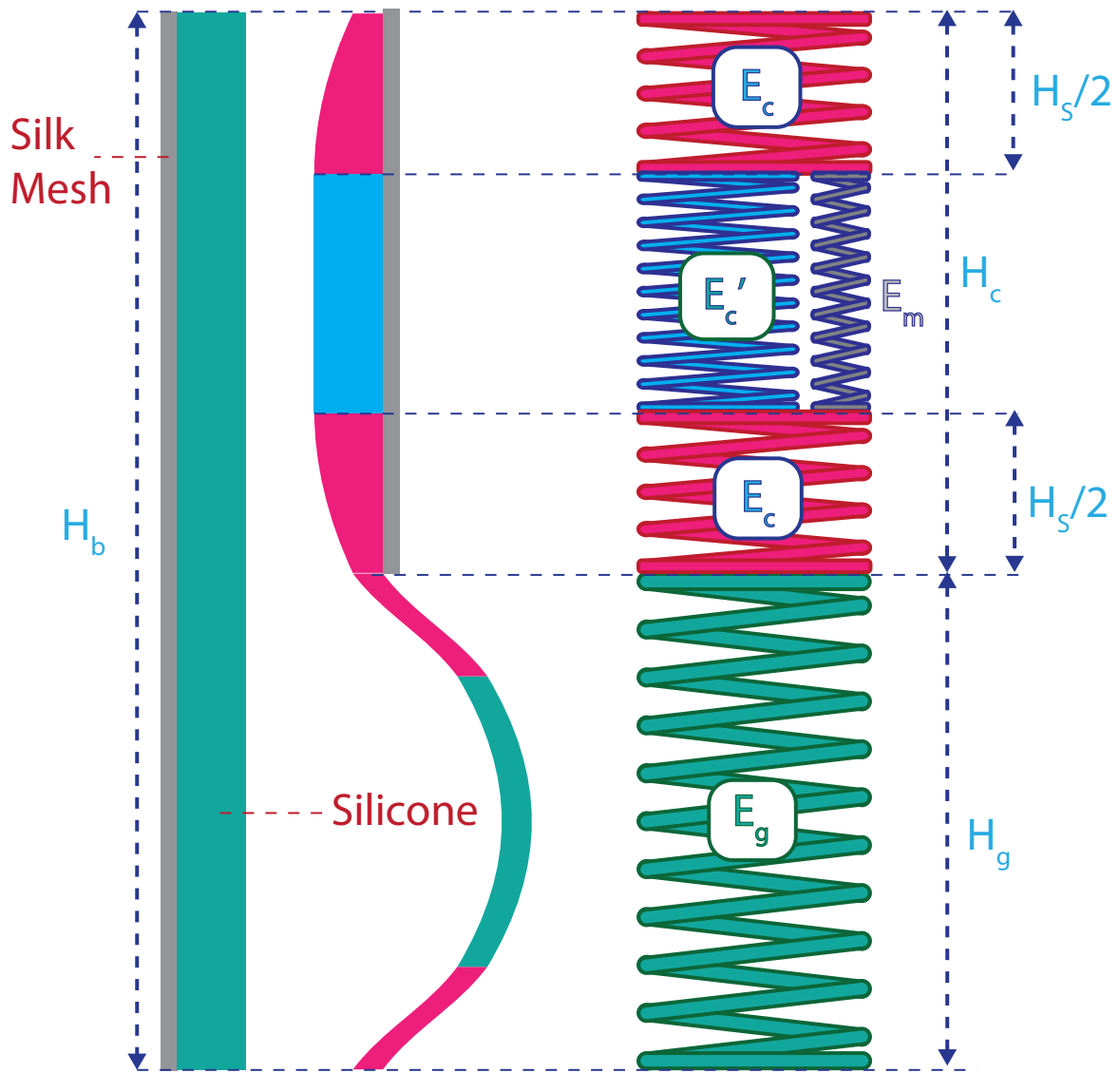


**Figure 5.11:** Cover section saturation model for the spring constant and the illustration of the silicone behaviour when pressurized (Note, in reality the block would bend, the bending was not depicted for illustration purposes)

## 5.4 Experimental Validation

In order to examine the prediction accuracy of the models discussed in the previous section, two different experimental procedures were designed and carried out. The first procedure, which was designed to estimate the parameters in the model, involved the production of gradient WSPAMs, with gradually increasing gap or cover section heights. These WSPAMs provided the ability to test multiple cover or gap heights in one WSPAM. Figure 5.12 shows the two gradient WSPAMs that were designed for this experiment.

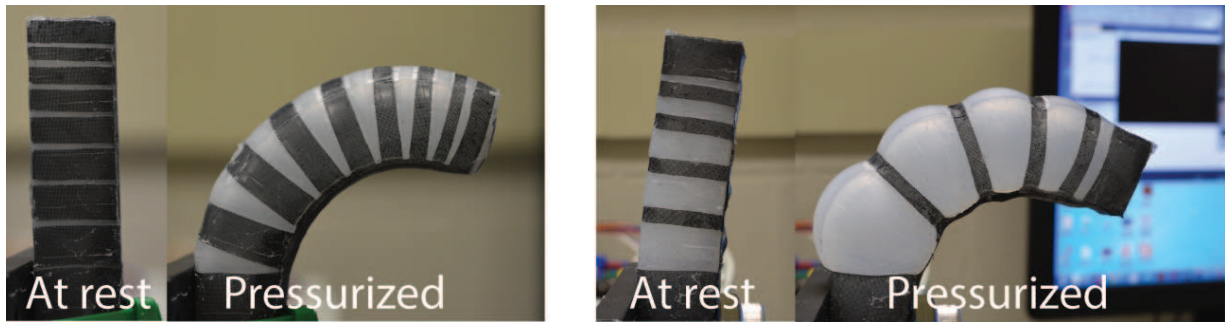


**Figure 5.12:** Gradient  $H_c$  (on the left) and  $H_g$  (on the right) WSPAMs at rest and pressurized

There are 6 collected data points for varying cover section heights and 4 data points for varying gap section heights. Note that the angles of the tip gaps were not included as they are not fully over the hollow core of the WSPAM, and include part of the WSPAM that is solid silicone. The heights were recorded as the number of associated steps of the CNC laser cutter which produced the wrapping, with each step approximately equal to  $0.42mm$ . The angles of the discrete gap-cover blocks are measured from the recorded images using Adobe Illustrator. In all experiments, the geometrical parameters  $L$  and  $W$  were kept the same between WSPAMs in order to keep  $C$  constant. In addition, the operating pressure during each experiment was recorded using an electronic pressure sensor. Since there is a linear relationship between  $\theta_b$  and  $P$ , as shown in equation 5.21, the measured angular displacements were normalized with respect to operating pressure.

Figure 5.13 illustrates the 4 data points for the cover gradient WSPAM (see figure 5.12, left) at constant  $H_c = 8$  and variable  $H_g = 8, 12, 16,$  and  $20$ . using equation 5.21 as the model, which indicates a linear relationship between  $\theta$  and  $H_g$ , a line is fitted through the experimental data points with  $H_g$  as the independent variable. The fitted line is illustrated in figure 5.13. The root mean square error (RMSE) of the fit is 0.0541. With respect to equation 5.21 the slope of the fit is  $\frac{CP}{E_g} = 0.034$ .

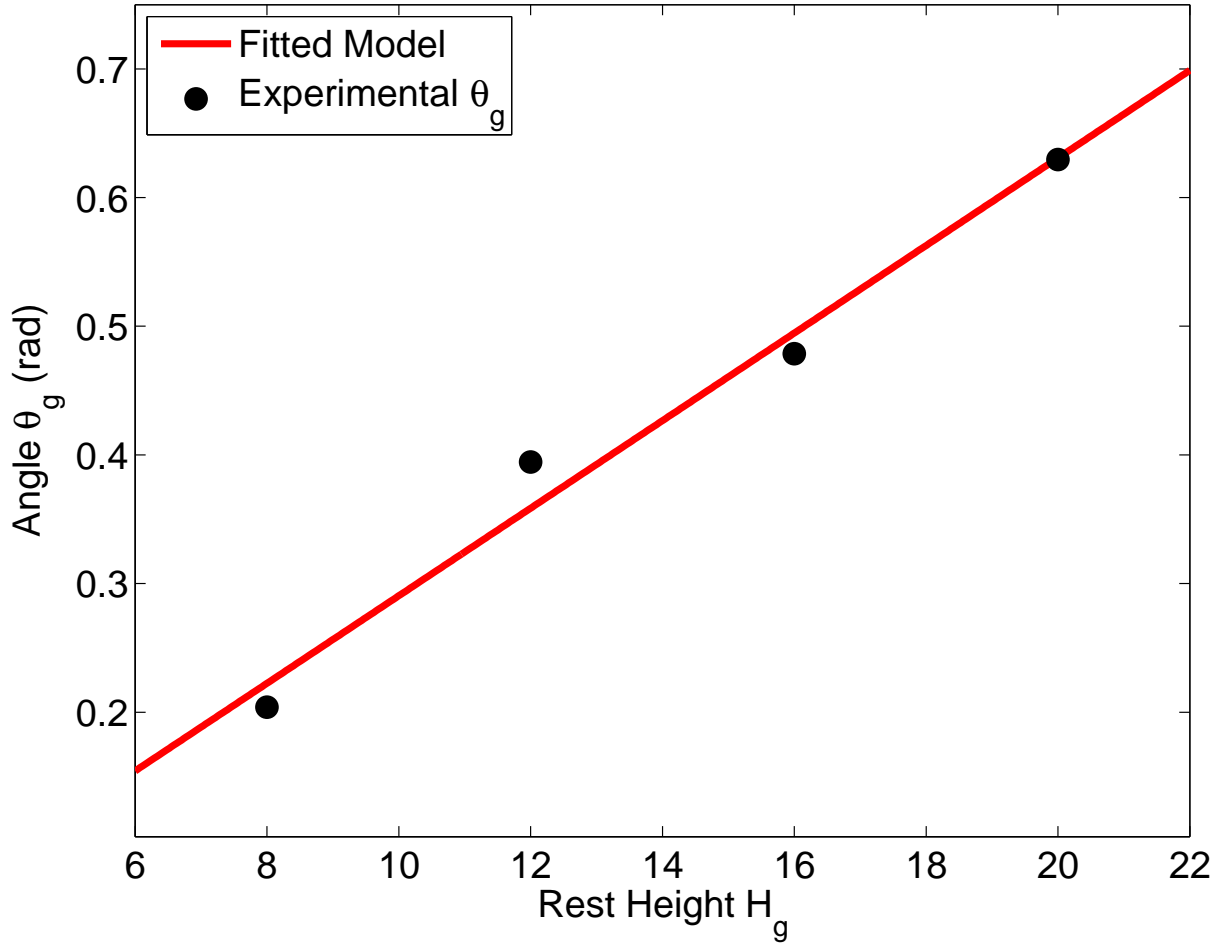


**Figure 5.13:** Simulation and experimental data for  $K_g$  in terms of rest heights  $H_g$

Figure 5.14 illustrates the 6 data points for the gap gradient WSPAM (see figure 5.12, right) at constant  $H_g = 2$  and variable  $H_c = 6, 8, 10, 12, 14$  and  $16$ . Fitting the developed model for variable  $H_c$  is more complex as it involves the determination of the saturation height  $H_s$ . Observing the data points collected for variable  $H_c$  heights, it can be observed that the saturation occurs somewhere between  $H_c = 8$  and  $H_c = 12$ . A line was fitted through the first 3 data points which represent the unsaturated region for cover height  $H_c$ . Another line was fitted through the last 3 data points which represent the saturated region for cover height  $H_c$ . The point where these two line meet is the saturation height,  $H_s = 8.21$ . The fitted function is represented in figure 5.14. The RMSE of the fit is 0.0109. With respect to equation 5.21, the slope of the unsaturated region is  $\frac{CP}{E_c} = 0.0110$ . With

respect to equation 5.22, the slope of the saturated region is  $\frac{CP}{E_m} = 0.0053$ .

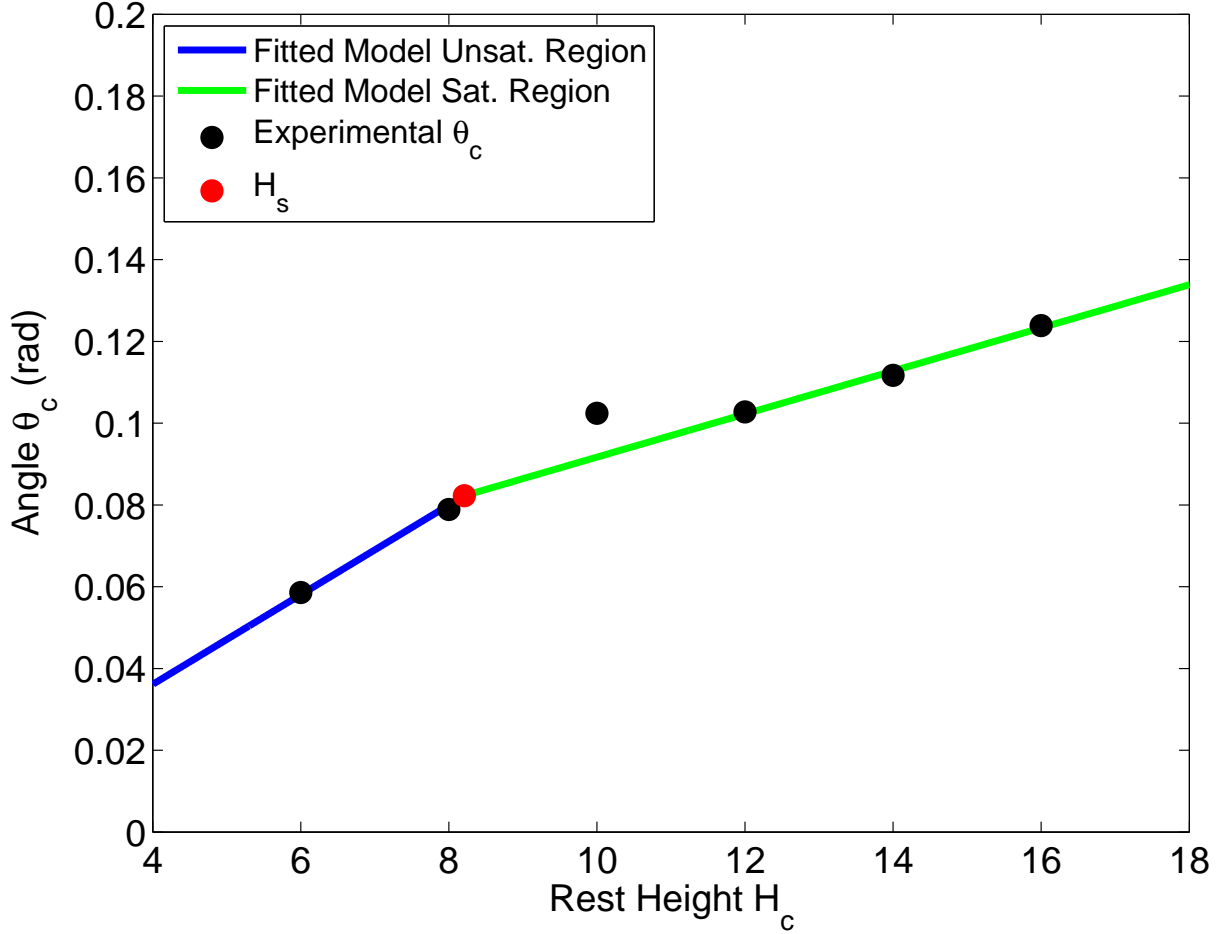


**Figure 5.14:** Simulation and experimental data for  $K_c$  in terms of rest heights  $H_c$

The second experiment investigates the angular displacement of the blocks in WSPAMs with uniform  $H_c$  and  $H_g$  values. While analyzing these uniform WSPAMs, the block height  $H_b$  and block ratio  $r = \frac{H_c}{H_b}$  are more intuitive to work with. Therefore, equation 5.21 and 5.22 which model  $\theta_b$  are rearranged and described in terms of  $H_b$  and  $r$  resulting in equations,

$$\theta_b = CP \frac{H_b(1-r)}{E_g} + CP \frac{rH_b}{E_c} \text{ for } rH_b < H_s. \quad (5.23)$$

$$\theta_b = CP \frac{H_b(1-r)}{E_g} + CP \frac{H_s}{E_c} + CP \frac{rH_b - H_s}{E_m} \quad \text{for } rH_b > H_s. \quad (5.24)$$

Three  $r$  values of 1/4, 2/4, and 3/4 and two  $H_b$  values of 16 and 24 were tested in the experiments. The constructed WSPAMs are illustrated in figure 5.15.

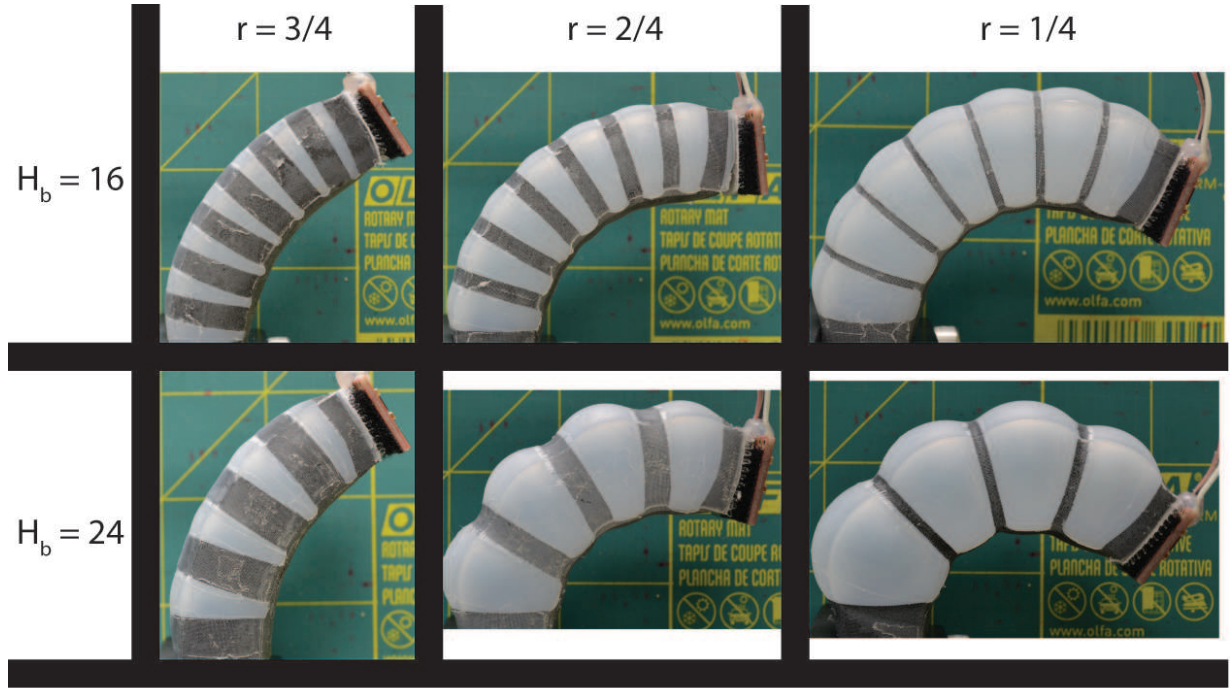


**Figure 5.15:** Pressurized WSPAMs at 3 different  $r$  and 2 different  $H_b$  values. Not that WSPAMs with lower  $r$  have higher  $H_g$  and achieve greater angular displacement but at the cost of a distended, “bloated” appearance.

The angular displacements of the blocks of the WSPAMs were measured from the images using Adobe Illustrator. The average of the measured displacement was assigned as the angular displacement of the block with the specific  $H_b$  and  $r$  values. The angular displacements were also normalized with respect to the internal pressure  $P$ . The resulting angular displacements are plotted in figure 5.16.

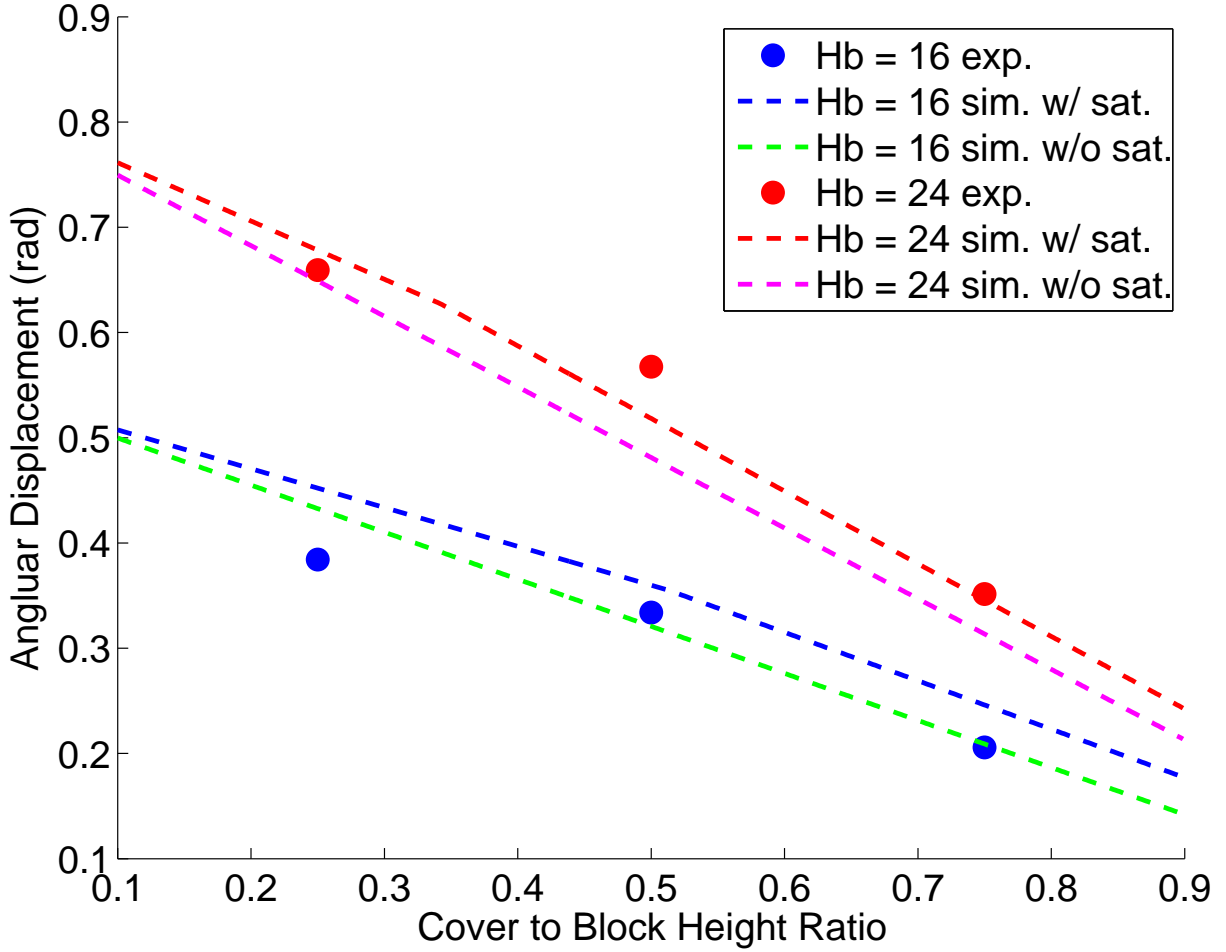


**Figure 5.16:** Simulated and experimental block angular displacement  $\theta_{tip}$  with respect to block height  $H_b$  and block ratio  $r$  in 2D

Figure 5.16 also includes the predicted block angular displacement from the model in equations 5.23 and 5.24. Since  $C$  is kept constant and all the collected data points are normalized with respect to pressure, the fractions  $\frac{CP}{E_g}$ ,  $\frac{CP}{E_c}$  and  $\frac{CP}{E_m}$  obtained from the gradient WSPAM experiment can be used in equations 5.23 and 5.24 to model the angular displacement. The total RMSE of the simulation model versus the experimental data is 0.099. The maximum error which occurs at  $r = 1/4$  and  $H_b = 16$  is 0.0679. These results demonstrate a good fit between the model and the experimental data, showing that the proposed model can be used to predict the angular displacement as a function of the cut and cover pattern. In figure 5.16, results for the simpler model without taking saturation

into account are also illustrated. The simpler model achieves an RMSE of 0.113 with a maximum error of 0.0834. This shows that considering the saturation of the cover section does improve the prediction of the model.

The model presented in figure 5.16 suggests that during the design process of WSPAM actuators, in order to maximize the output angular displacement  $\theta_b$ , block height  $H_b$  needs to be maximized and block ratio  $r$  needs to be minimized. This translates to minimizing cover height  $H_c$  while maximizing  $H_g$ . In a physical system however, there are restrictions on both the cover section height  $H_c$  and gap section height  $H_g$ . If bloating is undesirable,  $H_g$  should only be increased to heights that do not exhibit bloating at the desired working pressures. Also, decreasing  $H_c$  too much can either cause the cover section to tear the silicone over time or the silk mesh at those widths might not be able to withstand the applied pressure and can break. Thus, a robust minimum cover height that does not cause tear in the silicone and a maximum gap height that does not exhibit bloating has to be experimentally determined at the desired working pressure.

# Chapter 6

## Conclusions

Inspired by interactive architecture works such as *Hylozoic Soil* shown in figure 1.1 this thesis develops the design of an interactive finger-like structure called the IFLS, capable of performing motion affective motion trajectories. The design requirements of the IFLS were determined based on the characteristics of human affective motion and interactive architecture applications. In comparison to conventional robotic hand designs, soft pneumatic artificial air muscles (SPAMs) were found more suitable for the design of the IFLS. While SPAMs held great potential for the application in this work, because they are a recent pneumatic actuation technology, a new production and control methodology needed to be developed in order to fully exploit this potential.

Analysis of the open-loop response of the SPAMs demonstrated that these actuators are capable of achieving fast dynamic motions. The first contribution of this paper was designing a closed-loop controller, capable of controlling the fast dynamic response of the SPAM actuator. Innovative designs enabled the application of PWM controller designs previously used for conventional PAM actuators. The innovative designs included providing feedback on the orientation of the SPAM using a gyroscopic sensor, and introducing pneumatic low pass filters and pull-down resistors in order to reduce the high noise levels caused by the PWM signaling in the pneumatic circuit. The implementation of the controller enabled the SPAM to perform affective motions which require high velocities and accelerations. From a qualitative perspective, undesirable responses such as visible vibration were eliminated.

Experiments during the design and tuning of the controller suggested that flaws in the current designs of SPAMs reduce their robustness in high-speed applications. Also, their current production methods did not achieve consistent prototypes and were not easily customizable. This inspired the development of a novel SPAM design, WSPAMs, that

rectifies these issues. The production of WSPAMs uses laser-cut silk mesh wrapped around a hollow silicone core. The specific cut pattern on the silk mesh determines the motion trajectory of the actuator and its poses during the motion. The use of a laser cutter provides for highly repeatable and precise fabrication, with parameters that are easily modified. This results in a consistent, highly customizable actuator production method.

In addition to their production method, a model for the steady-state angular displacement of the WSPAMs was presented, which describes the relationship between the cut pattern and tip angular displacement, for a given finger geometry and working pressure. A procedure for estimating the parameters of the model was described. It was shown that the model, using the estimated parameters, is capable of predicting the steady-state tip angular displacements with good accuracy. The model, together with physical design constraints, can be used to design robust WSPAMs capable of achieving a desired angular displacement.

In future work, the dynamic model of WSPAM actuators will be investigated. This will allow for a better understanding of the velocity profile of these actuators and the amount of force and torque they can provide. The dynamic model of the WSPAMs can be used for more complex and nonlinear controller designs that can improve the trajectory-following capabilities of WSPAMs. In addition, the production method of the WSPAMs can be reevaluated with more industrial and volume production requirements in mind. Lastly, the WSPAM production method can be used for motion trajectories other than the finger-like curved motion investigated in this work. In future work, the existing model can be generalized for the inclusion of alternative trajectory designs, and the closed-loop control design can be advanced to track general WSPAM designs.

Future work will also focus on the evaluation of the affective capabilities of the developed actuators. Using the WSPAM actuator, IFLS mechanisms will be implemented that perform the affective movements discussed in the thesis. The capability of the IFLS mechanism to convey the target emotions using movement will be investigated using user studies. The user studies can also be used to attain a better understanding of the factors that influence affective perception. The IFLS mechanism and controller can be used to vary the intensity and variability of motion performance to investigate the sensitivity of motion and appearance factors on affective motion perception.

Lastly, the IFLS mechanism will be integrated into an interactive architecture installation such as Hylozoic Soil [10]. The IFLS mechanism will be used as part of the interactive mechanism to generate affective movements as part of the interaction strategy. The ability of the IFLS to convey affect when embedded in an interactive architecture environment will be analyzed.

# Bibliography

- [1] M. Karg, A.-A. Samadani, R. Gorbet, K. Kuhlentz, J. Hoey, and D. Kulic, “Body movements for affective expression: a survey of automatic recognition and generation,” *Affective Computing, IEEE Transactions on*, vol. 4, no. 4, pp. 341–359, 2013.
- [2] A. Kleinsmith and N. Bianchi-Berthouze, “Affective body expression perception and recognition: A survey,” *Affective Computing, IEEE Transactions on*, vol. 4, no. 1, pp. 15–33, 2013.
- [3] B. Allison, G. Nejat, and E. Kao, “The design of an expressive humanlike socially assistive robot,” *Journal of Mechanisms and Robotics*, vol. 1, no. 1, p. 011001, 2009.
- [4] Y. Bar-Cohen and C. Breazeal, “Biologically inspired intelligent robots,” in *Smart Structures and Materials*, pp. 14–20, International Society for Optics and Photonics, 2003.
- [5] C. L. Breazeal, *Designing sociable robots*. MIT press, 2004.
- [6] C. Breazeal, “Toward sociable robots,” *Robotics and autonomous systems*, vol. 42, no. 3, pp. 167–175, 2003.
- [7] F. E. Pollick, H. M. Paterson, A. Bruderlin, and A. J. Sanford, “Perceiving affect from arm movement,” *Cognition*, vol. 82, no. 2, pp. B51–B61, 2001.
- [8] M. S. ADA, K. Suda, and M. Ishii, “Expression of emotions in dance: Relation between arm movement characteristics and emotion,” *Perceptual and motor skills*, vol. 97, no. 3, pp. 697–708, 2003.
- [9] A.-A. Samadani, E. Kubica, R. Gorbet, and D. Kulić, “Perception and generation of affective hand movements,” *International Journal of Social Robotics*, vol. 5, no. 1, pp. 35–51, 2013.

- [10] P. Beesley, “Hylozoic soil,” *Leonardo*, vol. 42, no. 4, pp. 360–361, 2009.
- [11] J.-H. Lee, J.-Y. Park, and T.-J. Nam, “Emotional interaction through physical movement,” in *Human-Computer Interaction. HCI Intelligent Multimodal Interaction Environments*, pp. 401–410, Springer, 2007.
- [12] M. Saerbeck and C. Bartneck, “Perception of affect elicited by robot motion,” in *Proceedings of the 5th ACM/IEEE international conference on Human-robot interaction*, pp. 53–60, IEEE Press, 2010.
- [13] *HYLOZOIC SOIL*, 2009.
- [14] M. Controzzi, C. Cipriani, and M. C. Carrozza, “Design of artificial hands: A review,” in *The Human Hand as an Inspiration for Robot Hand Development*, pp. 219–246, Springer, 2014.
- [15] J. Pons, E. Rocon, R. Ceres, D. Reynaerts, B. Saro, S. Levin, and W. Van Moorghem, “The manus-hand dextrous robotics upper limb prosthesis: mechanical and manipulation aspects,” *Autonomous Robots*, vol. 16, no. 2, pp. 143–163, 2004.
- [16] J. T. Belter, J. L. Segil, A. M. Dollar, and R. F. Weir, “Mechanical design and performance specifications of anthropomorphic prosthetic hands: A review,” *J Rehabil Res Dev*, vol. 50, no. 5, pp. 599–618, 2013.
- [17] T. Takaki and T. Omata, “High-performance anthropomorphic robot hand with grasping-force-magnification mechanism,” *Mechatronics, IEEE/ASME Transactions on*, vol. 16, no. 3, pp. 583–591, 2011.
- [18] A.-A. Samadani, B. DeHart, K. Robinson, D. Kulic, E. Kubica, and R. Gorbet, “A study of human performance in recognizing expressive hand movements,” in *RO-MAN, 2011 IEEE*, pp. 93–100, 31 2011-aug. 3 2011.
- [19] G. Stillfried, U. Hillenbrand, M. Settles, and P. van der Smagt, “Mri-based skeletal hand movement model,” in *The Human Hand as an Inspiration for Robot Hand Development*, pp. 49–75, Springer, 2014.
- [20] S. Montambault and C. M. Gosselin, “Analysis of underactuated mechanical grippers,” *Journal of Mechanical Design*, vol. 123, no. 3, pp. 367–374, 2001.
- [21] V. Scheinman and J. McCarthy, “Mechanisms and actuation,” in *Springer Handbook of Robotics* (B. Siciliano and O. Khatib, eds.), pp. 67–86, Springer Berlin Heidelberg, 2008.

- [22] A. Namiki, Y. Imai, M. Ishikawa, and M. Kaneko, “Development of a high-speed multifingered hand system and its application to catching,” in *Intelligent Robots and Systems, 2003.(IROS 2003). Proceedings. 2003 IEEE/RSJ International Conference on*, vol. 3, pp. 2666–2671, IEEE, 2003.
- [23] RobotShop, *Brushless DC Motors*, April 2015. <http://www.robotshop.com/ca/en/blcdc-motors.html>.
- [24] RobotShop, *24V, 58RPM, 138.87oz-in Brushless DC Gearmotor*, April 2015. <http://www.robotshop.com/ca/en/24v-58rpm-13887-oz-in-brushless-dc-gearmotor.html>.
- [25] Pololu, *30:1 Metal Gearmotor 37Dx52L mm*, Nov 2014. <http://www.pololu.com/product/1103>.
- [26] J. Jalani, G. Herrmann, and C. Melhuish, “Robust active compliance control for practical grasping of a cylindrical object via a multifingered robot hand,” in *Robotics, Automation and Mechatronics (RAM), 2011 IEEE Conference on*, pp. 316–321, IEEE, 2011.
- [27] A. Parmiggiani, G. Metta, and N. Tsagarakis, “The mechatronic design of the new legs of the icub robot,” in *Humanoid Robots (Humanoids), 2012 12th IEEE-RAS International Conference on*, pp. 481–486, IEEE, 2012.
- [28] I. W. Hunter, J. M. Hollerbach, and J. Ballantyne, “A comparative analysis of actuator technologies for robotics,” *Robotics Review*, vol. 2, 1991.
- [29] S. Jacobsen, E. Iversen, D. Knutti, R. Johnson, and K. Biggers, “Design of the utah/mit dextrous hand,” in *Robotics and Automation. Proceedings. 1986 IEEE International Conference on*, vol. 3, pp. 1520–1532, IEEE, 1986.
- [30] K. B. Fite, T. J. Withrow, K. W. Wait, and M. Goldfarb, “A gas-actuated anthropomorphic transhumeral prosthesis,” in *Robotics and Automation, 2007 IEEE International Conference on*, pp. 3748–3754, IEEE, 2007.
- [31] B. Peerdeman, G. Smit, S. Stramigioli, D. Plettenburg, and S. Misra, “Evaluation of pneumatic cylinder actuators for hand prostheses,” in *Biomedical Robotics and Biomechatronics (BioRob), 2012 4th IEEE RAS & EMBS International Conference on*, pp. 1104–1109, IEEE, 2012.
- [32] Festo, *Airic’s Arm*, 2007. [http://www.festo.com/cms/en\\_corp/9785\\_10400.htm](http://www.festo.com/cms/en_corp/9785_10400.htm).

- [33] R. Walkler, “Developments in dextrous hands for advanced robotic applications,” in *Proc. the Sixth Biannual World Automation Congress, Seville, Spain*, pp. 123–128, 2004.
- [34] Y. Honda, F. Miyazaki, and A. Nishikawa, “Angle control of pneumatically-driven musculoskeletal model using antagonistic muscle ratio and antagonistic muscle activity,” in *Robotics and Biomimetics (ROBIO), 2010 IEEE International Conference on*, pp. 1722–1727, dec. 2010.
- [35] S. Nishino, N. Tsujiuchi, T. Koizumi, H. Komatsubara, T. Kudawara, and M. Shimizu, “Development of robot hand with pneumatic actuator and construct of master-slave system,” in *Engineering in Medicine and Biology Society, 2007. EMBS 2007. 29th Annual International Conference of the IEEE*, pp. 3027–3030, IEEE, 2007.
- [36] D. Plettenburg, “Electric versus pneumatic power in hand prostheses for children,” *Journal of medical engineering & technology*, vol. 13, no. 1-2, pp. 124–128, 1989.
- [37] D. Stoianovici, A. Patriciu, D. Petrisor, D. Mazilu, and L. Kavoussi, “A new type of motor: pneumatic step motor,” *Mechatronics, IEEE/ASME Transactions on*, vol. 12, no. 1, pp. 98–106, 2007.
- [38] J. Huber, N. Fleck, and M. Ashby, “The selection of mechanical actuators based on performance indices,” *Proceedings of the Royal Society of London. Series A: Mathematical, Physical and Engineering Sciences*, vol. 453, no. 1965, pp. 2185–2205, 1997.
- [39] pro-dex, *Air Motors*. <http://www.pro-dex.com/air-motors.aspx>.
- [40] G. Andrikopoulos, G. Nikolakopoulos, and S. Manesis, “A survey on applications of pneumatic artificial muscles,” in *Control & Automation (MED), 2011 19th Mediterranean Conference on*, pp. 1439–1446, IEEE, 2011.
- [41] H. Schulte, “The characteristics of the mckibben artificial muscle,” *The application of external power in prosthetics and orthotics*, vol. 874, pp. 94–115, 1961.
- [42] K. Suzumori, S. Wakimoto, K. Miyoshi, and K. Iwata, “Long bending rubber mechanism combined contracting and extending fluidic actuators,” in *Intelligent Robots and Systems, 2013. IROS 2013. IEEE/RSJ International Conference on*, IEEE, 2013.
- [43] R. B. Van Varseveld and G. M. Bone, “Accurate position control of a pneumatic actuator using on/off solenoid valves,” *Mechatronics, IEEE/ASME Transactions on*, vol. 2, no. 3, pp. 195–204, 1997.

- [44] M. Taghizadeh, A. Ghaffari, and F. Najafi, “Modeling and identification of a solenoid valve for pwm control applications,” *Comptes Rendus Mecanique*, vol. 337, no. 3, pp. 131–140, 2009.
- [45] V. Jouppila and A. Ellman, “Position control of pwm-actuated pneumatic muscle actuator system,” *ASME Conference Proceedings*, vol. 2011, no. 54938, pp. 393–404, 2011.
- [46] S. Schulz, C. Pylatiuk, M. Reischl, J. Martin, R. Mikut, and G. Bretthauer, “A hydraulically driven multifunctional prosthetic hand,” *Robotica*, vol. 23, no. 03, pp. 293–299, 2005.
- [47] K. Hoshino and W. Krishantha, “Calligraphic motion by humanoid robot arm using air cylinder actuators as endoskeletons,” in *Mechatronics, ICM2007 4th IEEE International Conference on*, pp. 1–6, IEEE, 2007.
- [48] K. Yang and C. Gu, “A novel robot hand with embedded shape memory alloy actuators,” *Proceedings of the Institution of Mechanical Engineers, Part C: Journal of Mechanical Engineering Science*, vol. 216, no. 7, pp. 737–745, 2002.
- [49] C. Y. Low, M. A. A. Kasim, T. Koch, R. Dumitrescu, H. Yussof, R. Jaafar, A. A. Ahmed Jaffar, and K. M. Ng, “Hybrid-actuated finger prosthesis with tactile sensing,” *INTERNATIONAL JOURNAL OF ADVANCED ROBOTIC SYSTEMS*, vol. 10, 2013.
- [50] R. B. Gorbet and R. A. Russell, “A novel differential shape memory alloy actuator for position control,” *Robotica*, vol. 13, no. 04, pp. 423–430, 1995.
- [51] M. Liang and W. Zhang, “Analysis of coupled-active fingers with gear mechanism,” in *Informatcs in Control, Automation and Robotics*, pp. 439–446, Springer, 2012.
- [52] G. Li, H. Liu, and W. Zhang, “Development of multi-fingered robotic hand with coupled and directly self-adaptive grasp,” *International Journal of Humanoid Robotics*, vol. 9, no. 04, 2012.
- [53] G. Li and W. Zhang, “Study on coupled and self-adaptive finger for robot hand with parallel rack and belt mechanisms,” in *Robotics and Biomimetics (ROBIO), 2010 IEEE International Conference on*, pp. 1110–1115, IEEE, 2010.
- [54] L.-R. Lin and H.-P. Huang, “Ntu hand: A new design of dexterous hands,” *Journal of Mechanical Design*, vol. 120, no. 2, pp. 282–292, 1998.

- [55] H. Kawasaki, T. Komatsu, and K. Uchiyama, “Dexterous anthropomorphic robot hand with distributed tactile sensor: Gifu hand ii,” *Mechatronics, IEEE/ASME Transactions on*, vol. 7, no. 3, pp. 296–303, 2002.
- [56] T. Zhang, S. Fan, L. Jiang, and H. Liu, “Development and experiment analysis of anthropomorphic prosthetic hand with flexible three-axis tactile sensor,” *International Journal of Humanoid Robotics*, vol. 10, no. 03, 2013.
- [57] M. Rakić, “An automatic hand prosthesis,” *Medical electronics and biological engineering*, vol. 2, no. 1, pp. 47–55, 1964.
- [58] F. Lotti, P. Tiezzi, G. Vassura, L. Biagiotti, and C. Melchiorri, “Ubh 3: an anthropomorphic hand with simplified endo-skeletal structure and soft continuous fingerpads,” in *Robotics and Automation, 2004. Proceedings. ICRA '04. 2004 IEEE International Conference on*, vol. 5, pp. 4736–4741, IEEE, 2004.
- [59] A. M. Dollar and R. D. Howe, “The highly adaptive sdm hand: Design and performance evaluation,” *The international journal of robotics research*, vol. 29, no. 5, pp. 585–597, 2010.
- [60] J. K. Salisbury and J. J. Craig, “Articulated hands force control and kinematic issues,” *The International Journal of Robotics Research*, vol. 1, no. 1, pp. 4–17, 1982.
- [61] H. A. Baldwin, “Realizable models of muscle function,” in *Biomechanics*, pp. 139–147, Springer, 1995.
- [62] F. Daerden and D. Lefeber, “Pneumatic artificial muscles: actuators for robotics and automation,” *European journal of mechanical and environmental engineering*, vol. 47, no. 1, pp. 11–21, 2002.
- [63] Y. S. Song, Y. Sun, R. Van Den Brand, J. Von Zitzewitz, S. Micera, G. Courtine, and J. Paik, “Soft robot for gait rehabilitation of spinalized rodents,” in *Intelligent Robots and Systems (IROS), 2013 IEEE/RSJ International Conference on*, pp. 971–976, Ieee, 2013.
- [64] P. Polygerinos, Z. Wang, K. C. Galloway, R. J. Wood, and C. J. Walsh, “Soft robotic glove for combined assistance and at-home rehabilitation,” *Robotics and Autonomous Systems*, 2014.
- [65] G. Fantoni, M. Santochi, G. Dini, K. Tracht, B. Scholz-Reiter, J. Fleischer, T. K. Lien, G. Seliger, G. Reinhart, J. Franke, *et al.*, “Grasping devices and methods in

- automated production processes,” *CIRP Annals-Manufacturing Technology*, vol. 63, no. 2, pp. 679–701, 2014.
- [66] C. Blanes, M. Mellado, and P. Beltran, “Novel additive manufacturing pneumatic actuators and mechanisms for food handling grippers,” in *Actuators*, vol. 3, pp. 205–225, Multidisciplinary Digital Publishing Institute, 2014.
- [67] F. Ilievski, A. D. Mazzeo, R. F. Shepherd, X. Chen, and G. M. Whitesides, “Soft robotics for chemists,” *Angewandte Chemie*, vol. 123, no. 8, pp. 1930–1935, 2011.
- [68] K. Suzumori, S. Iikura, and H. Tanaka, “Applying a flexible microactuator to robotic mechanisms,” *Control Systems, IEEE*, vol. 12, no. 1, pp. 21–27, 1992.
- [69] R. Deimel and O. Brock, “A compliant hand based on a novel pneumatic actuator,” in *Robotics and Automation (ICRA), 2013 IEEE International Conference on*, pp. 2047–2053, IEEE, 2013.
- [70] R. F. Shepherd, F. Ilievski, W. Choi, S. A. Morin, A. A. Stokes, A. D. Mazzeo, X. Chen, M. Wang, and G. M. Whitesides, “Multigait soft robot,” *Proceedings of the National Academy of Sciences*, vol. 108, no. 51, pp. 20400–20403, 2011.
- [71] K. Suzumori, S. Endo, T. Kanda, N. Kato, and H. Suzuki, “A bending pneumatic rubber actuator realizing soft-bodied manta swimming robot,” in *Robotics and Automation, 2007 IEEE International Conference on*, pp. 4975–4980, IEEE, 2007.
- [72] K. Suzumori, S. Iikura, and H. Tanaka, “Development of flexible microactuator and its applications to robotic mechanisms,” in *Robotics and Automation, 1991. Proceedings., 1991 IEEE International Conference on*, pp. 1622–1627, IEEE, 1991.
- [73] J. P. Yi Sun, Yun Seong Song, “Characterization of silicone rubber based soft pneumatic actuators,” in *Intelligent Robots and Systems, 2013. IROS 2013. IEEE/RSJ International Conference on*, IEEE, 2013.
- [74] SmoothOn, *Ecoflex Supersoft Silicone*, 2015. [http://www.smooth-on.com/Silicone-Rubber-an/c2\\_1115\\_1130/index.html?catdepth=1](http://www.smooth-on.com/Silicone-Rubber-an/c2_1115_1130/index.html?catdepth=1).
- [75] X. Shen, “Nonlinear model-based control of pneumatic artificial muscle servo systems,” *Control Engineering Practice*, vol. 18, no. 3, pp. 311 – 317, 2010.
- [76] T. V. Minh, T. Tjahjowidodo, H. Ramon, and H. Van Brussel, “Cascade position control of a single pneumatic artificial muscle–mass system with hysteresis compensation,” *Mechatronics*, vol. 20, no. 3, pp. 402–414, 2010.

- [77] D. C. Karnopp, D. L. Margolis, and R. C. Rosenberg, *System Dynamics: Modeling, Simulation, and Control of Mechatronic Systems*. Wiley, 2012.